

R-1110
CU-328
NEVIS-222

Nevis Laboratories
Columbia University
Physics Department
Irvington-on-Hudson
New York

ψ and ψ' Production in Hadron Collisions

DAVID CHU HOM

Reproduction in whole or in part
is permitted for any purpose of the
United States Government

Submitted in partial fulfillment of
the requirements for the degree
of Doctor of Philosophy in the Faculty
of Pure Science, Columbia University

1977

National Science Foundation
NSF PHY 76-84396

ψ and ψ' Production in Hadron Collisions *

DAVID CHU HOM †

Columbia University, New York, N.Y. 10027

* Research supported by the National Science Foundation.

† Submitted in partial fulfillment of the requirements for the degree of Doctor of Philosophy in the Faculty of Pure Science, Columbia University.

ABSTRACT

This thesis describes the design and operation of a double arm spectrometer for observing and measuring electron-positron pairs created in the collision of high energy protons with nuclei at the Fermi National Accelerator Laboratory. The data analysis and the results of the analysis are discussed. We have observed the production and decay of narrow resonances $\psi(3100)$ and $\psi'(3700)$. The production dynamics of $\psi(3100)$, in particular the distribution in transverse momenta, have been measured. The average $\langle p_t \rangle$ is observed to be higher than that of any previously measured particle. The total cross section at 90° in the center of mass has been determined for 300 and 400 GeV incident protons. Comparison with data of other experiments yields an excitation curve for ψ production versus proton energy. The $\psi'(3700)$ is observed here for the first time in hadronic production. The ratio of ψ' to ψ production

is found to be 0.018 ± 0.006 at 400 GeV and 0.014 ± 0.005 at 300 GeV. This result was not expected in current theories which try to understand ψ production as a direct result of quark collisions.

TABLE OF CONTENTS

	<u>Page</u>
I. Introduction	1
II. Experimental Apparatus	
A. Design Requirements	7
B. Overview	8
C. Apparatus Description	8
III. Data Acquisition	
A. Fast Logic	14
B. DC Logic	15
C. Readout System	17
D. On-Line Computer System	18
E. Data Taking	19
IV. Data Analysis and Results	
A. Description of Analysis	21
B. Results	25
C. Studies	30
V. Summary and Conclusions	
A. Summary of Results	35
B. Theoretical Significance	35
VI. Acknowledgments	39
Appendix I: Lead Glass Calorimeter	41
Appendix II: Digitizers and Digitizer Readout System	46
Appendix III: Lead Glass Calibration	49
Appendix IV: Proportional Wire Chamber Reconstruction	52

Appendix V: Magnetic Reconstruction	56
Appendix VI: Lead Glass Energy Determination	59
Appendix VII: Lead Glass Resolution	62
Appendix VIII: Longitudinal Shower Development	63
Appendix IX: Monte Carlo Calculation of Acceptances	66
Appendix X: Accidental Background Determination	69
References	72
Tables	77
Figures	95

I. INTRODUCTION

This thesis is on an experiment proposed to search for high mass dilepton pairs in proton nucleus collisions.

$$p + Be \rightarrow \gamma + \text{anything}$$
$$\quad \quad \quad \searrow \quad \quad \quad \swarrow$$
$$\quad \quad \quad \ell^+ \ell^- \quad \quad \quad .$$

Lepton pair production is a second generation experiment of a series of lepton experiments by the Columbia-Fermilab Collaboration. The first generation lepton experiment was single lepton production.¹

The motivations for this experiment are at least twofold: probe the nucleon structure and search for possible resonances.

In this experiment we probe the electromagnetic structure of the nucleon by studying the continuum dilepton spectrum in an unexplored mass range. We are looking at the process shown in Fig. 1. This is analogous to deep inelastic lepton-nucleon scattering (Fig. 2), where the virtual photon is spacelike.² We are looking at a timelike virtual photon. In both cases a known probe, the photon, is used to study the nucleon electromagnetic structure. The lepton-photon vertex is totally understood by QED. It is then the photon-hadron vertex we are studying. Measurements of the hadronic vertex function give us information about the nucleon structure. Another related process is hadron production in colliding e^+e^- beam experiments³ (see Fig. 3). Again the photon is timelike.

There are of course theoretical models of how a photon interacts with hadrons. One of the most studied of these

models is the parton model as deployed by Bjorken.⁴ In this model the hadron is composed of pointlike constituents. This decomposition allows calculations to be done exactly (except for sums over parton distributions) as the hadronic vertex is reduced to QED. This picture of the hadron can easily be shown to predict Bjorken scaling in deep inelastic lepton nucleon scattering. That is the cross section is a function of $x = q^2 / 2M\nu$ (see Fig. 2), instead of both q^2 and ν . Drell and Yan⁵ showed how massive lepton pairs could be produced in hadron-hadron collisions using the parton model. Their model is shown in Fig. 4. Their differential cross section also exhibits scaling:

$$\frac{d\sigma}{dQ^2} = \frac{4\pi\alpha^2}{3Q^2} \frac{1}{Q^2} f(\tau) ,$$

$$\text{where } f(\tau) = \int_0^1 dx_1 \int_0^1 dx_2 \delta(\tau - x_1 x_2) \sum_i \lambda_i^{-2} F_{2i}(x_1) \bar{F}_{2i}(x_2) .$$

$4\pi\alpha^2/3Q^2$ is the total cross section for $e^+e^- \rightarrow \mu^+\mu^-$. $f(\tau)$ is essentially a sum over parton distributions. λ_i is the charge of the i^{th} parton type. τ is the scaling variable:

$$\tau = Q^2/s ,$$

where Q^2 is the lepton pair mass squared and s is the pp c.m. energy squared. x_i is the parton fractional momentum. The F_{2i} and \bar{F}_{2i} are νW_2 as measured in deep inelastic scattering.² The $\nu, \bar{\nu}$ measurements for the antiparton distributions are at the moment very uncertain.⁶ This makes comparison of the parton model with lepton pair production very difficult.⁷ We can turn

the problem around and determine the antiparton distribution from the dilepton spectrum, as the parton distribution is known from deep inelastic experiments.

There are many theoretical models. Among the first are those of Berman-Bjorken-Kogut and Bjorken-Paschos and Kuti-Weisskopf.⁸ In the Kuti-Weisskopf model partons are identified with quarks of Gell-Mann and Zweig.⁹ Theoretical prejudices and/or simplifications are used to predict various parton distribution functions. With improved deep inelastic ep, μp and νp measurements¹⁰, phenomenological fits have been made for parton distributions. This permitted better calculations of the Drell-Yan process.¹¹

The other motivation of this experiment is to look for new structure in the mass spectrum. The literature abounds with speculations of new particles, especially for weak and electromagnetic interactions. As is well known the status of weak interaction theory is not completely satisfactory. The modern form of Fermi's theory of weak interactions¹² is due to Feynman and Gell-Mann¹³: the leptonic current is of the V-A form, the CVC hypothesis is assumed. The theory has been highly successful for first order weak processes. It is only when attempts to calculate higher order processes are made that difficulties are encountered. Yukawa's¹⁴ introduction of the intermediate vector boson (W^\pm) only postponed the unitarity violation of the theory at high energy. Worse still

the theory was not renormalizable. It is hoped, that at high energies and high transverse momentum ($p_t > 1 \text{ GeV}/c$), the electromagnetic and weak interactions would be competitive with the strong interactions. If that is the case there is the possibility of studying and improving our knowledge of weak and electromagnetic interactions at high energy. Using the full energy of the primary beam at Fermilab, we explore the highest accessible masses.

Predictions of intermediate bosons have been made for a long time. So far they have not been found. Yamaguchi¹⁵, using CVC, has been able to relate the electromagnetic process of $l^+ l^-$ production to the production of W^\pm . A measurement of lepton pair production can be used to set limits on the W mass if it is not found.¹⁶ A practical use of dilepton measurements with the use of scaling is to determine the parameters of a W^\pm search experiment or of an accelerator designed to produce W^\pm .

Lee and Wick¹⁷ have introduced a theory of QED with finite renormalization. The photon propagator is modified by the introduction of a new particle, the B^0 . B^0 , being massive, can decay into lepton pairs directly.

Recently there has been a great deal of interest in gauge theories. It started when Weinberg and Salam¹⁸ independently succeeded in unifying weak and electromagnetic interactions into one theory. The W^\pm and the photon became gauge bosons in their model. The disparity between the weak

and electromagnetic interactions was attributed to a spontaneous breaking of the gauge symmetry. The symmetry breaking gave the W^\pm its mass. It was suggested that the theory might be renormalizable as the gauge bosons are massless at the start. In addition to the charged vector bosons W^\pm , a neutral boson, was predicted: Z^0 . The Z^0 could be detected by its $l^+ l^-$ decay mode.

Georgi and Glashow¹⁹ proposed an alternative model without neutral currents (Z^0). Instead they predicted heavy lepton counterparts of the electron and muon (E^0, E^+, M^0, M^+). As of this writing neutral currents have been observed²⁰, but the existence of heavy leptons is an open question.²¹ There are models which have both neutral bosons as well as heavy leptons.²²

Before the advent of renormalizable gauge theories, Bjorken and Glashow²³ motivated the introduction of a fourth "charmed" quark. Their argument was based upon the leptons being a pair of doublets and arguing for a similar symmetry for hadrons.

$$\begin{pmatrix} \nu_e \\ \nu_\mu \\ e^- \\ \mu^- \end{pmatrix} \longleftrightarrow \begin{pmatrix} c \\ u \\ d \\ s \end{pmatrix}$$

Glashow, Iliopoulos and Maiani²⁴ provided a better basis for such a conjecture when they found that strangeness changing weak currents were suppressed to first order in G (Fermi coupling constant) in accord with experiments.

In the last few years there has been growing evidence for the validity of the SU(4) quark model. The discovery of the J/ψ meson²⁵, now believed to be the lowest state of $c\bar{c}$, provided the initial direct evidence. In addition, many excited and related states ($\psi', \psi'', \chi \dots$) have been observed at SPEAR.²⁶ Recent experiments may have also observed charmed baryons.²⁷

There has been a recent surge of interest in dilepton production since the measurements of single lepton production.²⁸ Single leptons were found to have an invariant cross section as a function of p_t very similar to pions scaled by 10^{-4} . This suggested the possibility that leptons were due to the production of objects with hadronic cross sections which decayed leptonically: $\phi, J/\psi, \psi'$.

This thesis will be on the production dynamics of the ψ/ψ' mesons in $p + Be$ collisions.²⁹ The J/ψ has previously been observed in hadron-hadron collisions. This is the first observation of the ψ' in such collisions. The higher mass spectrum is described elsewhere.³⁰

II. EXPERIMENTAL APPARATUS

A. Design Requirements

Since we are looking at a process of the Drell-Yan gender, we expect a very small cross section. To be able to pick up any unusual pearls in this debris of hadronic sand, we would require a hadron pair rejection of order 10^7 . There are two approaches to this problem. The first approach is to observe electron-positron pairs. Here we must be able to distinguish between hadrons and electrons. The problem with this approach is that we would be limited in incident beam intensity by the large hadronic flux. The second approach is to absorb the hadrons before they can reach the apparatus. Here we must observe muon pairs. This approach suffers from loss of resolution due to energy loss and multiple scattering in a hadron absorber. Our decision was to perform the experiment with the first method. A followup experiment will try to increase the sensitivity in the high mass region using muon pairs.³¹

To observe electron-positron pairs we require a hadron rejection of 10^3 to 10^4 per arm of the spectrometer. Since there is a large flux of hadrons we must be able to take high counting rates to explore small cross sections. A problem created by high rates is accidentals. To alleviate part of this problem we must have good time resolution. Due to the beam structure (18.9 ns), a resolution of 15 ns was sufficient.

As we are one of the first experiments to look at such a high mass region, we also want to be sensitive to resonances. Resonances would appear as peaks sitting on a continuum. Very good mass resolution is required so that any peaks would not be smeared out ($\sigma = 1\%$).

Since there is a large π^0 and η flux, care must be taken to avoid conversion of γ rays from their decay.

B. Overview

The apparatus is a double arm spectrometer with each arm on the opposite side of 90° in the pp c.m. for 300 and 400 GeV proton beams. Each arm covered a solid angle of 0.06 sr in the pp c.m. system. Each arm consisted of a 9-plane wire chamber-hodoscope magnetic spectrometer. No detectors were placed before the magnet so that we could take high beam flux. Charged particles were deflected in the vertical plane and the target is viewed in the horizontal nonbending plane. Electron identification was provided by a lead glass spectrometer sitting behind the magnetic spectrometer. A detailed description of the apparatus follows.

C. Apparatus Description

Our description of the apparatus will proceed in the same order as the beam would see it. The experiment was performed in the Proton Center Laboratory of the Fermi National Accelerator Laboratory. We will describe only one arm of the spectrometer since the arms were symmetric. The two arms were identical

except for a 180° rotation about the incident beam direction. Each arm of the spectrometer detected particles of one sign only. The apparatus is shown in Figs. 5 and 6.

A very thin target with low Z was required to avoid γ conversions. A beryllium target (4 in. long by 0.0088 in. wide by 4 in. high), known as Be VII, was used for normal data taking. In order to maintain a high ratio of interaction rate to incident beam flux, we required an extremely small beam spot size. It was on this criterion that the beam line in Proton Center was designed. We had control over the last section of the beam line. With the use of bending and quadrupole magnets, we were able to obtain a beam spot size of 0.4×2 mm. Our average targeting efficiency was 60%. The incident beam intensity was monitored by an SEM (secondary emission monitor, known as PCSEM) and an ion chamber. The beam position was tracked by SWICs (split wire ionization chamber). A beam dump was located 7 ft downstream of the target to absorb forward going particles. A large box containing the target, beam dump and the first part of the shielding for the spectrometer was filled with helium to minimize conversion material in the aperture through which the apparatus viewed the target. Collimators viewed the target symmetrically on both sides of the horizontal plane. Each collimator spanned from 50 to 95 mrad horizontally and ± 3.5 mrad vertically.

An automatic filter cycling system was placed after the target box. This allowed the insertion of conversion material

into the secondary beam. About 1 ft after the filters, a 2 in. tungsten collimator defined the actual vertical apertures of ± 3.5 mrad. Next came the shielding and 7-ft collimator. The collimated beam saw only vacuum from the upstream end of the collimator until the exit of the analyzing magnet.

The 10-ft long analyzing magnet was a dipole magnet with the fields in the horizontal plane perpendicular to the spectrometer axis. It sat 35 ft from the target. At a setting of 1300 A the integral field was 35 kG-meters or equivalently a p_t kick of 1.05 GeV/c. The major part of the data taking was at four settings of the spectrometer: 600, 800, 1100, 1300 A. In the left arm of the spectrometer, charged particles were bent upward. This arm was referred to as the up arm (up). The right arm had charged particles bent down into it. This arm was referred to as the down arm (dn). The reason for this bending up and down was that we gained 30% in acceptance. The two magnets were always set to symmetric fields strengths although the polarities were varied.

Helium bags were placed between the magnets and the first detectors to minimize conversions. The first detector station occurred after the magnet 80 ft from the target. This allowed the low momentum charged particles to be swept out. A separation between charged and neutral particles allowed us to place the detectors in the charged beam only.

The neutral beam which views the target directly consisted of a tremendous flux of γ 's and neutrons. The first counters were a set of three planes of multiwire proportional chambers (MWPC) with 2 mm wire spacing (Y_1, P_1, Q_1). One chamber had horizontal wires. The other two were small angle stereo chamber ($\pm \arctan(1/8)$ with respect to horizontal). Right behind the wire chambers was a plane of 38 strips of vertical scintillation counters (denoted by V_1). V_1 was then followed by a plane of trigger counters called T_0 .

Two meters behind the 80 ft station was a set of counters used to monitor our targeting efficiency. These counters sat in the neutral beam. They should not have seen any charged particles therefore they should have had no magnet setting dependence. They did in fact have a magnet dependence of $< 10\%$. This dependence was attributed to scattering of soft charged particles off the magnet polefaces. These counters will be denoted by NDN (or NDNBY). The so-called neutral beam blockers were between the 80 ft and 100 ft stations. Their purpose was to stop the neutral beam before it reached that part of a lead glass spectrometer which would have intercepted the neutral beam envelope. They consisted of slabs of steel backed by concrete blocks stacked outside of the aperture.

A one-plane wire chamber (Y_2) was placed at the 100 ft station. The chamber had horizontal wires of 3 mm spacing. A plane of trigger counters called T_1 was placed immediately behind the chamber.

The third detector station is at 120 ft. It begins with a set of 3 mm wire chambers: 1 horizontal and 2 small angle stereo (Y_3, P_3, Q_3). Following this was a hodoscope plane of 55 vertical scintillation strips (V_2). The next pieces of apparatus were contained in the superstructure for the lead glass array. The superstructure was housed in a temperature and humidity controlled fiber glass hut. The first object encountered by a particle was 2 radiation lengths of lead (0.5 in.). The lead started the electromagnetic shower earlier thereby improving the hadron rejection. This was followed by another plane of trigger counters S_2 . Finally, in between the first and second layer of lead glass (to be described) was another plane of trigger counters T_2 . The T_2 's were used in the fast logic to signal a shower in the lead glass.

The most important part of the apparatus in electron identification (and hadron rejection) was the lead glass spectrometer (Appendix I). From previous experiences a lead glass spectrometer can give hadron rejection of 10^4 event by event.^{1,32} Each arm of the spectrometer had an array of 96 blocks arranged as shown in Fig. 7. Each block was optically isolated from the others. Each had an RCA 8055 photomultiplier glued on. The photomultiplier bases were designed to have a linear response over a large dynamic range.³² The arrangement of blocks gave sampling of the shower development which is used in electron identification.

The other function of the lead glass spectrometer was to measure the energy of the electron. Its resolution increased with energy whereas the magnetic spectrometer resolution decreased. Thus they complemented each other very well³² (see Fig. 8).

The lead glass was 25.8 radiation lengths and 1.5 absorption lengths deep. Table I gives the various properties of the lead glass.

III. DATA ACQUISITION

A. Fast Logic

We will follow the data acquisition process in a natural order: from triggering until it is recorded onto magnetic tape.

The basic fast trigger required a track through the apparatus and an associated electromagnetic shower in the lead glass. A track was defined by a coincidence of three trigger counters:

$$T = T_0 \cdot T_1 \cdot S_2 \quad .$$

A typical T rate was about 1 MHz. The uncorrelated counting rates in the separate planes (singles rates) were typically four times higher. Note that S_2 counts single minimum ionizing particles here. A coincidence was then made with T_2 . We required that the pulse height in T_2 correspond to greater than 15 minimum ionizing particles. This signaled a shower of some sort after the first layer of lead glass.

$$E = T \cdot T_2 \quad .$$

A typical E rate was 100 kHz. E was defined as the fast trigger for a single electron. An electron-positron pair trigger was formed by the coincidence of an electron in one arm and a positron in the other:

$$E_{UD} = E_{UP} \cdot E_{DN} \quad ,$$

(where $E_{UP} = E$ for up arm, $E_{DN} = E$ for down arm). The E_{UD} rate was about 1 kHz. The fast logic is schematically

shown in Fig. 9. The fast logic trigger defined the so-called TFI (trigger fan-in).

B. DC Logic

By now the trigger rate has been reduced by a considerable amount. Further requirements were made on the DC logic level before an event qualified to be read into the computer. The DC logic (shown in Fig. 10 in a simplified block diagram form) allowed fairly sophisticated decision making. Its deadtime was set to 100 ns to allow time for the DC logic to make a decision. To keep its livetime as high as possible ($> 99\%$), it should not be triggered at greater than about 100 kc. The DC logic provided 32 bits (known as the logic bus) with which logical combinations were made. This was accomplished using the so-called pin logic modules. TFI fired TGI (trigger input generator) if the DC logic was live. A number of things happen: gates were sent to the MWPC coincidence registers (CR's) and hodoscope CR's, logic bus CR's and a delayed strobe to the logic bus. For the MWPC CR's, the gate width was 50 ns. The hodoscope signals were clipped to 2 ns by the CR input stage and then gated by an 18 ns gate. The logic bus CR gate was 9 ns.

An electron on the DC logic level required that the E bit and the ϵ bit be set. The E bit was the fast logic trigger given above. The ϵ bit was derived from summing the pulse height of the first two layers of lead glass. This

pulse then must pass a discriminator threshold to signify a shower in the lead glass. When this condition was satisfied in both arms, the pin logic modules would fire a TGO (output trigger generator). This signaled the acceptance of the trigger. Normal data rates ranged from 10-50 events per pulse. Table II gives a sample trigger rate.

The firing of TGO did a number of things. TGO deadtime was incurred for the readout duration. A strobe pulse was sent from the TGO module to the hodoscope data buffers. This caused the storage of the hodoscope CR information into the buffers. A read pulse was sent to the MWPC system to block the reset pulse, thus keeping the MWPC information stored in the CR's. Gates to various amplitude and time digitizers (ADC's and TDC's) were opened. After allowing for digitizing time (20 μ s), a trigger pulse was sent to the CAMAC branch driver interface (BD). This started the readout of the event.

When the DC logic became live again (100 ns after TGI), it continued to cycle with each TGI while the interface was reading in the accepted event. This allowed various rates satisfying the DC logic requirements to be scaled on blind scalars. Care was taken to have the DC logic deadtime overlap with the TGO deadtime.

Another important feature of the DC logic (from which it derives its name) is that after the CR's, no retiming was

required. Thus any late arriving signal could easily be accommodated. New triggers were very easy to implement (in fact too easy).

C. Readout System

The entire readout system and the DC logic, except for two standard CAMAC crates, were designed by H. Cunitz and W. Sippach of the Nevis Electronics Group. Our system was equivalent to a five CAMAC crate system. The six crate 4000 channel MWPC system was a second generation version of the Nygren-Carithers Brookhaven system.³³ It featured a fairly sophisticated fast nonserial readout scheme. Readout time is proportional to the number of nonadjacent wires firing. The hodoscope system was a smaller prototype employing double buffering. In addition to the MWPC and hodoscope system interface in crate 1, we had an assortment of data buffers (registers), a computer controlled pulser, LED (light emitting diode) display module, crate links to crates 3 and 4 (which contained the Nevis ADC scalers). Crate 2 contained blind scalers. Crate 5 contained LeCroy ADC's and TDC's and an NAL DVM (digital voltmeter) control module. In addition, a Jorway BD72A allowed us to see the contents of the blind scalers on a display terminal.

The Nevis ADC system consisted of 256 channels of 10-bit readout. Use was made of the branch driver and a packer module to pack the data in hardware. ADC's were selectively read out to reduce event size. See Appendix II for details.

The branch driver interface (BD) was the funnel of the data into the computer. It read out events as programmed in its RAM (random access memory). It performed all CAMAC and our on-line computer (PDP-15) protocols. Many improvements were made in the BD from the previous experiment¹: off-line cycling capabilities, priority system to allow the BD72A, various LED displays to increase our debugging capabilities.

D. On-Line Computer System

The experiment was on-line to a Digital Equipment Corporation (DEC) Unichannel-15 computer. The hardware consisted of a PDP-15 and PDP-11 linkup. On the PDP-15, we had 32 K core memory, floating point hardware, DEctape and magnetic tape drives, a line printer, storage scope, an RF15 256 K word fixed head disk and the branch driver interface. On the PDP-11 we had a 1.2 M word RK05 floating head disk, a line-printer, and a TU-10 magnetic tape drive.

The on-line program was written with data acquisition as its primary task. Maximum use was made of the powerful computing system for on-line purposes. The interrupt structure of the PDP-15 was used so that polling (interrogation by the CPU), requiring CPU time, was not required.

The on-line program set up the BD interface to prepare it for data taking. A minimum of bookkeeping was done after each event to keep computer deadtime low. When a buffer was filled, it was written out to the RF15 disk while the next

buffer was filling (use was made of DMA (direct memory access) and memory cycle stealing). This allowed very large fast buffering during the beam spill. At the end of the beam spill, blind scalers were read. Then full buffers were read from the RF15 and written to magnetic tape. To insure a minimum of downtime, the program was written to be able to use the peripherals on both PDP-15 and PDP-11.

The on-line program also provided: analysis capabilities, various monitoring, pedestal taking, calibration, timing and plateauing. The primary program monitored the MWPC, ADC, hodoscope, and blind scalers. The end of run summary produced was a record of this monitoring. Computerized high voltage scans of 400 channels were performed regularly. The user could also interact with the computer to have various services performed. He could have various histograms or distributions printed or displayed on a storage scope. In addition, he could define histograms of various quantities and have them output on request.

All analysis and servicing of requests were done during the time between beam spills.

E. Data Taking

Data runs in general were 1-2 hours long. Triggers during normal data taking were electron-positron pairs and single arm electrons. The end of run summaries were carefully checked to insure that all the apparatus was in working order on a run by run basis.

Twice a week, muon calibration runs were taken using the T triggers with the target out. The gains of four consecutive lead glass blocks are equalized with these runs. The muons were generated by the interaction of the beam with the beam dump. Due to the amount of material present, only muons escaped from the dump. Electron calibration runs were taken once a week. These runs (known as E/p runs) used the copper target to enhance the conversion electrons in the spectrometer arm of interest. Electron calibration runs determined the absolute energy scale of the lead glass pulse height. A more detailed description of the calibration procedure appears in Appendix III.

There were so-called Be III runs in which a Be target, identical to Be VII but 2.2 mm wide, was used. This insured that the entire beam was incident on target. This run was used to calibrate our targeting monitor NDN.

The study of the longitudinal electron shower development required a special run with enhanced electron sample. This run was similar to the E/p runs.

In addition, there was a host of special runs to study timing, plateau various counters, and to check various efficiencies.

IV. DATA ANALYSIS AND RESULTS

This section is divided into three parts:

- A. Description of Analysis; B. Results of Analysis;
- C. Study of Biases, Efficiencies and Backgrounds.

A. Description of Analysis

The first steps of the analysis begins with a first pass on the raw data tapes. The purpose of this first pass is to reduce the data by throwing out events which were obviously not electrons. The lead glass layer energies, E_1 and E_{12} (E_i = energy in i^{th} layer of lead glass, $i = 1, 2, 3, 4, 12 = 1$ and 2) in both arms, must pass a low threshold cut and at least one arm must pass a higher threshold cut. The thresholds were made magnet current dependent. Events surviving these cuts were written onto magnetic tape in the same format as the raw data. As a result, 250 tapes were reduced to 40 tapes.

Another pass through the data is made on the first pass tapes. Tighter cuts were made to reduce the amount of data still further. A so-called first layer and first-second layer mass were calculated from the energies and positions of shower clusters in the lead glass. This effective mass must then pass a magnet current dependent threshold. The data were now reduced to only 6 tapes.

A study of this compression process was made. We ran the full analysis program (described below) on both the raw data tapes and the final compression tapes for a small sample of

the data. Table III gives the results of the study. The FF (the classification is defined below when we discuss electron identification) class of events was 96% efficient above a mass of 2.8 GeV and 98% above 2.9 GeV. The tighter cuts were essentially 100% efficient. The reason for this is that the compressed data had an effective mass and E/p (defined below) threshold. A loose cut has higher probability of being below this threshold. Stated differently, we were inefficient for hadron events but efficient for electron events.

On the third pass of the data, we finally made use of the full analysis programs. A description of the analysis of an event follows. The amount of energy in each lead glass block was calculated with the appropriate calibration constant. Details of the lead glass calibration are described in Appendix III. A reconstruction program was then used to find particle tracks in the spectrometer. Since the two arms of the spectrometer were symmetric, the same programs were used for each arm. Depending upon the options set, the wire chamber reconstruction would use the trigger counters, T_0 and T_1 , and/or the scintillation hodoscopes, V_1 and V_2 . These requirements eliminated out of time tracks and resolved ambiguities. A least squares fit was then applied to the track. The χ^2 tells how good the track was. A description of the wire chamber reconstruction program

appears in Appendix IV. A magnetic reconstruction program was then used to trace the particle trajectory back through the magnet to the target. A description of the magnetic reconstruction is given in Appendix V. Up to three tracks per arm were fully reconstructed. The tracks were then graded according to the fiducial cuts passed. Table IV gives the fiducial volume used in the analysis.

The next step in the analysis was to determine whether the particle was an electron or not. The entry point of the track into the lead glass array was used to determine which blocks were to be summed for the energy determination. Lateral spread of the electromagnetic shower is taken into account by increasing the radii of blocks summed as the shower developed into the array. For details of the energy determination of a track, see Appendix VI. The energy cone described encloses > 99% of the shower energy. The ratio of the energy in the lead glass (E) to the momentum in the magnetic spectrometer (p) is an important parameter designated by E/p . For electrons, $E/p = 1$. This is smeared out by the resolution in E and p . A 30 GeV electron, for example, has a FWHM in E/p of 6.5% (see Appendix VII). The EE E/p cut was $1.0 \begin{matrix} -0.10 \\ +0.12 \end{matrix}$.

The next step in defining the electron character was to use the information on the longitudinal shower development. Hadronic showers tended to start later and last longer and be laterally wider, whereas about 90% of an electromagnetic shower is contained in the first two layers of lead glass.

Cuts were made on too little energy in the first layer energy fraction (E_1/E), the first two layer energy fraction (E_{12}/E), and on too much energy in the fourth layer (E_4/E). An explanation of these cuts appears in Appendix VIII.

Each track was then graded according to electron criteria. For subsequent calculations, the tracks with the best electron character was used. Of the 1132 events, which passed the EE criteria, 10 had a third track. Of these 9 had a third track, which also qualified as an electron. This is an indication of how clean the data were. Table V gives a breakdown according to current settings and mass.

When we have a track in each arm of the spectrometer passing the cuts described, we accepted the event as an electron-positron pair. Various quantities were then calculated for the event: transverse momentum, mass, Feynman x , center of mass rapidity, etc.

The third pass generated a summary of the data (DST = data summary tape) for all events which passed the FF or G_1G_1 cut. (The classifications are defined in Appendix VIII.) Each event contained the reconstructed track, fiducial, longitudinal and transverse lead glass information. It was from the DST that all subsequent pair data analysis was made. All data and results presented use the EE cut events unless otherwise stated.

B. Results

The mass spectrum for 300 and 400 GeV, for the events passing all the cuts discussed in Sec. IV.A, are shown in Fig. 11 for four spectrometer settings. A clear ψ (3100) and ψ' (3700) signal was seen at both energies. Even though the J/ψ and ψ' had very low acceptances for the 1100 A setting, the integrated sensitivity was better than for the 600 A and 800 A settings. Thus we saw a strong J/ψ and a ψ' signal for both 300 and 400 GeV data at 1100 A. Figure 12 shows the J/ψ region on an expanded scale. The muon data³¹ in the J/ψ region are shown for comparison.

For the J/ψ and ψ' , we show the p_t , y and decay angle distributions in Figs. 13-17.

To convert our data into meaningful results, we must unfold the apparatus acceptance. The acceptance was calculated by Monte Carlo methods. A model for pair production was used to throw events. Using this model we calculated cross sections from our data. These cross sections became the new model for the Monte Carlo. Iterating this process, we converged quickly. We ended up with self-consistent results. The Monte Carlo simulated the experimental situations by taking into account fiducial cuts, resolution effects of the wire chambers and magnetic reconstruction, multiple scattering by the amount of material in the secondary beam. A crucial test of the Monte Carlo is the prediction of the J/ψ

width as seen by our apparatus. At 600 A the J/ψ width ($\sigma = 40$ MeV) agreed with Monte Carlo predictions (see Table VI for comparison). Figure 18 shows the geometric momentum acceptance. Shown in Figs. 19 and 20 are the various mass acceptances. For the J/ψ and ψ' , the p_t and y acceptances are shown in Figs. 21-23. A detailed description of the Monte Carlo calculations appears in Appendix IX.

There is some model dependence of our results. We were not able to measure the decay distribution of the J/ψ very well. This was due to our limited acceptance in $\cos\theta$ (θ is the decay angle of the daughters as seen in the parent rest frame) and p_t . In addition there is the ambiguity of what reference frames should be used in defining the axis of quantization to obtain the simplest parameterization of the decay distribution.

The measurement of the decay distribution is important as it allows the determination of the J/ψ production alignment. The J/ψ is known to be spin 1 so that its decay distributions are $\sin^2\theta$ for $S_z = 0$ and $1 + \cos^2\theta$ for $S_z = \pm 1$. If we are able to measure the decay distribution, we gain information about J/ψ production in proton-nucleus collisions. A uniform decay distribution would imply no alignment of the J/ψ . $\sin^2\theta$ means the J/ψ is produced longitudinally polarized. Whereas, $1 + \cos^2\theta$ means transverse alignment.

Unfortunately there are an infinite number of choices for the quantization axis. The ones tried are the helicity frame and the Gottfried-Jackson frame.³⁴ There is no way to tell which is appropriate unless the J/ψ is produced aligned and we happen to stumble upon the reference frame in which the decay distribution can be simply described.

A study was made to look at the effect different models of J/ψ production and decay would have upon our results. Two reference frames were studied. In the helicity frame the axis of quantization is the J/ψ as seen in the J/ψ rest frame. This frame is natural for real photons. For parton-antiparton annihilation, the virtual photons are expected to be predominantly transversely polarized. The Gottfried-Jackson frame uses the beam direction as seen in the J/ψ rest frame. This frame is useful for quasi two-body reactions producing unstable particles. These two frames coincide if $p_t = 0$. We note that a uniform distribution in the J/ψ rest frame is independent of any axis. Thus three cases were studied: helicity with $1 + \cos^2\theta$, Gottfried-Jackson with $1 + \cos^2\theta$, and uniform. The data are then fitted to $1 + \alpha\cos^2\theta$ with $\alpha = 0, 1$ and α as a free parameter. The results of how well the data fit the models are given in Table VII and Fig. 24. It is seen that the data prefer the helicity frame with $1 + \cos^2\theta$ with confidence level of 37%. The value of α used has various consequences. The p_t slope of the invariant cross

section goes to $\exp(-1.2 p_t)$ if $\alpha = 0$ for the J/ψ . The total cross section, $d\sigma/dy$, increases by 60%. The effects on the high mass spectrum are studied in Ref. 30. All results presented in this report assume the $1 + \cos^2\theta$ model unless otherwise stated.

Shown in Table VIII are the fluxes used in obtaining the absolute normalization. The targeting runs mentioned in Sec. III.E were used to calibrate our targeting monitor, NDN. For Be III, we obtain NDN/PCSEM for 100% targeting. Then NDN was used to monitor the proton flux on the normal Be VII target.

The mass spectrum was calculated by using the following formula:

$$\frac{d^2\sigma}{dm dy} = \left[\frac{1}{f} \frac{1}{N_0 \rho} \frac{1}{\lambda (1 - \exp(-l/\lambda))} \right] \frac{1}{A(m, y)} \frac{1}{\epsilon} \frac{d^2Y}{dm dy} ,$$

where:

$A = 9.01$ is the atomic weight of beryllium,

$\rho =$ density of Be = 1.848 gm/cm^3 ,

$\lambda = 36.7 \text{ cm}$ is the absorption length of Be,

$l =$ target length: 4 in.,

$N_0 =$ Avogadro's number,

$f =$ flux = $\text{NDNBY}/(\text{NDN/PCSEM})_{\text{Be III}}$,

$A(m, y) =$ geometric acceptance ,

$\epsilon =$ efficiency due to all cuts ,

$Y =$ yield of events .

Note that we have taken into account the beam attenuation in the target. Secondary interactions were not important since

the target is very thin. Our results are presented per nucleon. The A dependence used to convert from nuclear targets to per nucleon is $A^{0.9 \pm 0.1}$. This A dependence is measured for the $\mu^+\mu^-$ decay mode of the J/ψ .³¹ We will hereafter denote the quantity in brackets [] by N.

The invariant cross section for the J/ψ and ψ' was gotten as a function of p_t by:

$$B E \frac{d^3\sigma}{dp^3} = \frac{1}{2\pi p_t} \frac{d^2\sigma}{dp_t dy} = \frac{N}{2\pi p_t} \frac{1}{A(p_t)} \frac{1}{\epsilon} \frac{d^2Y}{dp_t dy} ,$$

where B is the branching ratio into e^+e^- . We have assumed a flat ϕ dependence here and everywhere else. The y differential cross section is given by

$$B \frac{d\sigma}{dy} = N \frac{1}{A(y)\epsilon} \frac{dY}{dy} .$$

The full mass plot is shown in Figs. 25 and 26. A prominent J/ψ peak and a clear ψ' were seen at both 300 and 400 GeV. Table VIII gives the differential ψ/ψ' cross sections at $y = 0$. Note that at 400 GeV $-0.2 < y < +0.3$ and at 300 GeV $-0.1 < y < +0.4$. In Fig. 27 are shown the invariant cross sections for J/ψ and ψ' . Figure 27 also shows the differential y cross sections. Linear fits to the invariant cross sections were made:

$$B E \frac{d^3\sigma}{dp^3} = A e^{-bp_t} .$$

The results of these fits are given in Table IX.

The ψ' cross section was calculated with respect to the J/ψ cross section using the relative number of events and

relative acceptances at a given setting of the spectrometer. This technique reduced the amount of systematic errors that would appear in the ψ'/ψ ratio (i.e., no need to worry about absolute normalization and mass independent efficiencies). The models used are the ones given in Table II. The J/ψ cross section is inclusive, so that it includes J/ψ from ψ' decay.

C. Studies

1. Introduction

In this section we discuss systematic studies made on possible biases, efficiencies and background that would influence the results described in Sec. B.

2. Trigger

A study of the triggering efficiency was made. This study was divided into three parts: T , T_2 , and ϵ efficiency. The efficiency of $T = T_0 \cdot T_1 \cdot S_2$ was studied by using a completely independent fast trigger. This new trigger consisted of two Cerenkov counters per arm added for a subsequent dihadron experiment. The Cerenkov counters gave time resolution and required a threshold on the track momentum. Off-line, we reconstructed the tracks with the wire chambers and hodoscopes and asked if the trigger counters, through which the track traversed, fired. The efficiencies are given in Table X.

The next part of the electron trigger was T_2 . T_2 was required to pass a discriminator threshold. The fast

electron trigger was defined as the coincidence of T and T_2 . In addition we also digitized the T_2 pulse height. Triggering on T we got mostly minimum ionizing particles. Figure 28 shows the pulse height in T_2 for this trigger. If we then required that T_2 pass the discriminator threshold ($E = T \cdot T_2$), we see that the threshold was 15 minimum ionizing particles. We then asked how efficient T_2 was for electrons. Using a run in which the trigger was $T \cdot \epsilon$, we required that off-line we have an electron identified in the lead glass and asked if $E = T \cdot T_2$ had fired. We concluded that the T_2 efficiency was
(99.8 \pm 0.7)% for the up arm, and
(99.7 \pm 0.6)% for the down arm.

The third component of the electron trigger was ϵ , which required the energy in the first two layers of lead glass be above a threshold. Using a run in which the trigger was E , electrons are defined off-line using the lead glass energy and shower development. We then asked if the ϵ bit was set. Figures 29-30 show the efficiency plotted as a function of p . It can be seen that we were fully efficient for all momenta above the acceptance "threshold".

Thus the overall trigger efficiency was
(93.5 \pm 1.0)% up arm ,
(96.2 \pm 0.8)% down arm .

3. Electron Identification

Electron identification was, as previously explained, accomplished via the total energy deposited in the lead glass

and by the longitudinal shower development. We will discuss the latter. The E/p efficiency is $> 99\%$ since we have very good resolution (cut: $0.90 < E/p < 1.1$, $\sigma = \pm 3\%$). Electromagnetic shower development being statistical in nature, we were never able to make a sharp cut on the various energy distributions (E_i/E). Thus there was a compromise between efficiency and background rejection. For a given efficiency we looked for the best possible cuts for background rejection. As discussed in Appendix VIII, for a given efficiency, the signal to background is a very slow function of how cuts are made in the distribution E_i/E .

The shower cuts were developed so that the efficiency would not have any momentum dependence. The cuts were parameterized as a linear function of momentum. The range used for the parameterization was 20 to 50 GeV. Beyond 50 GeV, we ran into statistical problems as there were just not enough electrons to generate a distribution. Efficiencies for the various cuts are given in Appendix VIII.

The efficiency used in the calculation of the cross section is:

$$\begin{aligned} \epsilon &= \epsilon^2(\text{reconstruction})\epsilon^2(E/p)\epsilon^2(\text{EE shower})\epsilon^2(\text{trigger}) \\ &= (0.917 \pm 0.003)(1)(0.83 \pm 0.05)^2(0.935 \pm 1.0)(0.962 \pm 0.8) \\ &= 0.57 \pm 0.05 . \end{aligned}$$

The value used in the actual calculations was 0.5.

Of particular interest was the hadron rejection. There were several components that had to be considered. The T

trigger was almost all hadrons. By requiring $E = T \cdot T_2$, 25% of the T trigger survived. The DC logic requirement of ϵ reduced the E rate further by 5. Thus the on-line rejection was 5×10^{-2} . Off-line, the requirement on shower development and E/p left 2% of the $E \cdot \epsilon$ triggers. The overall rejection per arm was 10^3 , or an uncorrelated pair rejection of 10^6 . Figures 31-32 show E/p at each stage of the hadron rejection in the single arm experiment.¹ The number is an upper limit as our data contained electrons. If we subtract the hadron background under $E/p = 1$, we could improve the rejection to about 5×10^{-4} . The rejection we get is not as good as the single arm experiment for several reasons. At lower p_t , there is a larger π^0 flux. In demanding a higher efficiency for electrons, we must accept more background. Unlike the single arm experiment, no cut was made on greater than a single minimum ionizing particle in S_2 . But we, in fact, do not need to fine tune the rejection in one arm since the rejection of the other arm of the spectrometer is very powerful in selecting electron-positron pairs.

4. Accidental Background

A concern of all coincidence experiments is the problem of accidentals. This problem is enhanced when we explored small cross sections with high incident flux. As a result, a study was made of this background in our data. Appendix X explains how the accidental background was calculated.

The smooth curve in Figs. 25-26 shows that the data below 4 GeV (ψ/ψ' subtracted) are consistent with being all accidental. In the ψ/ψ' region, Table XI gives estimates of the accidental background. Since this background was so negligibly small, relative to ψ and ψ' , no bin by bin subtraction has been made on the invariant cross sections and differential y cross sections.

Additional information on accidentals is provided by time of flight (TOF) for the ϵ bit. Since the ϵ pulse was about 30 ns wide, there was the possibility that we triggered on the previous or next rf bucket (i.e., ± 18.9 ns).

Figure 33 shows the TOF's for both the up and down arm for e^+e^- pair data with all cuts except for TOF applied. The adjacent rf buckets are shown as cross-hatched regions. The curvature was due to pulse height slewing. For the 400 GeV data of the 1122 EE pair events, only 9 failed the TOF cuts.

Correlated background, as explained in Ref. 30, do not contribute in the region below 4 GeV. Figures 34-35 show how relatively clean of hadron background the J/ψ and ψ' regions were, when all cuts except for E/p were made. The cluster at $E/p = 1$, in both the up and down arm, is the e^+e^- signal. The horizontal region at $E/p = 1$ is electrons in one arm but not the other. Similarly the same is true for the vertical region about $E/p = 1$. This demonstrates how powerful is the requirement of an electron in one arm and a positron in the other.

V. SUMMARY AND CONCLUSIONS

A. Summary of Results

We have observed a strong J/ψ and ψ' signal in $p + Be \rightarrow e^+e^- + X$ at 300 and 400 GeV. Measurements of their production dynamics have been made. The invariant cross section at $x = 0$ is presented for $p_t = 0-2$ GeV. In our region $x = 0$, the differential x cross section is flat over the limited range of x acceptance. The data are seen to prefer a $1 + \cos^2\theta$ decay distribution in the helicity frame with Confidence Level = 37%, although as noted, our small acceptance in p_t couples the p_t and decay distribution strongly.

Measurement of J/ψ and ψ' production in hadron collisions is of much theoretical interest. The x , s and p_t dependence can be used to distinguish between various mechanisms for psion production. Figure 36 shows the s -dependence of J/ψ and ψ' production as measured in this and other experiments.³⁵ The J/ψ measurements taken together give a good global picture of J/ψ production versus incident hadron energy. The ψ' data has not as yet been clearly seen in another hadron production experiment. This is because no other experiment has yet the combination of luminosity and resolution. The ψ' p_t slope is consistent with that of the J/ψ .

B. Theoretical Significance

Green, Jacob and Landshoff³⁶, in an early model, were able to predict a sharp s dependence at $x = 0$. Their

calculations are in reasonable agreement with the J/ψ data. Their prediction of a plateau in a region near $x = 0$ was also confirmed. The model they used is similar to the Drell-Yan mechanism (Fig. 4) of $q\bar{q}$ annihilation. More sophisticated models evolved, spurred by the low ψ' to J/ψ cross section. In any non-cascade model, one would expect ψ/ψ' to be of order 1, scaling as m'^2/m^2 , since the ψ' is thought to be a radial excitation of the J/ψ . Ellis, Einhorn and Quiqq³⁷ and Carlson and Suaya³⁸ conjectured that J/ψ and ψ' were not produced directly but rather have cascaded from χ_c states. χ_c states are in turn produced by gluon-gluon "amalgamation" (Fig. 37). Cascade production has built into it an explanation of the low J/ψ to ψ' cross section. χ_c , with mass between that of the J/ψ and ψ' , contributes only to J/ψ . If χ_c is more massive than ψ' , the competitive decay to J/ψ and ψ' favors J/ψ . For χ_c above charm threshold, decay to J/ψ and ψ' would be negligible.

The cascade model is not unique. Bourquin and Gaillard³⁹, using a phenomenological model, have been able to obtain predictions in agreement with our measured results for J/ψ to ψ' . Along with the data, Fig. 36 shows the models of Donnachie and Landshoff⁴² (dotted curve), Carlson and Suaya (solid curve). More data on ψ' would provide a better picture of the psion dynamics: the s dependence of the cross section and p_t dependence of the invariant cross section.

As stated in the introduction, sources of single lepton production are of particular interest. The sources must be produced with hadronic cross sections like π 's and K's at high p_t and have a high leptonic branching ratio. The J/ψ satisfies this requirement. Using a Monte Carlo program, we calculated the contribution of J/ψ to single lepton production. Figure 38 shows the results of the calculation using the invariant cross section determined in this experiment. At high p_t ($p_t > 3$), J/ψ is consistent with the single lepton data. Bourquin and Gaillard have made a systematic study³⁹ of the various sources of single leptons: ρ , ω , ϕ , J/ψ . Adding these sources together, they come up short of the single lepton data in the interval $1 < p_t < 2$ GeV/c. They conjectured that the deficit, using their model of hadron production, could be made up by the production of charmed mesons: $D \rightarrow K\ell\nu$. This explanation is by no means unique. The low p_t single lepton data are still controversial and thus no conclusions can be drawn.

The surprisingly large $\langle p_t \rangle$ of lepton pairs aroused both experimental and theoretical interest. Anderson et al³⁵ have measured the $\langle p_t \rangle$ versus m up to 3 GeV. They find that the $\langle p_t \rangle$ increases continuously with mass independent of whether a resonance or continuum mass region is considered. Hom et al³¹ have measured $\langle p_t \rangle = 1.6$ GeV for mass greater than 5 GeV. This is in accord with the continuing rise of $\langle p_t \rangle$ with mass.

The original Drell-Yan model was two-dimensional (space-time), thus $p_t = 0$. There have been recent attempts to incorporate transverse momentum into the model. The model of Gunion⁴¹ and Kogut⁴² attempts to do this by giving the partons a transverse momentum distribution.

M. Duong-van et al⁴³ generates massive lepton pairs by a meson-quark scattering. The scattering process gives rise to transverse momentum which a Drell-Yan annihilation process cannot.

In the near future, much better data should be available from the same Columbia-Fermilab-Stony Brook collaboration. The electron-positron pair experiment has been duplicated with better than a factor of two improvement in resolution. A muon pair experiment is currently underway with high sensitivity and good resolution out to a mass of > 15 GeV. Thus a great deal of new and exciting physics can be expected in the near future.

VI. ACKNOWLEDGEMENTS

As with any contemporary high energy physics experiment, success depends upon a great number of people, each giving his or her unique contribution. I would like to acknowledge these efforts and the large debt I owe to the people who performed them.

I would like to thank Professor Leon M. Lederman, my sponsor, for providing a stimulating atmosphere for doing physics. His questions and ideas always evolved into new insights.

Drs. Jeff Appel, Irwin Gaines, Walter Innes, Hans Paar, Jeff Weiss, and John Yoh taught me much about how to assemble, run, and analyze an experiment. Their efforts were essential in my development as a physicist.

Dave Snyder, my fellow graduate student, provided the camaraderie during the long hours of setting up of the experiment and during the long period of detailed analysis.

The engineers and technicians were no less important than the physicists. Herb Cunitz's patience in teaching a young graduate student electronics is deeply appreciated. Bill Sippach's electronic design was an absolute beauty to behold. The Nevis Electronics Group built and tested the special electronics we required. Richie Meyers and Art Timm and the Nevis Machine Shop constructed much of the detector hardware.

All the work at Nevis would not have been possible were it not for the people in the Receiving, Personnel and Purchasing Departments.

Aside from Irwin Gaines, Dan Curtis of the Fermilab Computing Department provided many helpful discussions on the on-line program.

I would like to thank our technicians Pierre Bury, Ken Gray, Pete Lucey, Frank Pearsall, Bruce Tews, and Jack Upton. I would especially like to thank Ken Gray and Frank Pearsall and their families for the friendship they offered.

Without the hard work and dedication of people in the Accelerator Division and Proton Laboratory at Fermilab, the experiment would not have been possible.

Finally, I would like to thank Ann Therrien for not only typing and editing this manuscript, but for being someone I could talk to.

APPENDIX I

Lead Glass Calorimeter

Electron identification in this experiment was provided by identical lead glass calorimeter and magnetic spectrometer apparatus on each arm. An entering particle's longitudinal shower development and total energy deposit in the lead glass provided information which served to identify it as an electron or non-electron event.

The lead glass calorimeter in this experiment served as a total absorption Cerenkov counter for containing the cascade showers initiated by incident electrons. Many descriptions exist in literature relating how the passage of a single electron through matter can give birth to observed large numbers of electrons and positrons. Both analytic calculations^{44,45} and Monte Carlo simulations^{46,47,48} have been used to test the assumed physical model.

Electrons enter matter, typically undergo bremsstrahlung to produce one or more photons, the photons convert to e^+e^- pairs, and the process starts over again, but with an increased number of electrons of decreased average energy. The growth of the shower will continue until pair production is no longer the dominant mode of photon interaction, and the shower will die out as electrons fall in energy and lose larger fractions of their energy to the medium in small, relatively continuous ionization energy transfers. Heitler⁴⁹ points out that such

cascade showers were first observed in Wilson Chamber experiments, and that the most direct evidence for their physical nature comes from photographic plates that record the actual shower particle tracks (Fig. 39).

Figure 40 presents some formulae of Cerenkov and bremsstrahlung radiation. When integrating the Cerenkov formulae over frequency, it is important to note that the condition $n > 1/\beta$ bounds the available range of integration. A schematic plot of the index of refraction (n) for a typical optical medium is shown in Fig. 41. The restricted range of integration at high frequencies usually insures that Cerenkov energy losses will be small compared to losses due to other available radiative mechanisms.

Electrons and positrons will generate Cerenkov light in lead glass until they reach kinetic energies near 0.13 MeV. Monte Carlo simulation programs, which trace electron showers down to energies close to this lower limit energy, indicate that the total track length traversed by the e^+e^- particles in an electromagnetic shower is proportional to the energy of the original, initiating electron. Since the energy loss to Cerenkov radiation is independent of electron energy over a wide energy range (see Fig. 40b), the total Cerenkov light emitted in a cascade shower will be proportional to the total track length of the e^+e^- particles, and thus proportional to the initiating electron's (or positron's) energy. This suggests

the use of a transparent medium, of preferably short radiation length, to serve as an energy calorimeter. Lead glass was chosen for this experiment.

While bremsstrahlung energy losses are greater than those due to Cerenkov radiation in lead glass (bremsstrahlung photons range in energy from 0 up to the maximum allowed by the radiating electron), energy losses to Cerenkov radiation in a band near the visible region of the spectrum (400-800 nm) are typically orders of magnitude larger than bremsstrahlung losses in the same restricted frequency range. A photomultiplier tube is sensitive to radiation near the visible region of the spectrum, and so can be used to sample emitted Cerenkov light in lead glass. The phototube's limited spectral sensitivity makes it insensitive to the more prevalent bremsstrahlung radiation.

The digitized pulse area measured from each lead glass block's photomultiplier tube will be proportional to the block's shower energy deposit; the constant of proportionality is referred to as the lead glass block's 'calibration' constant. The determination of a set of these constants for all lead glass blocks, and the monitoring of their variation with time, will be discussed in Appendix III.

The configuration of lead glass blocks for one arm is shown in Fig. 7. Each array consisted of 24 ($15 \times 15 \times 35 \text{ cm}^3$) blocks and 72 ($15.25 \times 15.25 \times 45 \text{ cm}^3$) blocks. Some properties

of the lead glass are summarized in Table I and in Fig. 42. Many details pertaining to this calorimeter are described adequately elsewhere³² and will not be reconsidered here.

An RCA 8055 photomultiplier tube was glued to the small face of each lead glass block with Kodak HE 10 assembly cement ($n = 1.58$). Aluminum foil (1 mil thick) was wrapped about the glass up to the tube base, and this foil was put at cathode potential (through a 1.5 M Ω resistor) to limit leakage currents flowing across the photocathode. The block sides and remaining small face were covered with mylar (5 mil) to mechanically protect the aluminum foil surface and provide electrical insulation for the ungrounded foil. To light tight each block, black polyethylene (6 mil) was used. A cylindrical mu-metal shield was placed around the phototube, and soft iron foil was wrapped about the upper portion of the lead glass block to extend the magnetic shielding beyond the photocathode about one tube diameter.

Blocks in each lead glass layer were stacked tightly together with no significant gaps. The layers themselves were separated by 2-3 in. RG-8 cable (low dispersion) was used to transmit the anode signals from each block to the experiment's trailer.

The ϵ signals of the DC logic were derived, on each arm, from the dynode signals of blocks in the first two lead glass layers. These dynode signals were passively fanned in, inverted, amplified and cabled to the trailer on disc loaded

coaxial cable. There this signal's pulse height was discriminated; the threshold setting of the discriminator on each arm determined the minimum energy deposit in the first two lead glass layers necessary for the DC logic ϵ bit to be set.

Both lead glass arrays were maintained in temperature and humidity controlled huts. A lead sheet (2.3 radiation lengths) was placed directly in front of the first layer of lead glass to increase the observable differences between hadrons and electrons. Lead was chosen for its small ratio of absorption to radiation length.

APPENDIX II

Digitizers and Digitizer Readout System

This appendix will describe the readout system for the Nevis ADC's and its various options.

We have in the system 256 channels of ADC's. The digitizers and scalers in their normal operation will digitize 500 pC full scale. Full scale being 1024 channels as the scalers are 10 bit scalers. Of the 256 channels, 192 are for the lead glass. These 192 digitizers are the quad types. Each unit has a common gate, four BNC signal inputs and four NIM level pulse train outputs in the rear. The scalers for the new digitizers are slightly different from those of the previous experiment.^{1, 32} There is a line in the dataway which, if enabled, will allow the scaler to overflow 1024, resetting it to 0. This option would have given us an effective 2048 channels if used in conjunction with the variable format module (VFM). The other 64 channels are the ones used in the previous experiment. All scalers were placed in NEVAC crates 3 and 4, so as not to use up valuable space in the master crate (crate 1). (NEVAC is the Nevis version of a CAMAC crate made with ECL (Emitter Coupled Logic) but compatible with CAMAC on the branch highway level.) For calibration purposes, the slope voltage of the ADC's is set to 1.2 V (instead of 24.0 V) to give us 20 times greater gain. A bias voltage is also changed to balance the circuit. This

high gain setting was used for muon straight-through calibration (see Appendix III).

Other features of our ADC's are:

1. Base line restoration: an electronic servo clamps the input stage base line to its value for the last few μ s. Thus only signal above the base line is digitized. This allows us to filter 60 cycle and other low frequency noise.

2. Pedestal injection into linear range of ADC: pedestals were normally in channels 30-40 with a standard deviation of about 1%.

3. Ground isolation: the ADC's have only one ground, that of the DC coupled input. The pulse train outputs are transformer coupled. We are able to minimize ground loop problems.

We now discuss the readout system itself. The Nevis CAMAC dataway is 16 bit for the read lines. To use computer core space efficiently and reduce readout time, the data for each octal scaler is packed from eight 10 bit words into five 16 bit words. This is accomplished by the scaler packer module and the branch driver. Crates 3 and 4 are not connected to the branch highway directly, but through crate 1's dataway. In crate 1, we have two master crate links (MCL) which connect to slave crate links (SCL) in crates 3 and 4. This eliminates the need for two additional complicated crate controllers. The crate controller in crate 1 acts as the crate controller

for crates 3 and 4. To a branch driver, it would appear as if crates 3 and 4 were normal crates on the branch highway.

As 256 ADC's are a large number to read out (when most of them will be pedestal anyway), we designed the crate linkage so as to allow the hardware (i.e. hodoscopes) to determine the groups of lead glass blocks to be read out. This is accomplished by addressing the MCL directly, which activates the dataway variable line (V). This is a signal for the variable format module to take over all dataway addressing operations. When an ADC read is executed, the status of the 16 individual inputs to the VFM determine the groups of octal scalars to be read. The bit pattern of header words sent out initially by the VFM informs us as to which octal scalars are to follow the header word. Using the VFM, we were able to cut down event size by about 50%.

The digitizers were calibrated for their high gain setting. The slope of the linear response of the ADC was measured by changing the pedestal injection voltage. This was done for both the normal and high gain settings. The ratio of the slopes was the relative gain of the two settings. This was then incorporated into the muon straight-through calibration. In addition, tests of digitizer linearity and stability were made. The non-linear term in the quadratic fit to the pedestal data indicates a 1/2 (digitizer) scale error of 0.6% and a full scale error of 1.3%. Digitizer gains fluctuate with time on the level of $\sigma = 0.4\%$ over a period of 2 months.

APPENDIX III

Lead Glass Calibration

Two types of special data were used for calibration of the lead glass arrays. Muon calibration (done once every two days) provided information used to equalize the gain of each lead glass block with respect to those directly in front or in back of it. A relatively pure muon sample was obtained by removing the target and allowing the incident beam to interact completely in a tungsten beam dump 2.1 m downstream of the target position.

Electron calibration (done once every week) provided data used to absolutely calibrate the lead glass arrays. For this calibration, the sample of electrons in the beam was increased by use of a wider copper target and by the insertion of copper foils (15-45 mils thick) into the aperture, 7 ft downstream of the target. The thicker target and thin foils served to increase the amount of material in the aperture, to convert more γ rays into e^+e^- pairs.

A. Muon Calibration

For a fixed incident trajectory with respect to lead glass, a muon will deposit a constant amount of energy in the block, regardless of the muon incident energy. 135 MeV was assumed to be the muon energy deposit in 15 cm of lead glass (block sizes were uniform to 1/2%).

In muon calibration, the trigger was set to illuminate the half of the lead glass block most distant from the photocathode; histograms of digitized pulse area were made

for each block. Analysis of these histograms, on-line, provided a means of adjusting high voltages to equalize lead glass block gains (to $\pm 10\%$). This same data served to provide finer individual block gain corrections off-line. Repetition of one muon calibration after another served to check reproducibility of muon gain values measured by this procedure. Muon median channel values were reproducible with a σ of 1.2%.

To measure the muon energy deposit, lead glass digitizer gains were increased by a factor of 20 above normal. The linearity and gain of each digitizer was measured for both the normal and high gain settings. $\pm 0.5\%$ fluctuations in gain were measured over a one month time period.

B. Electron Calibration

Contrasted with muons, electrons deposit all their energy in the 25.8 radiation lengths of lead glass, and so their measured shower energy should equal their incident momentum ($E = p$). Plots of E/p , which were made using data with enhanced electron beam, showed a prominent peak near 1.0 (Fig. 43). Each set of four blocks (in a row, along the beam direction) was calibrated by multiplying their calibration constants by a factor that would center the set's electron peak at 1.0. These corrections typically amounted to a few percent and varied by 2-4% over the experiment's lifetime. The weekly electron calibration runs provided data

for adjustment of these corrections with time. In addition to providing absolute energy calibration, this adjustment roughly corrects for the small amount of energy lost by electrons in the 2.3 radiation lengths of lead before the arrays.

In using lead glass to measure the energy of showering particles, corrections must be made for light attenuation effects. The closer the entering particle is to the photocathode, the greater the measured light output. The correction factor used to adjust for this effect is plotted in Fig. 44. This curve describes an average behavior of the lead glass in the arrays. Individual sets of 4 blocks typically deviate from this average behavior by less than 0.5%.

Even with this correction, the lead glass resolution degraded significantly when the entering particle passed within 5-7 cm of the photocathode. This was probably due to energy leakages out of the glass. For this reason, a fiducial cut was made on the data 6.35 cm from the outer edges of the array. Monte Carlo results⁵⁰, from the simulation of 20 GeV electron initiated showers, indicate that 97% of the electron shower energy is contained within a 6.35 cm radius.

APPENDIX IV

Proportional Wire Chamber Reconstruction

The wire chamber reconstruction program was used to reconstruct tracks downstream of the air gap magnet. Reconstruction begins by looking for wires in the Y, P, Q chambers which are consistent with a track passing through that detector station (80 ft or 120 ft station). The requirement was that the wires be within 0.200 in. of each other in the y dimension (the coordinate system is described in Appendix V). These wires are then taken off a table of wire hits. After exhausting the search for all so-called triplets, the remaining wire hits are paired off to form all possible "doublets".

The next step is to pair off triplets and doublets at 80 ft and 120 ft, starting with triplet pairs first. The pairs found are then verified against a loose target and magnet cut. Checks against the T_1 trigger counters and V_1 and V_2 counters insure that the track passed through the correct counters. This eliminates spurious and out of time tracks in the MWPC's. The wire chamber at 100 ft is used to resolve ambiguities only and is not required in the reconstruction.

Once a track is found, a least square fit is made. In the fitting procedure multiple scattering, which introduces correlations, is taken into account. The track fitting parameters are taken to be the x, y at 80 ft and 120 ft, respectively.

$$a = \begin{bmatrix} x_1 \\ y_1 \\ x_2 \\ y_2 \end{bmatrix}$$

The fitted points predicted for the measurements are \bar{y} :

$$\bar{y} = \begin{bmatrix} \bar{y}_1 \\ \bar{p}_1 \\ \bar{q}_1 \\ \bar{y}_2 \\ \bar{y}_3 \\ \bar{p}_3 \\ \bar{q}_3 \end{bmatrix}$$

Then $\bar{y} = Ca$ where C is the matrix describing the geometry required to go from a to \bar{y} . The quadratic form

$$M = (y - \bar{y})^T W(y - \bar{y})$$

is then minimized. $W^{-1} = E =$ covariance matrix. The covariance matrix has two components. The first is the inherent wire chamber resolution and the second, which introduces non-diagonal elements, is the multiple scattering. Differentiating with respect to a_i , we get

$$\frac{\partial M}{\partial a_i} = 0 .$$

Solving,

$$\begin{aligned} a &= (C^T E^{-1} C)^{-1} C^T E^{-1} y \\ &= H^{-1} C^T E^{-1} y . \end{aligned}$$

For the calculation of the covariance matrix, the multiple scattering formula used was

$$\theta^2 = \left(\frac{0.015}{p}\right)^2 \frac{\ell}{L} ,$$

where:

θ = rms scattering angle ,

p = momentum of particle ,

ℓ = amount of material in units of length (Table XV) ,

L = radiation length of material .

For example the scattering error at Y_3 , due to the material between 80 ft and 100 ft, is given by

$$\begin{aligned} \sigma_{Y_3}^2 &= \int_{z_1}^{z_2} \left(\frac{0.015}{p}\right)^2 \frac{dz}{L} (z_3 - z)^2 \\ &= \frac{7}{12} \left(\frac{0.015}{p}\right)^2 (z_3 - z_1)^2 \frac{\ell}{L} . \end{aligned}$$

Similarly,

$$\sigma_{Y_1}^2 = \sigma_{Y_2}^2 = \frac{1}{12} \left(\frac{0.015}{p}\right)^2 (z_3 - z_1)^2 \frac{\ell}{L} .$$

For the correlation terms, we use the constraint

$$Y_1 = 2Y_2 - Y_3 .$$

Thus,

$$\sigma_{Y_1}^2 = 4\sigma_{Y_2}^2 + \sigma_{Y_3}^2 - 4\sigma_{Y_2 Y_3}^2 .$$

The error for the fitted parameters, a , is by

definition

$$\begin{aligned} \sigma_{ij}^2(a) &= \sum \frac{\partial a_i}{\partial y_\ell} \sigma_{\ell k}^2(y) \frac{\partial a_j}{\partial y_k} , \\ \sigma^2(a) &= (C^T E^{-1} C)^{-1} = H^{-1} . \end{aligned}$$

The error matrix has two non-zero correlation terms, $\sigma_{X_1 X_2}^2$ and $\sigma_{Y_1 Y_2}^2$. The resolution, as a function of momentum is shown in Fig. 8.

We now consider the question of reconstruction efficiency. The algorithm, as given above, will find a track if there are no wire chamber inefficiencies. Thus, we are reduced to the question of calculating the efficiency for $n > n_{\min}$ chambers, where n_{\min} is the minimum number of chambers necessary for reconstructing a track.

At the 80 ft or 120 ft detector stations, we require ≥ 2 of the 3 chambers fire. The average chamber efficiency is $e = 0.98$. Thus, each detector station efficiency is

$$\begin{aligned} \epsilon &= \sum_{i=2}^3 \binom{3}{i} e^i (1-e)^{3-i} \\ &= 3e^2 - 2e^3 \\ &= 0.9988 . \end{aligned}$$

Since V_1 and V_2 are required, their efficiencies must be included (see Table X). Therefore, for pair events

$$\begin{aligned} \epsilon^2(\text{reconstruction}) &= \epsilon^4 \epsilon^2(V_1) \epsilon^2(V_2) \\ &= 0.917 \pm 0.003 . \end{aligned}$$

This factor is included in the overall apparatus efficiency.

APPENDIX V

Magnetic Reconstruction

A derivation of the equation, used to fit the measured field in the magnet, is presented. The tracing of tracks reconstructed downstream of the magnet (see Appendix IV) through the magnet to the target is described.

The magnetic field is mapped with a flip coil hooked up to an integrator. Thus, we measure

$$\vec{C} = \int_{-\infty}^{+\infty} \vec{B} dz \quad .$$

Using Maxwell's equation:

$$\vec{\nabla} \cdot \vec{B} = \vec{\nabla} \times \vec{B} = 0 \quad ,$$

and $B_z(z = \pm \infty) = 0$, it can be shown that in two dimensions (x and y)

$$\vec{\nabla} \cdot \vec{C} = \vec{\nabla} \times \vec{C} = 0 \quad .$$

Our coordinate system is: the z axis is the spectrometer axis (72.5 mrad with respect to the proton beam line); x is in the horizontal plane pointing towards large angle; y axis such that we have a right handed coordinate system, the origin is at the target center (z = 0). Thus

$$\vec{C}(x, y) = \vec{\nabla} \phi$$

$$\phi = \sum_{ij=0}^{\infty} C_{ij} x^i y^j \quad .$$

With the constraint that

$$\begin{aligned}
 C_x(0,0) &= a_1 & C_y(0,0) &= 0 \\
 C_x(x,y) &= C_x(x,-y) & C_x(x,y) &= C_x(-x,y) \quad .
 \end{aligned}$$

We assume the magnets are symmetric in the four quadrants.

Then

$$\begin{aligned}
 C_{10} &= a_1 \\
 C_{01} &= 0
 \end{aligned}$$

and

$$C_{i+2} C_j^{(i+2)(i+1)} + C_i C_{j+2}^{(j+2)(j+1)} = 0 \quad .$$

Thus,

$$\begin{aligned}
 C_x(x,y) &= a_1 + a_2(x^2 - y^2) + a_3(x^4 - 6x^2y^2 + y^4) \\
 &+ a_4(x^6 - 15x^4y^2 + 15x^2y^4 - y^6) \\
 &+ a_5(x^8 - 28x^6y^2 + 70x^4y^4 - 28x^2y^6 + y^8) + \dots
 \end{aligned}$$

and

$$\begin{aligned}
 C_y(x,y) &= -2a_2xy + 4a_3(xy^3 - x^3y) \\
 &- a_4(6x^5y - 20x^3y^3 + 6xy^5) \\
 &+ a_5(8xy^7 - 56x^3y^5 + 56x^5y^3 - 8x^7y) + \dots
 \end{aligned}$$

Subsequent measurements showed that the magnetic field was very uniform. Thus keeping terms up to a_2 was sufficient. The absolute field at the center of the magnet as a function of current was found to have a saturation of the steel polefaces described by

$$a_1 = 8.10 \times 10^{-4} \left[1 - \left(\frac{I}{5000} \right)^{3.5} \right] I$$

(where I is in amperes and a_1 is in GeV/c) and a_2/a_1 is measured to be 0.00007. The field shapes of both analysis magnets were found to be identical.

The magnetic reconstruction was performed in two iterations. On the first iteration the horizontal and vertical production angles and the bend angle are evaluated by using an effective bend plane approximation. In the vertical bend direction, it is assumed that the track came from $y = 0$. In the non-bend plane, the x coordinate of the track at $z = 0$ can be calculated. Subsequent fiducial cuts are made on the x coordinate at the target (see Table IV). On the second iteration, the magnet is divided into two halves in z . The average $\langle y \rangle$ and x at midmagnet are used to calculate the integral field. An effective bend plane calculation is then performed for the two halves of the magnet. The magnet effective bend plane is then recalculated. With the effective bend plane, the production and bend angles and momentum are recalculated. The errors calculated from a fit of the measurements downstream of the magnet are propagated through the magnet to give errors on the production angles and momentum.

The magnetic reconstruction program provided for a momentum resolution of better than $\sigma = 0.5\%$. Figure 8 shows the magnetic spectrometer resolution. At low momentum, it is dominated by multiple scattering and at high momentum by the intrinsic wire chamber resolution.

APPENDIX VI

Lead Glass Energy Determination

To accommodate the long rise time of the RCA 8055 photomultiplier tube, the lead glass digitizer gate was set at 270 ns. A gate this length extended over 13 accelerator rf buckets. During this time, the lead glass was 'open' to secondary events that could shower (pile up) in the lead glass after the triggering particle. This possibility made it undesirable to simply sum the energy deposited in all lead glass blocks to calculate an event's calorimeter deposit. In the off-line analysis, the reconstructed track (as determined from wire chamber and hodoscope information) was used to select those blocks to be included in the event energy determination. Circles were traced around the track at the rear of each lead glass layer, and the overlap of these circles with lead glass blocks selected those blocks included in the energy summation.

For these circles, radii of 3.0, 3.5, 3.75 and 4.0 in. were chosen (for layers 1, 2, 3 and 4, respectively). These radii gradually increase to accommodate the expanding particle shower and will be referred to as defining a 'cone' about the particle trajectory. Comparison of this radii set with others was done and the results are shown in Fig. 45 and 46, for two different momentum ranges.

Figure 47 provides information on the lateral spread of electron showers in the lead glass. The curves present the fraction of layer energy deposited in a single lead glass

block as a function of the entering particle's distance from block center (the center of the distributions corresponds to block center; the 50% point appears at the edge of the block). The change in shape of the curves, going from momenta of 20 to 40 GeV is slight and did not merit the use of momentum-dependent radii.

The chosen set of radii included ($99 \pm 1.4\%$) of the electron shower energy. A study was made to determine the fraction of energy deposited outside this cone as a function of E/p . Results of this study are shown in Fig. 48. They indicate that as E/p approaches 1.0, more of the total event energy is included in the electron shower cone. The hadrons close to $E/p = 1.0$, passing electron longitudinal shower cuts, seem rather similar to electrons in their transverse shower dimensions. One concludes that, using the present radii set, this experiment's hadron rejection would not be improved by cuts on the transverse size of a particle's lead glass shower.

As intensity increases and spill quality worsens, one expects an increase in lead glass energy pileup due to secondary events showering in the glass within 270 ns after the triggering particle. The effect of this on the dielectron data can be judged from the values of Table XII. Presented are average E/p values for 400 GeV dielectrons, where the data have been divided into 4 bins of NDN and $INDUTY \times NDN$ (where $INDUTY$ is the duty cycle of the beam spill). Severe

pileup problems in the data would be reflected in a shift of the average E/p upward, going from low to high intensity, or from good to bad beam quality. No such shift is observed. The actual plots from which these numbers were taken are shown in Figs. 49 and 50. The percentage of energy found outside the event cone, in the remainder of the lead glass blocks, is plotted in Fig. 51 for the 400 GeV dielectrons (the percentage is calculated relative to the event's cone energy). For each current, lead glass background levels are low.

A check on the absolute energy calibration of the lead glass and on the energy determination procedure can be made using the clear signal of the J/ψ particle. Presented in Table XIII are average E/p values for J/ψ events, for each arm of the spectrometer and for magnet settings at which J/ψ acceptance was adequate. Provided also are J/ψ mass values, calculated using the events' lead glass energy and the reconstructed pair opening angle.

APPENDIX VII

Lead Glass Resolution

Test beam data, taken over a range of energies from 3 to 75 GeV, was used to determine the validity of the following lead glass resolution formula:³²

$$\frac{\text{FWHM}(E)}{E} = 0.015 + \frac{0.1}{\sqrt{E}} \quad .$$

Of particular interest are the data points for 50 and 75 GeV, which were measured using this experiment's large lead glass blocks, stacked as in the spectrometer arrays.

In practice, all the benefits of this lead glass resolution will not be realized due to random errors inherent in the calibration procedure. Using estimates of calibration errors given in Appendix III, one can calculate a predicted resolution of the lead glass by folding known errors in with the published resolution formula. Values for this predicted resolution, along with values calculated from the published formula are shown in Table XIV. One sees a 20-30% resolution shift over the 20-30 GeV momentum range.

A measurement of the actual lead glass resolution was made using an electron enhanced beam and studying the variation of the electron peak width in E/p histograms with energy. The results are shown in the same table. There is good agreement with the predicted resolution in the high momentum region, but not in the low.

APPENDIX VIII

Longitudinal Shower Development

One of the handles we have in identifying electrons is that they show a characteristic longitudinal shower development. We make use of this by sampling the shower four times in the four layers of lead glass. This appendix will discuss how cuts were arrived at to discriminate between electrons and hadrons. We will also discuss whether we have made the optimal cut or not.

To look at electron shower development, we must first isolate a sample of electrons. This is accomplished by a subtraction technique. We take a run in which we enhance the number of electrons by using a wide high Z target (Cu) and inserting a 0.015 in. foil in the secondary beam. This results in conversion of γ 's from π^0 decay into e^+e^- pairs. During this run, half the time we insert 2 in. of lead in the secondary beam. This would absorb all electrons in the beam leaving only hadrons. We then histogram for each event the ratio of energy in the lead glass and the momentum in the magnetic spectrometer (E/p), and the various fractional energies E_i/E (where E_i is the energy in the i^{th} layer, and $E =$ total energy). Histograms were divided into lead and no lead and into momentum bins. For each momentum bin, we subtract the lead from the no-lead distributions. We normalize the subtraction using the E/p region away from 1 since the shape of the hadron distributions in E/p would not

be affected by the lead. This same normalization is used to subtract the E_i/E distributions. What is left after the subtraction are the various electron shower distributions for each momentum bin. See Fig. 52 for an example of the subtraction. Note that the E_i/E distributions all have a E/p cut applied to enhance the electron sample. The subtracted E/p distribution shows how good is the subtraction method given sufficient statistics.

Our first set of cuts was determined by cutting 5, 10, 20% into tails of the distributions. These cuts were then plotted as a function of momentum. A linear fit was used:

$$\text{cut } E_i/E: C_i = A_i p + B_i .$$

Due to the way electrons shower, E_1/E , E_{12}/E cuts were lower limit cuts and E_2/E , E_3/E , E_4/E were upper limit cuts.

Since cutting at the tails of distributions involves large statistical fluctuations, we developed a second set of cuts to determine the coefficient A_i better. This involves plotting the median of the distributions as a function of momentum. B_i is then allowed to float depending upon the efficiency desired.

The cuts that were in fact used were E_1/E , E_{12}/E , E_4/E . A look at the E_3/E distribution shows that the background is flat even under the electrons. To maintain high efficiency, the E_3/E cut would not gain much in background rejection since it has a relatively long tail. The E_2/E cut was not used since the information is carried by the E_1/E and E_{12}/E cut.

For a given set of cuts, we calculate the efficiency for electrons. Here again we use a subtraction technique on the E/p plots. The number of electrons is determined by subtracting E/p histograms with and without the lead filter in. The electrons are defined as the number of events in the region $0.90 < E/p < 1.10$ left after subtraction. We do the same thing again but this time apply the shower cuts. The number of events remaining after cuts allows us to calculate the efficiency. The efficiencies were calculated for several momentum bins 20-25, 25-30, > 30 GeV. There was no momentum dependence to the level of $\sigma = \pm 3\%$.

A study on the question of whether we have the optimal signal to background ratio for a given efficiency was made. The background was defined in a region below $E/p = 1$ but above any software or hardware thresholds: $0.60 < E/p < 0.88$. The results of the study were that for a given efficiency the signal to background ratio was a fairly flat function of the various shower cuts. A gain in signal to background of about $10 \pm 5\%$ could have been gotten if our cuts had been optimized. A minimal gain at best.

The efficiencies and definition of the various cuts used are given in Table XVI.

APPENDIX IX

Monte Carlo Calculation of Acceptances

In the calculation of cross sections, one must correct the data for the finite probability that an event will be seen by the apparatus. This probability is commonly called the acceptance probability of the apparatus or just the acceptance. We begin with a general discussion before we discuss the specific case of this experiment.

Let

$\frac{dN}{dx_j}$ = number of events observed in the interval x_j to $x_j + dx_j$,

$\frac{d\sigma}{dx_i}$ = differential cross section for process in question ,

$\frac{d\theta}{dx_j}(x_i, x_j)$ = differential probability for various apparatus effects not related to geometry. It is the probability for a particle to be produced with parameters x_i and be observed with parameters x_j to $x_j + dx_j$. x_i and x_j constitute a complete description of an event.

$A(x_i, x_j) = 1$ if event is observed ,
 $= 0$ if event is not observed ,

n = normalization factor (i.e., flux) .

Then

$$\frac{dN}{dx_j} = n \int \frac{d\sigma}{dx_i} \frac{d\theta}{dx_j}(x_i, x_j) \cdot A(x_i, x_j) \cdot dx_i ,$$

where the integral is over the production variables to take into account the various uninteresting apparatus effects (i.e., multiple scattering, axial symmetry, resolution effects, etc.). If there are no apparatus effects, then $\frac{d\theta}{dx_j} = \delta(x_i - x_j)$.

$$\frac{dN}{dx_j} = n A(x_j) \frac{d\sigma}{dx_j} ,$$

where the last equality defines the acceptance $A(x_j)$ ($0 < A(x_j) < 1$) and n is a flux factor.

$A(x_j)$ is the probability that an event will be observed at x_j if we integrate over the x_i . In general, the integration to obtain $A(x_j)$ is difficult if not impossible to do analytically. A Monte Carlo technique is used.

$n \frac{d\sigma}{dx_i}$ particles are thrown in the phase space x_i and we ask how many are accepted: dN/dx_j . The acceptance is then the ratio of accepted to thrown.

The models used throughout in this experiment have been various J/ψ production models. As in most models, we assume that the invariant cross section factorizes into a p_t and x or y distribution. An event is thrown with p_t and x or y and is weighted according to the cross section. The J/ψ is then allowed to decay. Various models of the production and decay of the J/ψ have been looked at: the helicity and the Gottfried-Jackson frame with flat and $1 + \cos^2\theta$ distributions.

The decay products are then traced through the apparatus. The target interaction point is thrown to allow the interaction to be anywhere along the 4 in. target. Bremsstrahlung loss of the decay electrons in the target is included. About 10% of the J/ψ is irrecoverably lost due to this. The apparent mass is shifted well below 3.1 GeV so that the event would not be recognized as a J/ψ . The particles are then bent into the

detector apparatus. At the 80 ft station, we include an effective multiple scattering as the lepton passes through the detector.

If the lepton pair is still in the apparatus as far as the lead glass, we then reconstruct the event exactly as we would with real data. The resolution of the hodoscopes and wire chambers is included in a constrained fit of the track. The track is then traced back through the bending magnet with the constraint that the track pass through the center of the target. Various quantities are calculated for the tracks: momentum, mass, p_t , y , x , etc.

Fiducial cuts are then applied to each track. If the event passes, it is histogrammed as a function of p_t , y weighted by $d\sigma/dp_t dy$. The ratio of the accepted histogram and the thrown histogram gives the acceptance as a function of p_t and y .

For the mass acceptance, we throw J/ψ with various masses and integrate over p_t . The distribution of thrown events is given by

$$n \frac{d^2\sigma}{dm dy} .$$

The accepted events by

$$\frac{d^2N}{dm dy} .$$

The acceptance is then given by

$$A(m, y) = \frac{d^2N/dm dy}{n d^2\sigma/dm dy} .$$

APPENDIX X

Accidental Background Determination

This appendix will describe how we have determined the accidental background in our data. We first define what we mean by accidentals. An accidental event occurs when two protons in the same time resolution bin of the apparatus (in our experiment this is determined by the rf structure of the accelerator: 18.9 ns) interact. One interaction sends a particle into one arm and the other into the other arm of the spectrometer. Our background arises when these two uncorrelated particles are identified as electrons. There is no way to distinguish this from two particles from the same interacting proton on an event by event basis. We must resort to determining the background integrated over the entire data set.

The shape of the accidental background is obtained from pairing uncorrelated single arm events (i.e., events which trigger one arm of the spectrometer). This "pair" event is required to pass the exact same cuts that the normal pair data must pass. The number of events gotten this way goes as the number of single arm events squared so statistics are not a problem. This spectrum must now be normalized.

Let n_U, n_D = counting rate of counters U and D in time interval T. U and D are uncorrelated.

t = time resolution.

Then $n_i t/T$ = probability of i counting in time interval T_0 to T_0+t .

$$\begin{aligned}
 n_{UD} &= \text{coincidence rate of counters U and D} \\
 &= n_U t/T \cdot n_D t/T \cdot T/t \\
 &\quad \text{if uniform counting rate throughout time interval T} \\
 &\quad T/t \text{ is the number of period t.}
 \end{aligned}$$

If the counting rate is not uniform (dn/dt not a constant), the effective counting time T' is given by

$$T' = n_U n_D t / n_{UD} \cdot$$

Define duty factor

$$D = T'/T.$$

The electron accidental pair rate is then given by

$$\begin{aligned}
 e_{UD} &= e_U e_D t / T' \\
 &= t/T \cdot e_U e_D / D
 \end{aligned}$$

for time interval T (i.e., beam pulse). The single arm electron yield e_i was calibrated per NDNBY (= N) which is a measure of the number of interacting protons. The duty factor D was calculated from the coincidence T_U, T_D, T_{UD} . T_{UD} was mostly accidental since there were a great number of uncorrelated hadrons going through the spectrometer. The rate constants found are given in Table XVII. e_{UD} was summed pulse by pulse for the data set presented

$$E_{UD} = \Sigma e_{UD} \cdot$$

The spectrum of pair events is then normalized to E_{UD} events. The number of events is given in Table XVII. We note that most of the events will be in the low mass region of the spectrometer. This normalized spectrum is then corrected

for acceptance and flux just as the normal pair data. As explained in Appendix IX, the model used is the J/ψ production model.

The differential cross sections for the two energies are given in Figs. 25-26, where the smooth curve is the accidental spectrum. The figures show that at the J/ψ and ψ' region, except for the resonances, everything is dominated by accidentals. Table XI gives the number of accidental events expected in the J/ψ and ψ' region.

We note that the accidentals go up with current. This is due to our running at higher intensity for the higher currents. The accidentals go as the square of the intensity but it is dominated by the low mass region. Except for 1100 A, the accidental background is very low. If we assume everything away from the J/ψ and ψ' is accidental, we get a second normalization of the accidental spectrum. The results of this are shown in Table XI.

REFERENCES

- 1 J.A. Appel, M.H. Bourquin, I. Gaines, D.C. Hom, L.M. Lederman, H.P. Paar, J.-P. Repellin, D.H. Saxon, H.D. Snyder, J.M. Weiss, J.K. Yoh, B.C. Brown, J.-M. Gaillard, T. Yamanouchi, Phys. Rev. Lett. 33, 719 (1974); 33, 722 (1974).
J.A. Appel, M.H. Bourquin, I. Gaines, D.C. Hom, L.M. Lederman, H.P. Paar, J.-P. Repellin, H.D. Snyder, J.M. Weiss, J.K. Yoh, B.C. Brown, C.N. Brown, J.-M. Gaillard, J.R. Sauer, T. Yamanouchi, Phys. Rev. Lett. 35, 9 (1975).
H. P. Paar, Nevis Report 208, Columbia University Ph.D. Thesis (1975).
I. Gaines, Nevis Report 215, Columbia University Ph.D. Thesis (1976).
- 2 M. Breidenbach, J.I. Friedman, H.W. Kendall, E.D. Bloom, D.H. Coward, H. DeStaebler, J. Drees, L.W. Mo, R.E. Taylor, Phys. Rev. Lett. 23, 935 (1969).
- 3 A. Litke, G. Hanson, A. Hofmann, J. Koch, L. Law, M.E. Law, J. Leong, R. Little, R. Madaras, H. Newman, J.M. Paterson, R. Pordes, K. Strauch, G. Tarnopolsky, Richard Wilson, Phys. Rev. Lett. 30, 1189 (1973).
G. Tarnopolsky, J. Eshelman, M.E. Law, J. Leong, H. Newman, R. Little, K. Strauch, R. Wilson, Phys. Rev. Lett. 32, 432 (1974).
B. Richter, London International Conference on High Energy Physics (1974).
- 4 J.D. Bjorken, Phys. Rev. 179, 1547 (1969).
J.D. Bjorken, E.A. Paschos, Phys. Rev. 185, 1975 (1969).
- 5 S.D. Drell, T.-M. Yan, Phys. Rev. Lett. 25, 316 (1970).
- 6 L.M. Sehgal, Phenomenology of Neutrino Reactions, Argonne National Laboratory, ANL-HEP-PR-75-45.
D.H. Perkins, SLAC Conference on Leptons and Photons at High Energies (1975).
- 7 H.P. Paar, E.A. Paschos, Phys. Rev. D10, 1502 (1974).
S. Pakvasa, D. Parashar, S.F. Tuan, Phys. Rev. D10, 2124 (1974).
- 8 S.M. Berman, J.D. Bjorken, J.B. Kogut, Phys. Rev. D4, 3388 (1971).
J. Kuti, V.F. Weisskopf, Phys. Rev. D4, 3418 (1971).
Also, see Ref. 4.
- 9 M. Gell-Mann, Phys. Lett. 8, 214 (1964).
G. Zweig, CERN Repts. TH 401, TH 402 (1964).

- 10 R.E. Taylor, SLAC Conference (1974).
L.W. Mo, Proceedings of the Division of Particles and
Fields, APS Annual Meeting 1976, BNL-50598.
Gargamelle Neutrino Collaboration (Ref. 20), Nucl. Phys.
B85, 269 (1975).
- 11 M. Duong-van, Phys. Lett. 60B, 287 (1976);
see also Ref. 7.
- 12 E. Fermi, Z. fur Phys. 88, 161 (1934).
- 13 R.P. Feynman, M. Gell-Mann, Phys. Rev. 109, 193 (1958).
- 14 H. Yukawa, Proc. Math. Soc. Japan 17, 48 (1935).
- 15 Y. Yamaguchi, Il Nuovo Cimento 43, 193 (1966).
F. Chilton, A.M. Saperstein, E. Shrauner, Phys. Rev.
148, 1380 (1966).
- 16 L.M. Lederman, B.G. Pope, Phys. Rev. Lett. 27, 765 (1971).
L.M. Lederman, D.H. Saxon, Nucl. Phys. B63, 313 (1973).
- 17 T.D. Lee, G.C. Wick, Phys. Rev. D2, 1033 (1970).
- 18 S. Weinberg, Phys. Rev. Lett. 19, 1264 (1967);
27, 1688 (1971).
- 19 H. Georgi, S.L. Glashow, Phys. Rev. Lett. 28, 1494 (1972).
- 20 F.J. Hasert, S. Kabe, W. Krenz, J. Von Krough, D. Lanske,
J. Morfin, K. Schultze, H. Weerts, G.H. Bertrand-Coremans,
J. Sacton, W. Van Doninck, P. Vilain, U. Camerini, D.C.
Cundy, R. Baldi, I. Danilchenko, W.F. Fry, D. Haidt,
S. Natali, P. Musset, B. Osculati, R. Palmer, J.B.M.
Pattison, D.H. Perkins, A. Pullia, A. Rousset, W. Venus,
H. Wachsmuth, V. Brisson, B. Degrange, M. Haguenaer,
L. Kluberg, U. Nguyen-Khac, P. Petiau, E. Belotti,
S. Bonetti, D. Cavalli, C. Conta, E. Fiorini, M. Rollier,
B. Aubert, D. Blum, L.M. Chounet, P. Heusse, A. Lagarrigue,
A.M. Lutz, A. Orkin-Lecourtois, J.P. Vialle, F.W. Bullock,
M.J. Esten, T.W. Jones, J. McKenzie, A.G. Michette,
G. Myatt, W.G. Scott, Phys. Lett. 46B, 138 (1973).
- 21 M.L. Perl, G.S. Abrams, A.M. Boyarski, M. Breidenbach,
D.D. Briggs, F. Bulos, W. Chinowsky, J.T. Dakin, G.J.
Feldman, C.E. Friedberg, D. Fryberger, G. Goldhaber, G.
Hanson, F.B. Heile, B. Jean-Marie, J.A. Kadyk, R.R. Larsen,
A.M. Litke, D. Luke, B.A. Lulu, V. Luth, D. Lyon, C.C.
Morehouse, J.M. Paterson, F.M. Pierre, T.P. Pun, P.A.
Rapidis, B. Richter, B. Sadoulet, R.F. Schwitters, W.
Tanenbaum, G.H. Trilling, F. Vannucci, J.S. Whitaker,
F.C. Winkelman, J.E. Wiss, Phys. Rev. Lett. 35, 1489 (1975).

- 22 B.W. Lee, Phys. Rev. D6, 1188 (1972).
J. Prentki, B. Zumino, Nucl. Phys. B47, 99 (1972).
- 23 B.J. Bjorken, S.L. Glashow, Phys. Lett. 11, 255 (1964).
- 24 S.L. Glashow, J. Iliopoulos, L. Maiani, Phys. Rev. D2,
1285 (1970).
- 25 J.J. Aubert, U. Becker, P.J. Biggs, J. Burger, M. Chen,
G. Everhart, P. Goldhagen, J. Leong, T. McCorriston,
T.G. Rhoades, M. Rhode, Samuel C.C. Ting, Sau Lan Wu,
Y.Y. Lee, Phys. Rev. Lett. 33, 1404 (1974).
J.E. Augustin, A.M. Boyarski, M. Breidenbach, F. Bulos,
J.T. Dakin, G.J. Feldman, G.E. Fischer, D. Fryberger,
G. Hanson, B. Jean-Marie, R.R. Larsen, V. Luth, H.L.
Lynch, D. Lyon, C.C. Morehouse, J.M. Paterson, M.L. Perl,
B. Richter, P. Rapidis, R.F. Schwitters, W.M. Tanenbaum,
F. Vannucci, G.S. Abrams, D. Briggs, W. Chinowsky, C.E.
Friedberg, G. Goldhaber, R.J. Hollebeek, J.A. Kadyk, B.
Lulu, F. Pierre, G.H. Trilling, J.S. Whitaker, J. Wiss,
J.E. Zipse, Phys. Rev. Lett. 33, 1406 (1974).
- 26 G.S. Abrams, D. Briggs, W. Chinowsky, C.E. Friedberg,
G. Goldhaber, R.J. Hollebeek, J.A. Kadyk, A. Litke,
B. Lulu, F. Pierre, B. Sadoulet, G.H. Trilling, J.S.
Whitaker, J. Wiss, J.E. Zipse, J.E. Augustin, A.M.
Boyarski, M. Breidenbach, F. Bulos, G.J. Feldman, G.E.
Fischer, D. Fryberger, G. Hanson, B. Jean-Marie, R.R.
Larsen, V. Luth, H.L. Lynch, D. Lyon, C.C. Morehouse,
J.M. Paterson, M.L. Perl, B. Richter, P. Rapidis, R.F.
Schwitters, W. Tanenbaum, F. Vannucci, Phys. Rev. Lett. 33,
1453 (1974).
Recent reviews on electron-positron annihilation are
B.H. Wiik and G. Wolf, Electron-Positron Interactions,
DESY 77/01, January 1977.
Vera Luth, Hadron Production in e^+e^- Annihilation,
SLAC-PUB-1873, January 1977.
- 27 B. Knapp, W. Lee, P. Leung, S.D. Smith, A. Wijangco,
J. Knauer, D. Yount, J. Bronstein, R. Coleman, G. Gladding,
M. Goodman, M. Gormley, R. Messner, T. O'Halloran, J.
Sarracino, A. Wattenberg, M. Binkley, I. Gaines, J. Peoples,
Phys. Rev. Lett. 37, 882 (1976).
- 28 J.P. Boymond, R. Mermod, P.A. Piroue, R.L. Sumner,
J.W. Cronin, H.J. Frisch, M.J. Shochet, Phys. Rev.
Lett. 33, 112 (1974); also see Ref. 1.

- 29 H.D. Snyder, D.C. Hom, L.M. Lederman, H.P. Paar, J.M. Weiss, J.K. Yoh, J.A. Appel, B.C. Brown, C.N. Brown, W.R. Innes, T. Yamanouchi, D.M. Kaplan, Phys. Rev. Lett. 36, 1415 (1976).
B.C. Brown, J.A. Appel, C.N. Brown, W. Innes, T. Yamanouchi, R.J. Engelmann, R.J. Fisk, H. Jostlein, D.M. Kaplan, R.D. Kephart, R.L. McCarthy, D.C. Hom, L.M. Lederman, H.P. Paar, H.D. Snyder, J.M. Weiss, J.K. Yoh, FERMILAB - 77/54-EXP.
- 30 D.C. Hom, L.M. Lederman, H.P. Paar, H.D. Snyder, J.M. Weiss, J.K. Yoh, J.A. Appel, B.C. Brown, C.N. Brown, W.R. Innes, T. Yamanouchi, D.M. Kaplan, Phys. Rev. Lett. 36, 1236 (1976).
H.D. Snyder, Nevis Report, Columbia University Ph.D. Thesis.
- 31 D.C. Hom, L.M. Lederman, H.P. Paar, H.D. Snyder, J.M. Weiss, J.K. Yoh, J.A. Appel, B.C. Brown, C.N. Brown, W.R. Innes, T. Yamanouchi, R.J. Engelmann, R.J. Fisk, H. Jostlein, D.M. Kaplan, R.D. Kephart, R.L. McCarthy, Phys. Rev. Lett. 37, 1374 (1976). A followup on the muon experiment with better resolution and larger acceptance is scheduled to begin in May 1977.
- 32 J.A. Appel, M.H. Bourquin, I. Gaines, D.C. Hom, L.M. Lederman, H.P. Paar, J.P. Repellin, D.H. Saxon, H.D. Snyder, J.M. Weiss, J.K. Yoh, B.C. Brown, C.N. Brown, J.M. Gaillard, J.R. Sauer, T. Yamanouchi, Nucl. Instr. and Meth. 127, 495 (1975).
- 33 H. Cunitz, W. Sippach, J. Dieperink, Nucl. Instr. and Meth. 91, 211 (1971).
- 34 K. Gottfried, J.D. Jackson, Phys. Lett. 8, 144 (1964).
- 35 U. Becker, private communication, as quoted in Anderson et al at the Tbilisi Conference.
Yu.M. Antipov, V.A. Bessubov, N.P. Budanov, Yu.B. Bushnin, S.P. Denisov, Yu.P. Gorin, A.A. Lebedev, A.A. Lednev, Yu.M. Mikhailov, A.I. Petrukhin, S.A. Polovnikov, V.N. Roinishvili, V.S. Selesnev, V.I. Sergienko, D.A. Stoyankva, A.N. Sytin, Ya.A. Vazdik, F.A. Yotch, Phys. Lett. 60B, 309 (1976).
K.J. Anderson, G.G. Henry, K.T. McDonald, C. Newman, J.E. Pilcher, E.I. Rosenberg, J.G. Branson, G.E. Hogan, R.D. Pisarski, G.H. Sanders, A.J.S. Smith, J.J. Thaler, XVIIIth Conference on High Energy Physics, Tibilisi, USSR (1976).
M. Binkley, I. Gaines, J. Peoples, B. Knapp, W. Lee, P. Leung, S.D. Smith, A. Wijangco, J. Knauer, J. Bronstein, R. Coleman, G. Gladding, M. Goodman, M. Gormley, R. Messner, T. O'Halloran, J. Sarracino, A. Wattenberg, Phys. Rev. Lett. 37, 574 (1976).
F.W. Busser, L. Camilleri, L. DiLella, B.G. Pope, A.M. Smith, B.J. Blumenfeld, S.N. White, A.F. Rothenberg, S.L.

- Segler, M.J. Tannenbaum, M. Banner, J.B. Cheze, H. Kasha, J.P. Pansart, G. Smadja, J. Teiger, H. Zaccone, A. Zylberstejn, CERN preprint, to be published.
- 36 M.B. Green, M. Jacob, P.V. Landshoff, *Il Nuovo Cimento* 29A, 123 (1975).
- 37 S.D. Ellis, M.B. Einhorn, C. Quigg, *Phys. Rev. Lett.* 36, 1263 (1976).
- 38 C.E. Carlson, R. Suaya, William and Mary Preprint, WM-PP-12 (1976); also private communication.
- 39 M.H. Bourquin, J.M. Gaillard, *Phys. Lett.* 59B, 191 (1975).
M.H. Bourquin, J.M. Gaillard, *Nucl. Phys.B*, to be published.
- 40 A. Donnachie, P.V. Landshoff, TH 2166-CERN (1976).
- 41 J.F. Gunion, Univ. of Calif. at David Preprint, UCD-76-8.
- 42 J.B. Kogut, Cornell Univ. Preprint CLNS-348, October 1976.
- 43 M. Duong-van, K.V. Vasavada, R. Blankenbecler, SLAC Preprint, submitted to Physical Review.
- 44 B. Rossi, K. Griesen, *Rev. Mod. Rev.* 13, 240 (1941).
- 45 B. Rossi, High Energy Particles (Prentice Hall), Chapter 5 (1952).
- 46 H. Messel, D. Crawford, Electron-Photon Shower Distribution Function Tables (Pergamon Press 1970).
- 47 U. Volkel, DESY 65/6 (July 1965); DESY 67/16 (May 1967).
- 48 E. Longo, I. Sestili, *Nucl. Instr. & Meth.* 128, 283 (1975).
- 49 W. Heitler, The Quantum Theory of Radiation (Oxford Press, 3rd Edition) Chapter 38 (1954).
- 50 W.B. Atwood, SLAC Report 185, Appendix B (June 1975).

Table II

Typical Trigger Rates

Run	2016		
Current	1107A		
PCSEM	4.59×10^{10}	protons/pulse	
NDN	1.06×10^5		
T_{UD}	1.54×10^5		
E_{UD}	2.09×10^3		
$E_{UD} \epsilon_{UD}$	28.1		
TGO	36.5		
TFI	3.34×10^3		
TGI	3.20×10^3		
	UP	DOWN	
T	2.70×10^6	2.52×10^6	
T_1	8.62×10^6	7.53×10^6	
E	2.52×10^5	3.65×10^5	
$E \cdot \epsilon$	5.49×10^4	5.52×10^4	
S_2	9.82×10^6		

Table III

Data Compression Efficiency

Tape	Runs	m	GG+FF	GG	FF	EF	EE
NL6971	2001-4 (raw data)	>2.2	259	227	191	172	106
		>2.8	119	113	102	98	77
		>2.9	100	96	88	87	70
NM1153	2001-4 (compressed data)	>2.2	170	154	150	145	101
		>2.8	101	100	98	96	77
		>2.9	87	87	86	85	70
NL6136	663-9 (raw data(600A))	>2.2	23				
NM1129	663-9 (compressed data)	>2.2	23				

Table IV

Fiducial Volume

Apparatus	z	Up	z	Down
Pb Glass	1433.2	y=9.3, 39.8	1434.8	y=9.3, 39.8
Chamber Y ₁	951.2	y=4.2, 19.6	950.0	y=4.3, 19.7
Magnet	502.3	x=±12.0 y=-.8, 3.4	503.6	x=±12.0 y=-.8, 3.4
2' Collimator	60.16	x=-1.40, 1.40	60.16	x=-1.50, 1.30
2" Collimator	266.01	y=-1.20, 0.88	266.01	y=-1.04, 1.04
Target	0.00	x=-2.2, 4.6	0.00	x=-3.0, 4.2
Production Angles		$\theta_x = -.024, .022$ $\theta_y = -.0045, .0037$		$\theta_x = -.024, .022$ $\theta_y = -.0044, .0040$

NOTE

Coordinate system used has z along 72.5 mrad. spectrometer axis. y is in vertical bending direction. x points in the horizontal plane towards large angles. All lengths are in units of inches.

Table V

Event Track Multiplicity for 400 GeV Data

	m (GeV)	Number Events	Extra Tracks	Extra Electrons
600A	all	193	5	5
	ψ	92	3	3
	>5	2	0	0
800A	all	440	1	1
	ψ	253	0	0
	>5	1	0	0
960A	all	79	1	0
	ψ	47	1	0
	>5	1	0	0
1100A	all	345	2	2
	ψ	184	2	2
	>5	18	0	0
1300A	all	65	1	1
	ψ	15	0	0
	>5	16	0	0

NOTE

Multiple tracks which are identical to 100 MeV momentum and 1 mrad. opening angle are considered one track.

Table VI

 ψ/ψ' Resolution

	m (GeV)	σ_{expt} (GeV)	σ_{MC} (GeV)
600A	3.091 \pm .005	.043 \pm .003	.042
800A	3.105 \pm .003	.038 \pm .002	.029
1100A	3.114 \pm .003	.036 \pm .002	.026
1100A	3.695 \pm .006	.040 \pm .004	.031

Table VII

 χ^2 Fit to $A(1+\alpha \cos^2\theta)$ to 400 GeV ψ Model: flat helicity, invariant cross section $\propto e^{-1.2p_t}$

	α	χ^2	CL
600A	0	1.15	.90
	+1	1.58	.80
	$.33 \pm .48$.479	.93
800A	0	15.5	.005
	+1	4.87	.34
	$.93 \pm .40$	4.84	.20

Model: $1+\cos^2\theta$, invariant cross section $\propto e^{-1.5p_t}$

600A	0	2.68	.60
	+1	.654	.95
	$.68 \pm .61$.432	.93
800A	0	31.5	<.001
	+1	7.47	.12
	$1.8 \pm .6$	4.71	.20

Model: flat helicity, invariant cross section $\propto e^{-1.2p_t}$

600+800A	0	14.3	.006
	+1	4.32	.37
	$.75 \pm .31$	3.77	.30

Model: $1+\cos^2\theta$, invariant cross section $\propto e^{-1.5p_t}$

600+800A	0	30.3	<.001
	+1	5.14	.28
	$1.5 \pm .2$	3.67	.30

Model: $1+\cos^2\theta$ Gottfried-Jackson, $e^{-1.5p_t}$

600+800A	+1	35.9	<.001
----------	----	------	-------

Table VIII

 ψ/ψ' Cross Sections

400 GeV	600A	800A	960A	1100A
NDNSGY	57.6	345	148.6	2300×10^6
NDN/PCSEM	275	275	275	300×10^{-8}
$\psi e^{-1.5p_t}, 1+\cos^2\theta$ helicity				
Acceptance	2.04	1.40	.565	$.135 \times 10^{-4}$
Yield (Y)	91-10	249-40	41-4	171-20
$B \frac{d\sigma}{dy}(y=0)$	10.9	6.69×10^{-33}		
$\langle B \frac{d\sigma}{dy} \rangle =$	$(8.80 \pm 2.20) \times 10^{-33} \text{ cm}^2/\text{nucleon}$			
$\psi' e^{-1.9p_t}$				
Acceptance		3.10	2.29	1.28×10^{-4}
Yield	1	12-6	7-2	41-8
$R = B'\sigma'/B\sigma$		1.3 ± 0.7	3.3 ± 1.6	$2.3 \pm 0.8\%$
$\langle R \rangle =$	$.018 \pm .006$			
300 GeV				
NDNSGY	43.2	230		1820×10^6
NDN/PCSEM		275		300×10^{-8}
$\psi e^{-1.6p_t}$				
Acceptance	1.93	1.22		$.0973 \times 10^{-4}$
Yield	45-11	139-20		122-30
$B \frac{d\sigma}{dy}$	6.35	6.60×10^{-33}		
$\langle B \frac{d\sigma}{dy} \rangle =$	$(6.48 \pm 1.62) \times 10^{-33} \text{ cm}^2/\text{nucleon}$			
$\psi' e^{-1.9p_t}$				
Acceptance		2.78		1.07×10^{-4}
Yield	0	11-6		20-6
$B'\sigma'/B\sigma$		1.8 ± 0.9		$1.4 \pm 0.5\%$
$\langle R \rangle =$	$.014 \pm .005$			

Table IX

Differential Cross Sections

For the model of $1+\cos^2\theta$ and $E\frac{d^3\sigma}{dp^3}=Ae^{-bp_t}$

	$B\frac{d\sigma}{dy}$ (cm ² /nucleon)	A	b	P(χ^2)
400 GeV ψ	$(8.80\pm 2.20)\times 10^{-33}$	$(3.32\pm 1.03)\times 10^{-33}$	$1.54\pm .14$.06
ψ'	$(1.67\pm 0.61)\times 10^{-34}$	$(9.59\pm 6.14)\times 10^{-35}$	1.9 ± 0.5	
300 GeV ψ	$(6.48\pm 1.62)\times 10^{-33}$	$(2.81\pm 1.05)\times 10^{-33}$	$1.65\pm .23$.15
ψ'	$(9.72\pm 3.55)\times 10^{-35}$	$(5.58\pm 3.57)\times 10^{-35}$	1.9	

For the model of flat helicity

	$B\frac{d\sigma}{dy}$	A	b	P(χ^2)
400 GeV ψ	$(1.29\pm 0.32)\times 10^{-32}$	$(2.91\pm 0.93)\times 10^{-33}$	$1.19\pm .12$.0003
300 GeV ψ	$(7.22\pm 1.80)\times 10^{-33}$	$(1.44\pm 0.69)\times 10^{-33}$	$1.12\pm .23$	0.15

Table X

Trigger Counter Efficiencies

	Up	Down
T_0	98.2 ± 1.1	99.8 ± 0.8
T_1	96.3 ± 0.6	97.1 ± 0.5
S_2	98.9 ± 0.3	99.6 ± 0.2
T	93.7 ± 0.7	96.5 ± 0.6
T_2	99.8 ± 0.7	99.7 ± 0.6

NOTE

The T_0 efficiencies are in fact an upper limit as the T_1 bit efficiency cannot be taken out.

 V_1 and V_2 Efficiencies

	Up	Down
V_1	97.5 ± 0.2	97.3 ± 0.2
V_2	98.4 ± 0.1	98.7 ± 0.1

Table XI

Accidental Background Under ψ/ψ'

400 GeV

	Total Accid.	Expected Accidental		Expected Accidental		Expected
	Events	Events	ψ	ψ	ψ'	ψ'
600A	1.76×10^6	60.1	3.22×10^4	1.1	4930	.17
800A	1.50×10^6	111.5	1.00×10^5	7.43	1.62×10^4	1.20
1100A	4.61×10^5	162.2	8.65×10^4	30.4	4.49×10^4	15.8

If we now normalize away from resonance region

	Acc. Evts	Data Evts	Expected	Expected
	3.3 < m < 3.5	3.3 < m < 3.5	Acc ψ	Acc ψ'
600A	1.25×10^4	2	5	0.8
800A	4.16×10^4	6	14	2.3
1100A	7.34×10^4	15	18	9.2

Table XII

Average Dielectron E/p Versus Beam Quality

$x = \text{NDN}$ or $\text{INDUTY} \times \text{NDN}$ ($I \times N$)

\bar{x} = median value of x for 400 GeV data

- Regions:
- 1) $x < \bar{x}$
 - 2) $\bar{x} < x < \bar{x} + \sigma$
 - 3) $\bar{x} + \sigma < x < \bar{x} + 2\sigma$
 - 4) $\bar{x} + 2\sigma < x$

E/p Averages (400 GeV)

Current:	600A	800A	960A	1100A	1300A
Low NDN 1	.992	.995	.990	.999	.994
2	.994	.994	.996	1.0000	1.00000
3	.992	.994	.992	.999	1.004
4	.998	.995	1.0000	.994	1.004
Low $I \times N$ 1	.996	.994	.994	.999	.994
2	.990	.995	.996	1.0000	1.0000
3	.990	.994	.994	.997	1.008
4	.994	.995	.994	.996	1.006

Table of Median Values (400 GeV)

	NDN	σ	INDUTY	σ	$N \times I \times 10^{-4}$	σ
600A	7150	2400	1.87	.30	1.5	.64
800A	21000	6400	1.80	.30	3.5	1.6
960A	29000	8600	1.8	.33	5.7	2.0
1100A	42300	13000	1.80	.31	7.2	3.7
1300A	66000	29000	1.80	.38	14.3	8.3

Incident protons = $5.6 \times 10^5 \times \text{NDN}$

TABLE XIII

LEAD GLASS CALIBRATION CHECK WITH J/ψ

	E/p AVERAGE	STANDARD DEVIATION	NUMBER OF EVENTS	MASS	STANDARD DEVIATION	NUMBER OF EVENTS
600 AMP. 1	1.001	.038	170	3.067	.102	168
2	1.000	.035				
800 AMP. 1	.994	.037	528	3.052	.118	516
2	.994	.040				
960 AMP. 1	.996	.040	58	3.070	.118	56
2	.997	.031				
1100 AMP. 1	1.000	.035	406	3.100	.113	400
2	.996	.034				

1 AND 2 ARE INDICES FOR RESPECTIVE
SPECTROMETER ARMS

TABLE XIV

LEAD GLASS ENERGY RESOLUTION				
	16 GeV	20 GeV	30 GeV	40 GeV
FORMULA	.0400	.0374	.0333	.0308
PREDICTED	.047	.045	.041	.039
ACTUAL	.063	.055	.045	.040

(FWHM)

Table XV

Material in Secondary Beam

Material	Comment	Length	RL	%RL	z(in.)
1 Be	Tgt 4x.0088x1"	.154	35.3	.436	.154
2 He+.01Air	Target box	585.3	444x10 ³	.1318	585.5
3 Kapton	5mil window	.0127	28.7	.04425	585.5
4 Air	Between tgt box and filter	71.10	30050	.2366	656.6
5	Filter				
6 Air	Bet filter/pile	17.46	30050	.0581	674.1
7 Mylar	Pile window	.0254	28.70	.0885	674.2
8 Airx3/760	Vac in shield	295.9	761x10 ⁴	.0039	970.1
9 Airx3/760	Magnet vac	353.1	761x10 ⁴	.0046	1323
10 Mylar	Mag window	.0254	28.7	.0885	1323
11 Polyeth	He Bag face	.0127	48.0	.0265	1323
12 He	He in bag	1057	477x10 ³	.2215	2380
13 Polyeth	He bag face	.0127	48.0	.0265	2380
14 Air	Air gap to station 1	41.91	30050	.1395	2422
15 Al	Al screen	.00678	8.9	.0762	2422
16 Aclar	PWC windows	.00635	38	.0167	2422
17 Cu	HV planes	.00031	1.43	.0218	2422
18 W	Signal plane	.000016	.35	.00457	2422
19	Hodo light tight mat.	.0127	38	.0334	2422
20 Al	Al foil for	.00254	8.9	.0285	2422

hodo wrapping						
21	Scint	V1 1/8 and 1/4"	.420	42.9	.979	2422
22		T0 light	.0127	38.0	.0334	2422
tighting						
23	Al	Al for T0	.00254	8.9	.0285	2422
24	Scint	T0 1/4"	.635	42.9	1.480	2423
25	Air	Sta.1 to T0	41.91	30050	.1395	2465
26	Air	T0 to Y2	508.0	30050	1.691	2973
27		see 1Y,P,Q				
28	Air	Y2 to T1	60.96	30050	.2029	3034
29		see T0				
30	Air	T1 to Sta. 3	495.3	30050	1.648	3530

Table XVI

Shower Cut Parameterization					
Cut Label	Cuts	A_i	B_i	E/p	Efficiency
$E=E_1$	E1/E	$-.00046$	$.520$	$-.10,+.12$	$.83$
	E12/E	$-.00024$	$.920$		
	E4/E	$.00020$	$.030$		
E_2	E1/E	$-.00050$	$.590$	$\pm.07$	$.73$
	E12/E	$-.00022$	$.947$		
	E4/E	$.00019$	$.010$		
E_3	E1/E	$-.00047$	$.622$	$\pm.05$	$.62$
	E12/E	$-.00019$	$.961$		
	E4/E	$.00018$	$.0075$		
G_1	E1/E	$-.00285$	$.35$	$\pm.10$	$.95$
	E12/E	$-.00109$	$.75$		
	E4/E	$.000101$	$.05$		
G_2	as	as	$.39$	$\pm.10$	$.93$
	above	above	$.79$		
			$.06$		
G_3	as	as	$.43$	$\pm.10$	$.90$
	above	above	$.83$		
			$.05$		
G_4	as	as	$.50$	$\pm.10$	$.83$
	above	above	$.85$		
			$.04$		
F	$E_1/E=0.14+1.2/(E+10)$			$-.10,+.12$	$.92$
	$E12/E=0.88-.003E$				
	or E_1 shower			$-.15,+.18$	

Table XVII

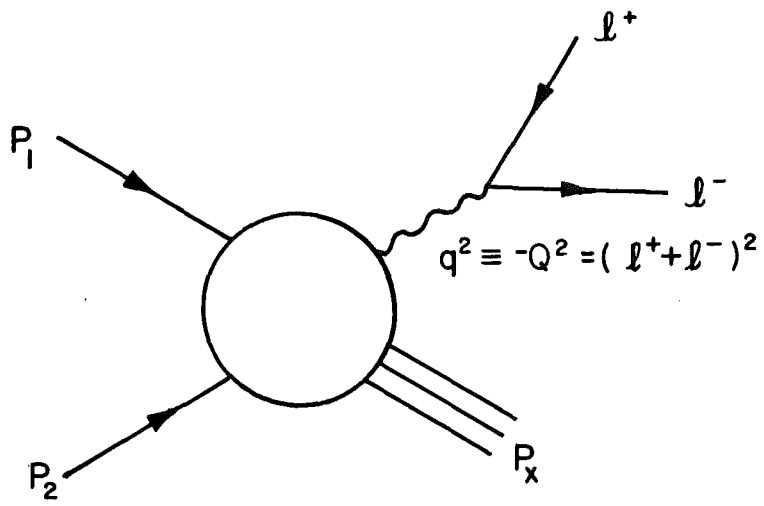
Accidental Normalization and Rate Constants

400 GeV	e_U/NDNBY	e_D/NDNBY	E_{UD}
600A	$.0584 \pm .008$	$.0555 \pm .0101$	60.1
800A	$.0206 \pm .0075$	$.0196 \pm .0074$	111.5
1100A	$.00634 \pm .00152$	$.00648 \pm .00254$	162.2
1300A	$.00104 \pm .00035$	$.00133 \pm .00038$	10.0
300 GeV			
600A	$.0886 \pm .0120$	$.0743 \pm .0043$	122.9
800A	$.0202 \pm .0035$	$.0257 \pm .0059$	94.0
1100A	$.00395 \pm .00127$	$.00553 \pm .00131$	67.7

FIGURE CAPTIONS

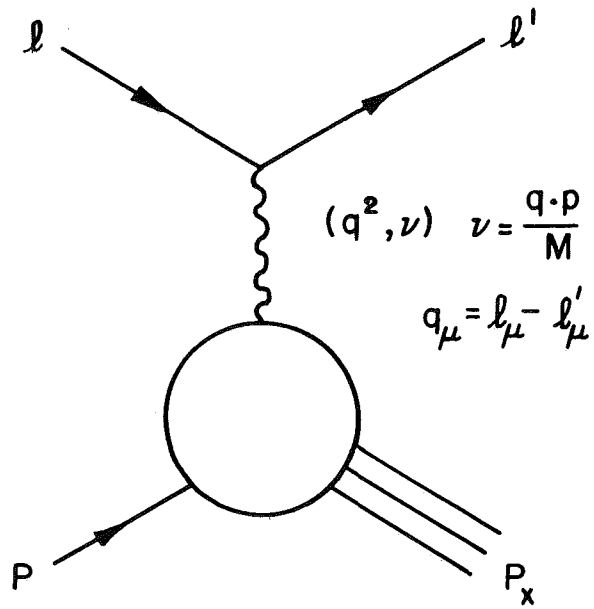
- Fig. 1 Inclusive virtual photon production in hadronic collisions
- Fig. 2 Deep inelastic lepton nucleon scattering
- Fig. 3 Hadron production in e^+e^- annihilation
- Fig. 4 Drell-Yan model for massive lepton production by parton-antiparton annihilation
- Fig. 5 Top view of double arm spectrometer
- Fig. 6 Detail layout of one arm of spectrometer
- Fig. 7 Lead glass array for one arm of spectrometer
- Fig. 8 Magnetic spectrometer and lead glass energy resolution
- Fig. 9 Fast trigger logic diagram
- Fig. 10 Block diagram of DC logic
- Fig. 11 Data plots for all spectrometer settings and 300 and 400 GeV running
- Fig. 12 Blowup of ψ/ψ' region. Muon data are shown for comparison
- Fig. 13 p_t distribution for ψ
- Fig. 14 Rapidity distribution for ψ
- Fig. 15 Decay distribution for ψ in helicity frame
- Fig. 16 Decay distribution for ψ in Gottfried-Jackson frame
- Fig. 17 ψ' data distributions
- Fig. 18 Single arm momentum resolution
- Fig. 19 400 GeV mass acceptance
- Fig. 20 300 GeV mass acceptance
- Fig. 21 ψ/ψ' p_t acceptance at 400 GeV
- Fig. 22 ψ p_t acceptance at 300 GeV
- Fig. 23 ψ center of mass rapidity acceptance
- Fig. 24 Decay angle acceptance and cross sections
- Fig. 25 Differential mass cross section at 400 GeV
- Fig. 26 Differential mass cross section at 300 GeV

- Fig. 27 Invariant ψ/ψ' cross sections and differential y cross section
- Fig. 28 T_2 pulse height distribution
- Fig. 29 ϵ bit efficiency vs. momentum
- Fig. 30 ϵ bit efficiency vs. momentum
- Fig. 31 E/p with T and $T \cdot T_2$ triggers
- Fig. 32 E/p with (a) $E \cdot \epsilon$, (b) after longitudinal shower cuts, (c) with lead absorber
- Fig. 33 Scatter plots of $\text{TOF}(\epsilon)$ vs. pulse height of ϵ
- Fig. 34 $(E/p)_{\text{up}}$ vs. $(E/p)_{\text{dn}}$ for ψ mass region when all other cuts applied
- Fig. 35 $(E/p)_{\text{up}}$ vs. $(E/p)_{\text{dn}}$ for ψ' mass region when all other cuts applied
- Fig. 36 ψ/ψ' excitation data compared to Refs. 38 and 40
- Fig. 37 ψ production by gluon amalgamation
- Fig. 38 Direct lepton production by ψ
- Fig. 39 Electromagnetic shower development
- Fig. 40 Cerenkov radiation and bremsstrahlung
- Fig. 41 Dispersion in optical media and bremsstrahlung intensity
- Fig. 42 Properties of lead glass
- Fig. 43 Lead glass pulse height transit correction
- Fig. 44 Lead glass pulse height transit correction
- Fig. 45 Lead glass (cone energy)/(layer energy) vs. radii of γ cones for 10-20 GeV electrons
- Fig. 46 Lead glass (cone energy)/(layer energy) vs radii of cones for 40-50 GeV electrons
- Fig. 47 Transverse shower development
- Fig. 48 Shower (cone energy)/(total energy) vs E/p
- Fig. 49 E/p vs. NDN
- Fig. 50 E/p vs. NDN x INDUTY
- Fig. 51 % lead glass energy outside of cone
- Fig. 52 Subtraction of hadronic showers to produce electron shower distributions



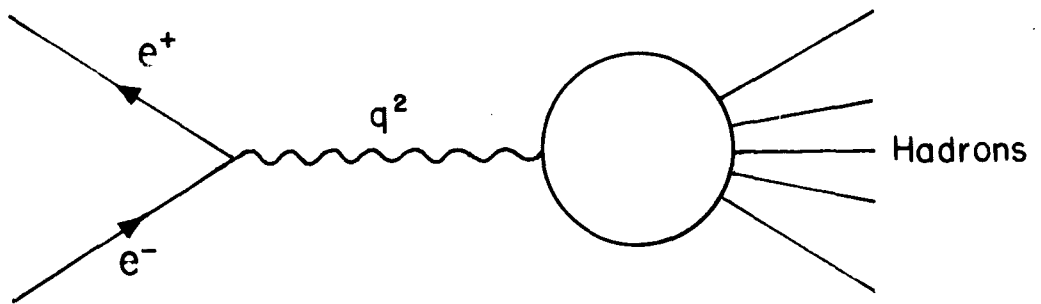
VIRTUAL PHOTON PRODUCTION

FIG. 1



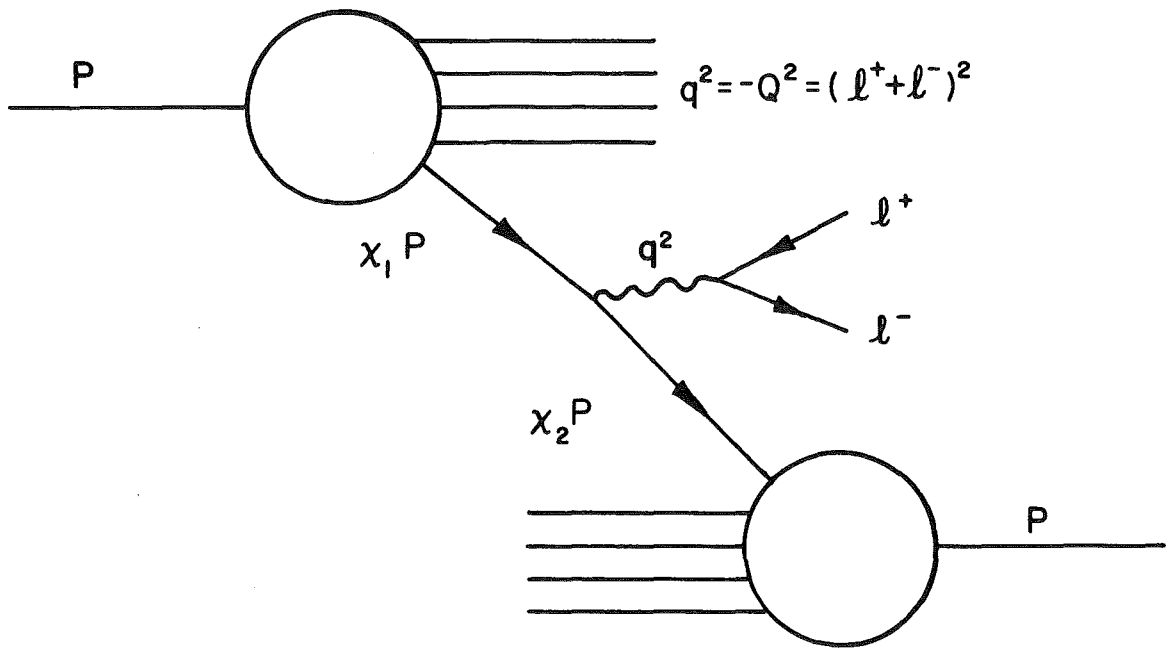
DEEP INELASTIC LEPTON
NUCLEAR SCATTERING

FIG. 2



$e^+ e^-$ PAIR ANNIHILATION

FIG. 3



PARTON ANTIPARTON ANNIHILATION

FIG. 4

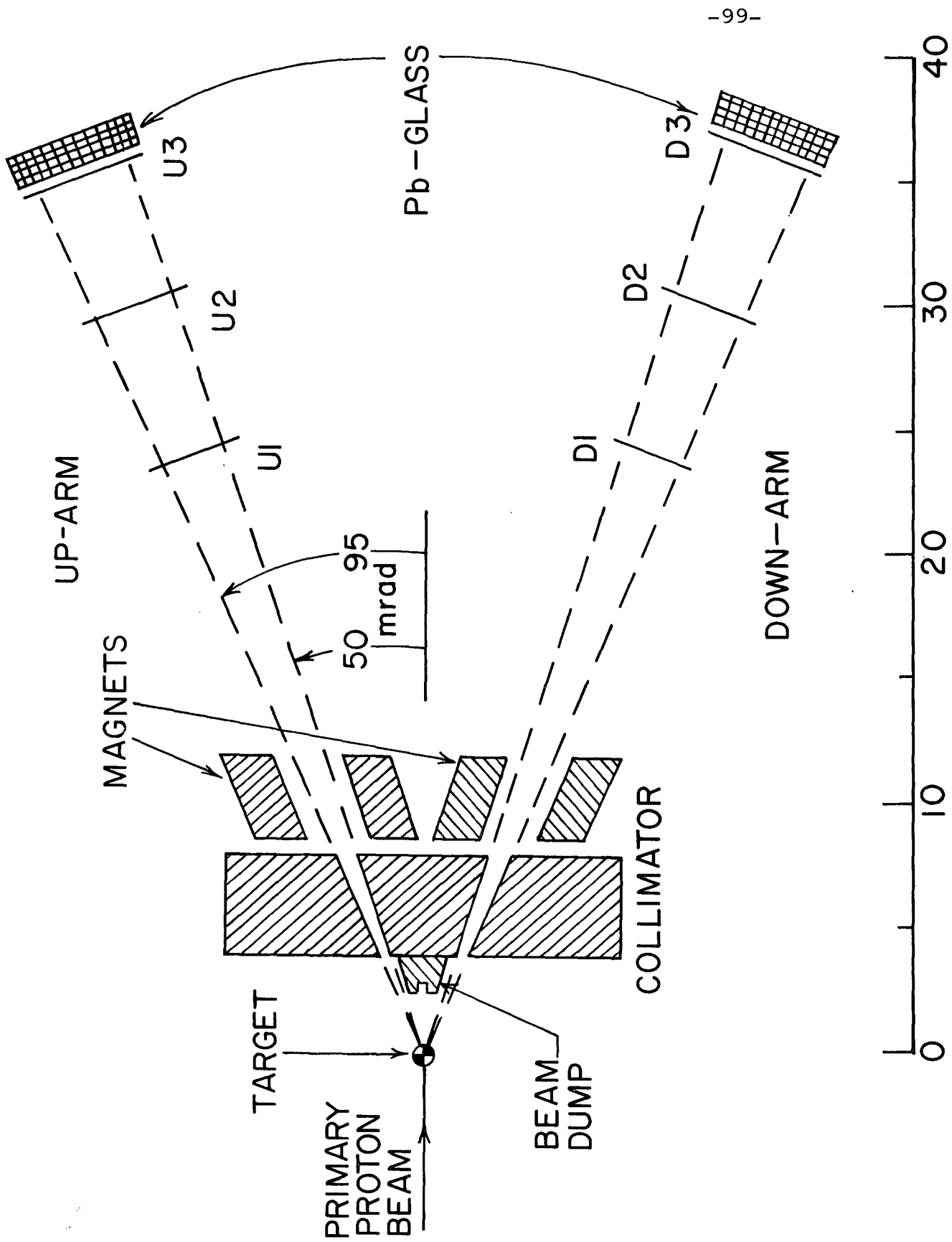
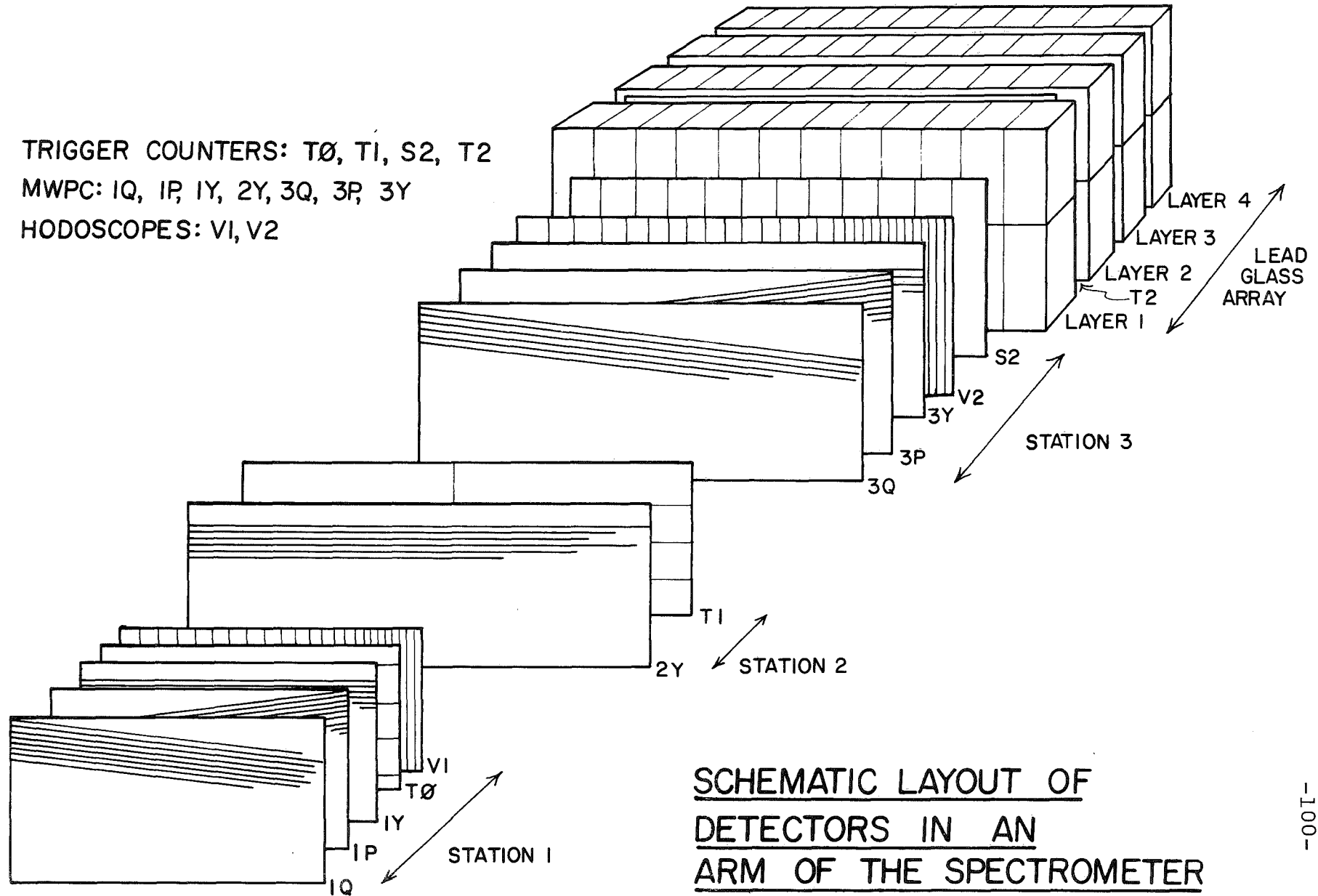


FIG. 5

TRIGGER COUNTERS: T0, T1, S2, T2
 MWPC: IQ, IP, IY, 2Y, 3Q, 3P, 3Y
 HODOSCOPES: V1, V2



SCHEMATIC LAYOUT OF
 DETECTORS IN AN
 ARM OF THE SPECTROMETER

FIG. 6

LEAD GLASS ARRAY

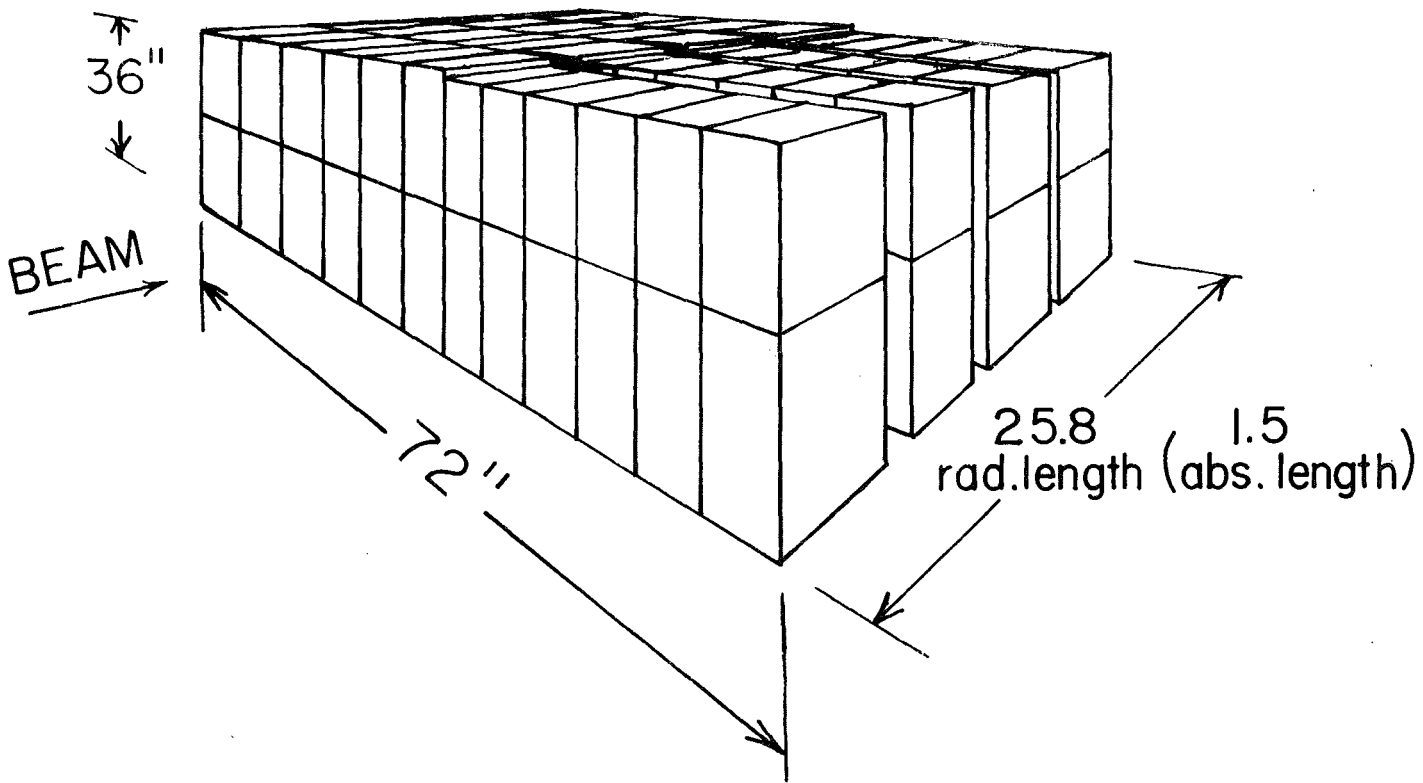


FIG. 7

RESOLUTION

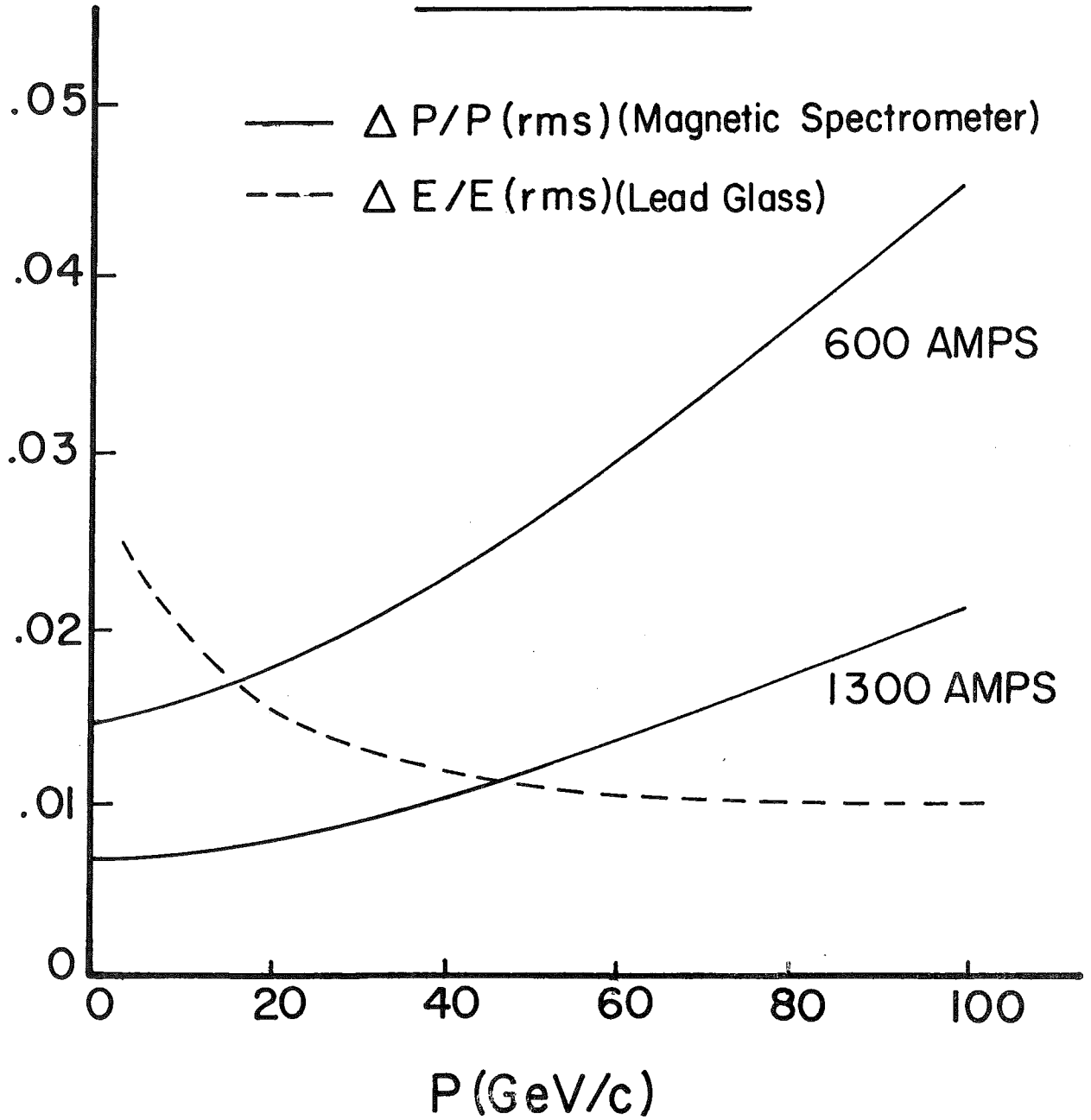


FIG. 8

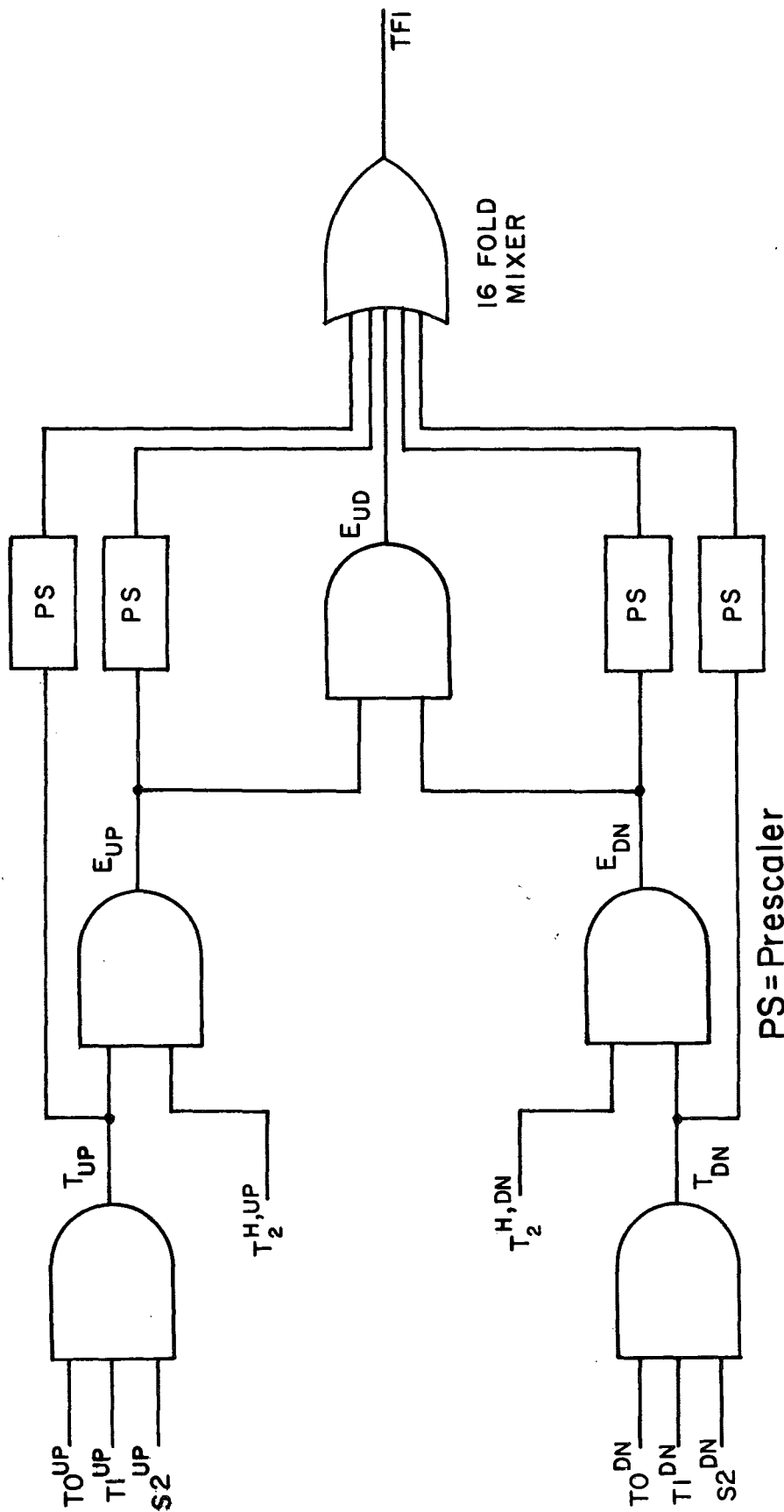


FIG. 9

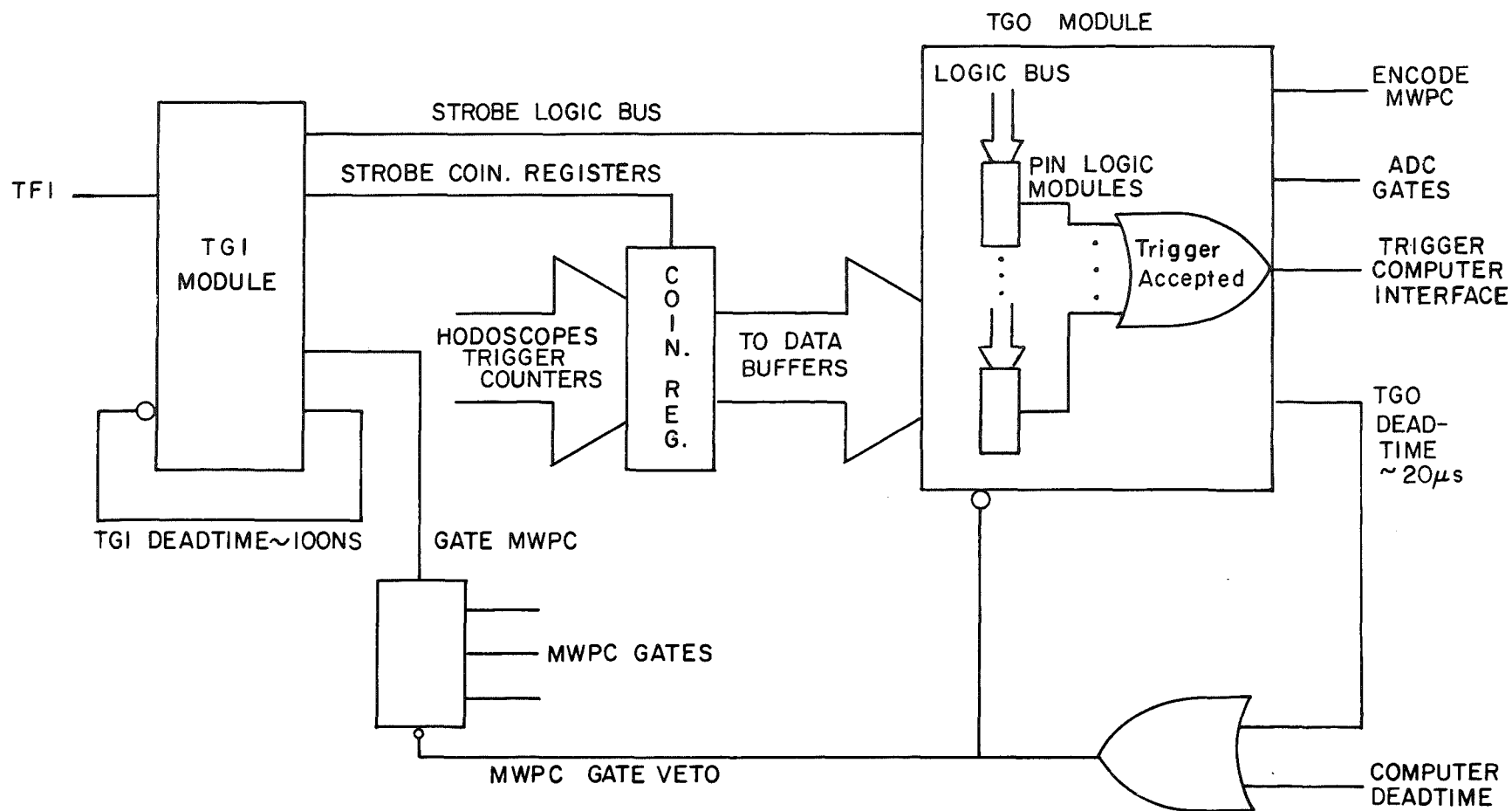


FIG. 10

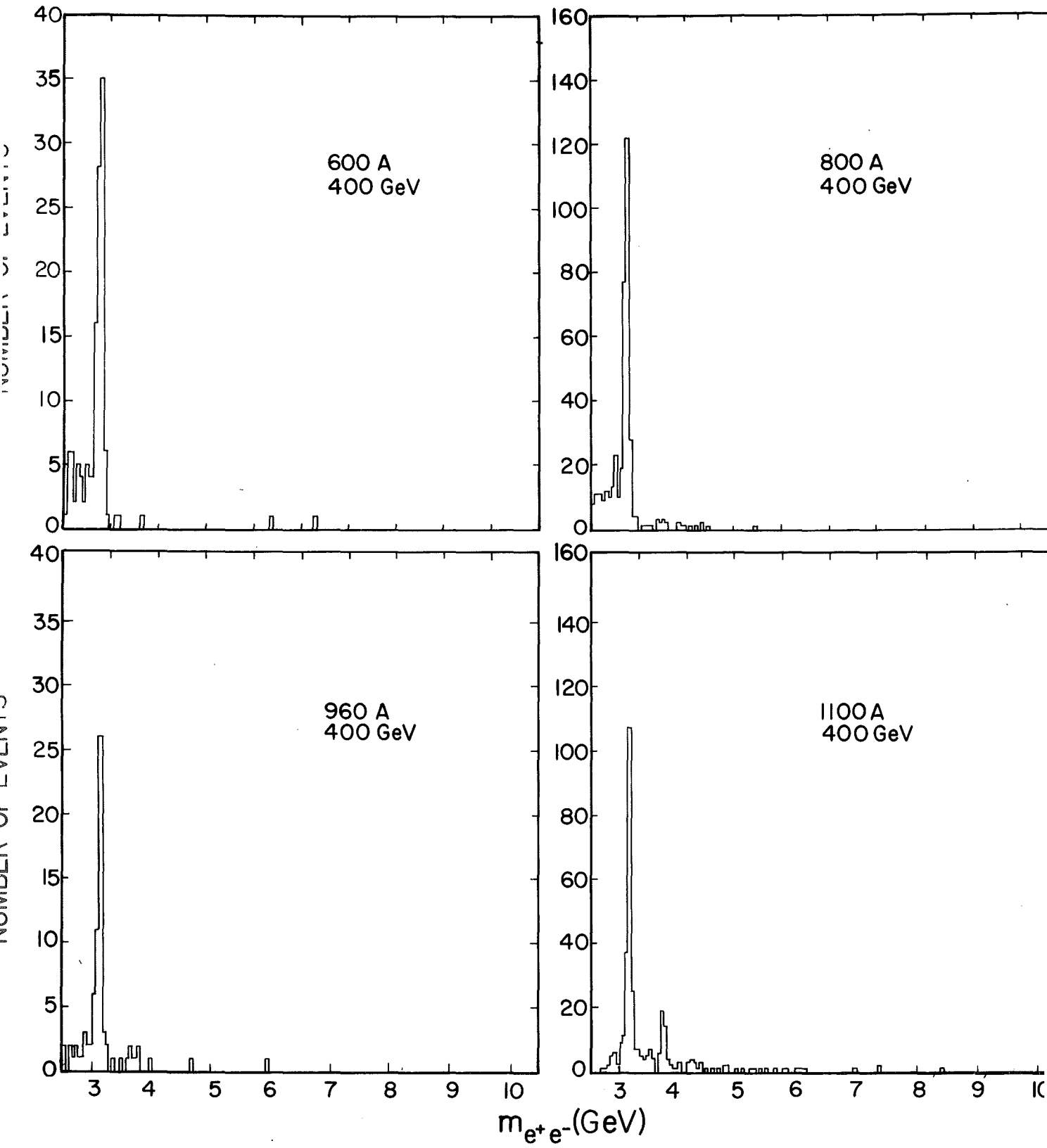


FIG. 11a

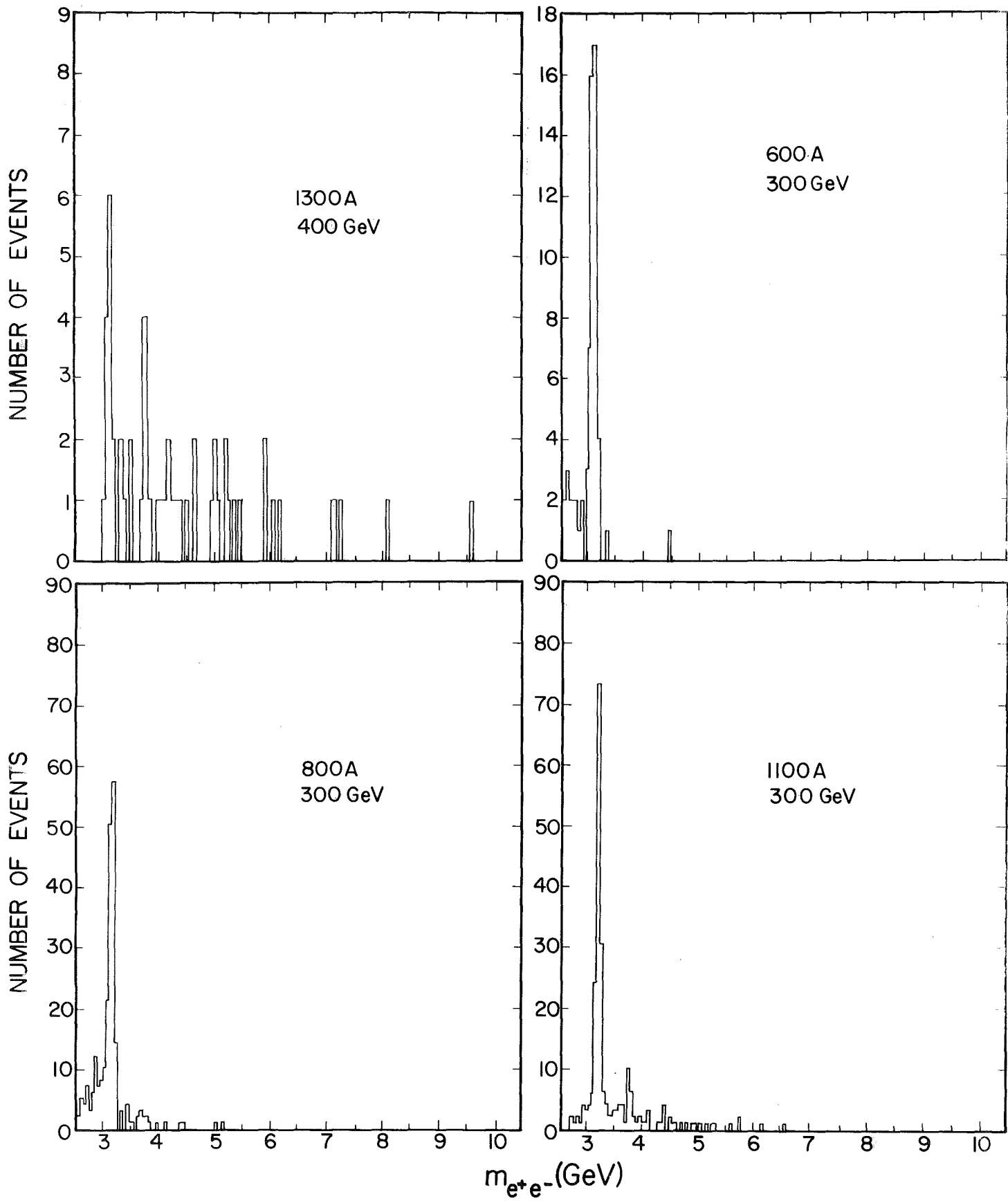


FIG. 11b

NUMBER OF EVENTS

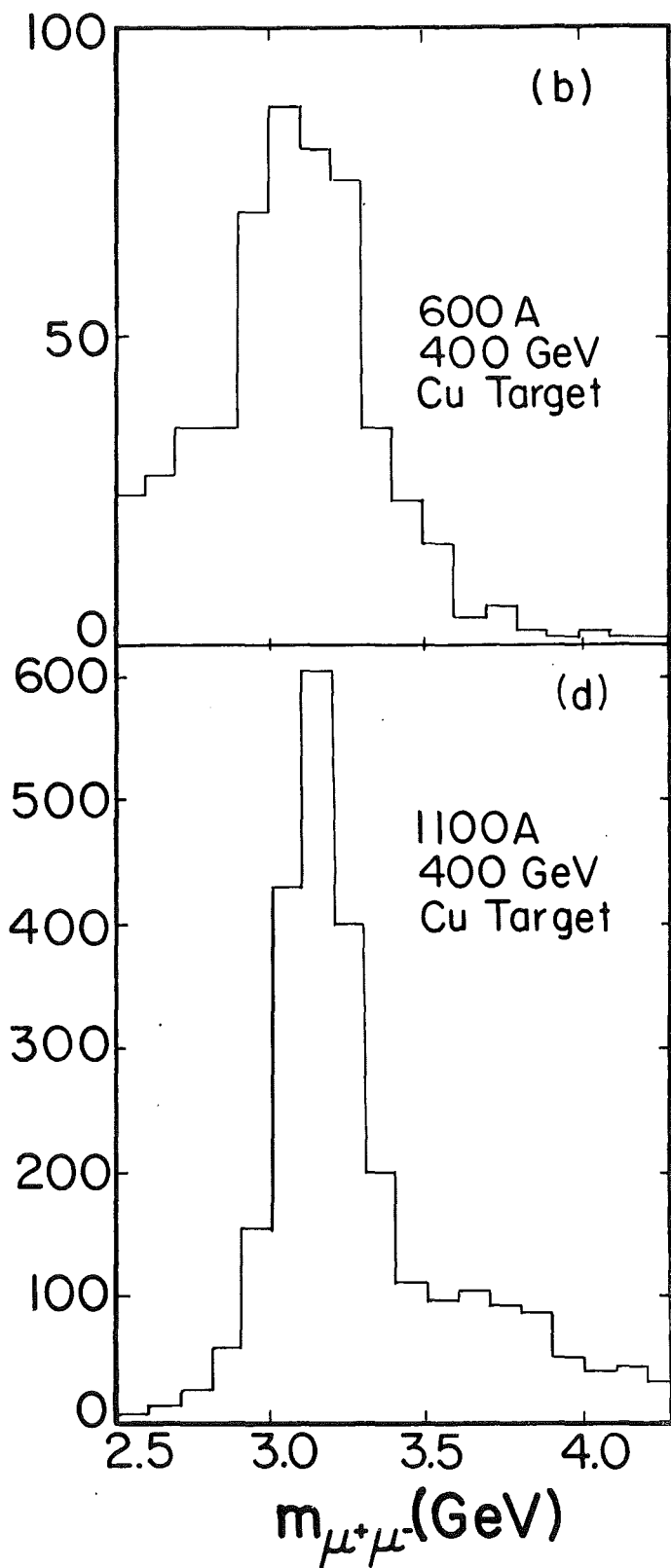
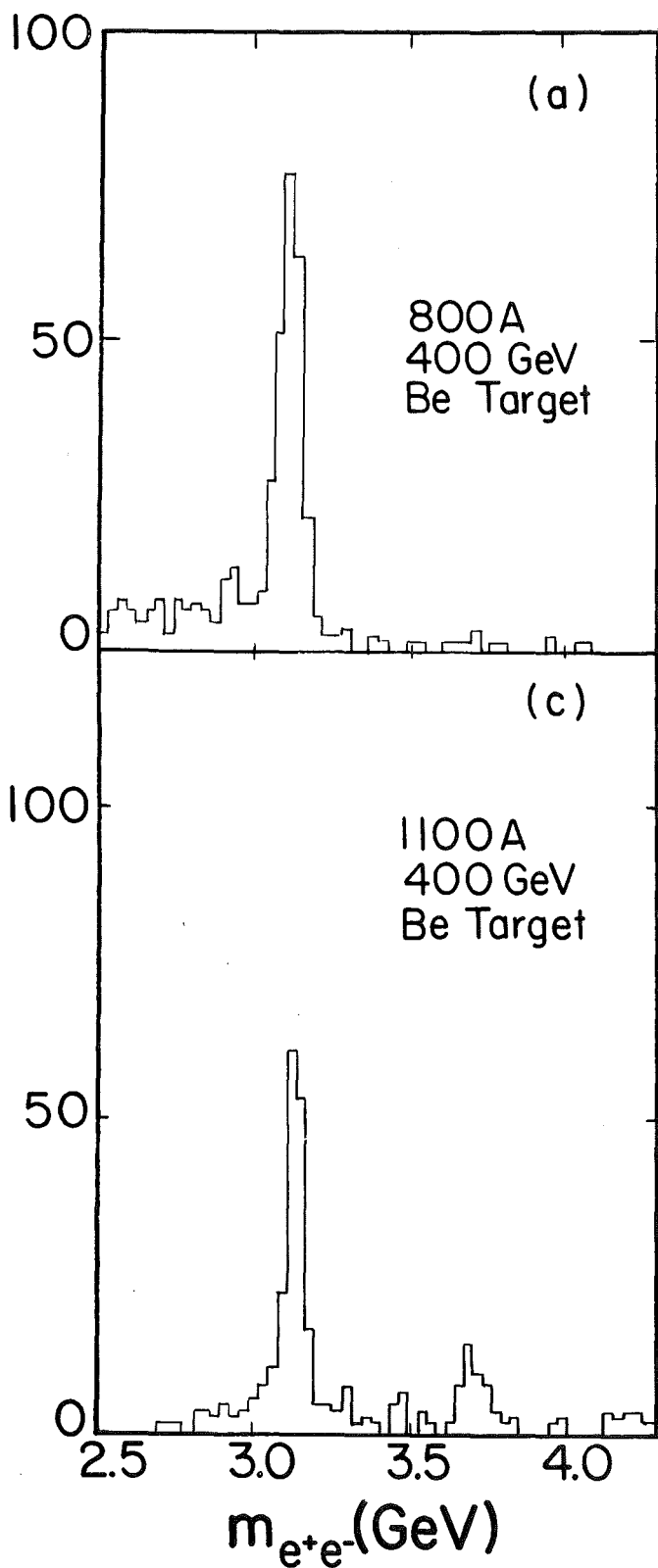


FIG. 12

ψ DATA DISTRIBUTION

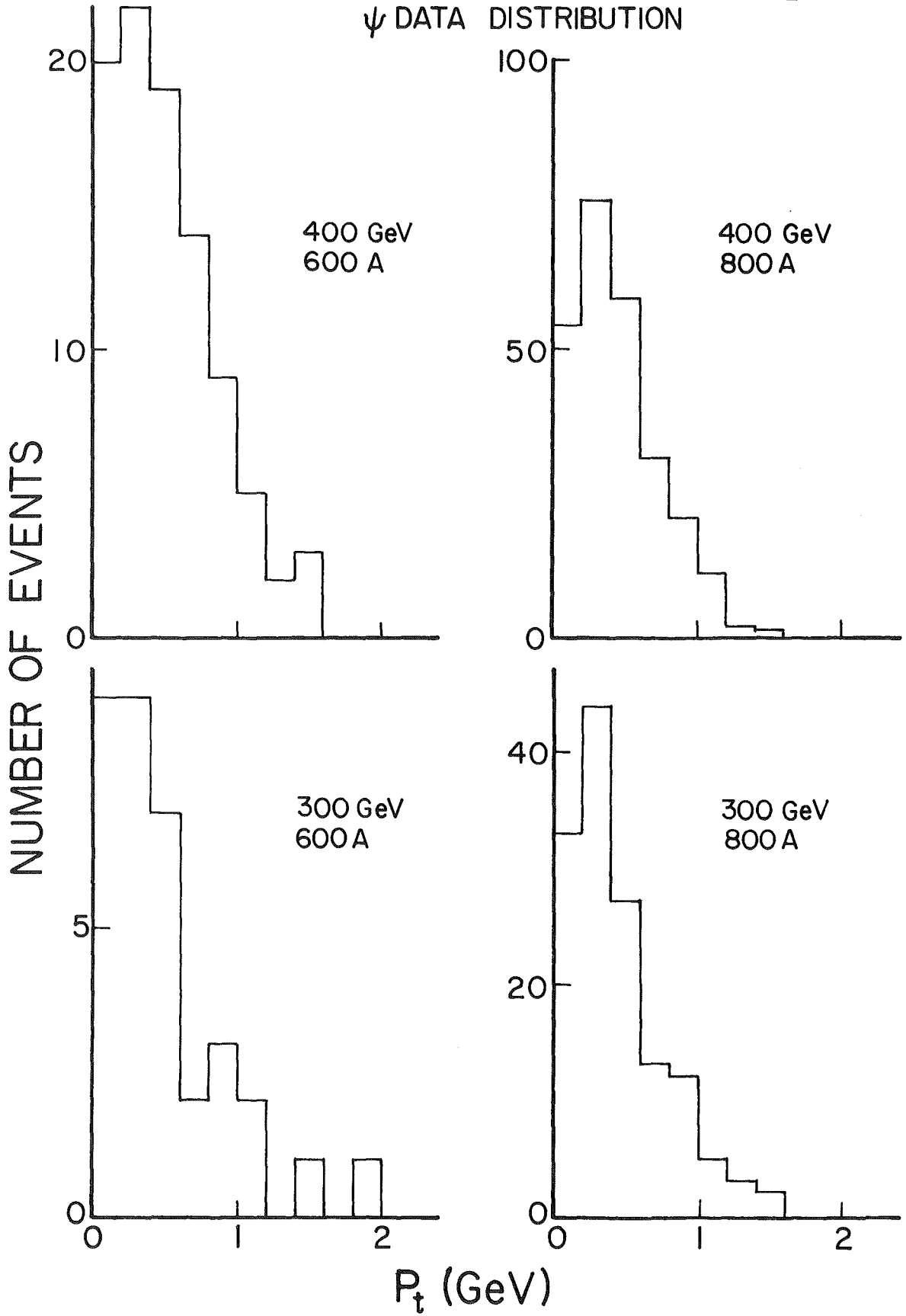
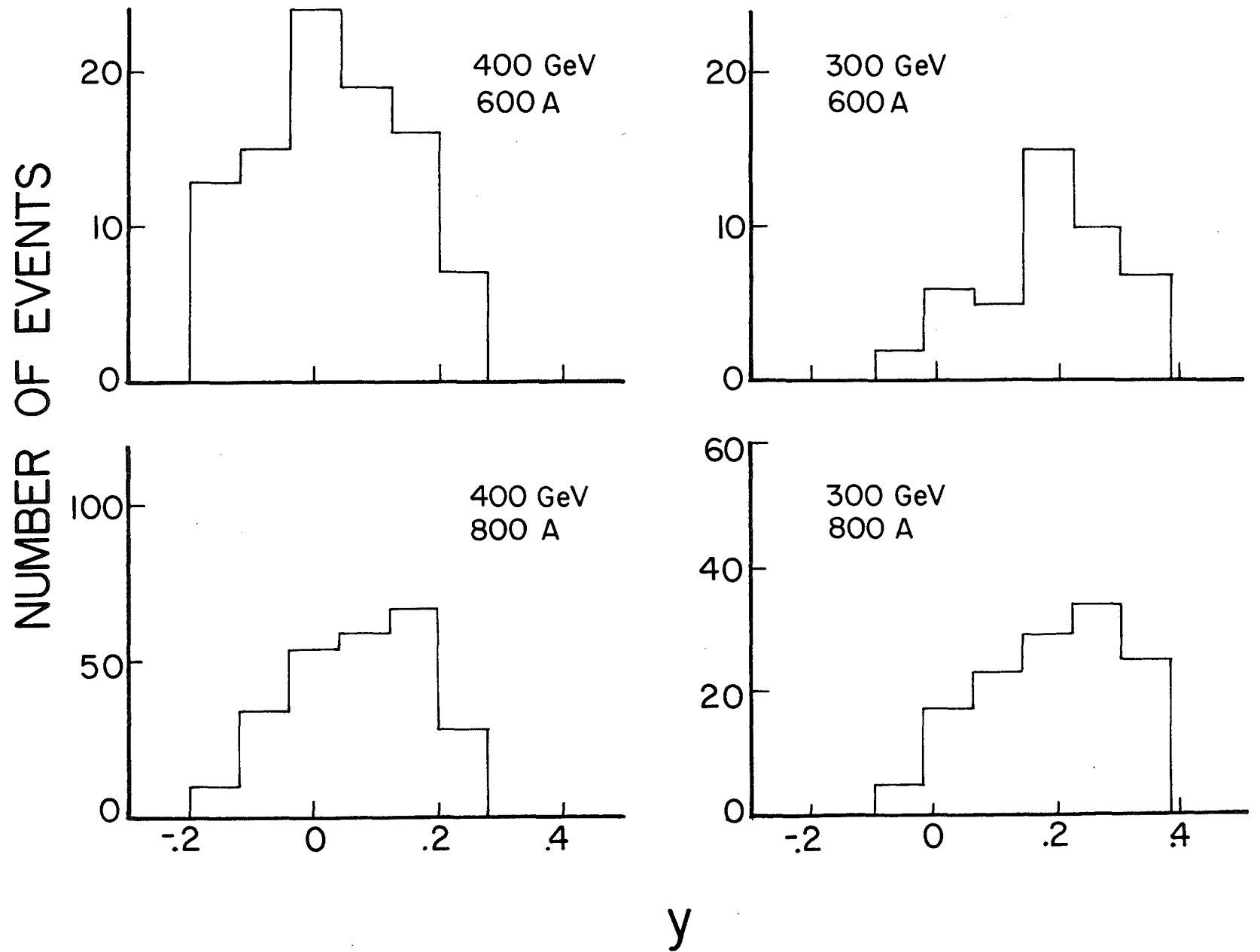


FIG. 13

ψ DATA DISTRIBUTION



y
FIG. 14

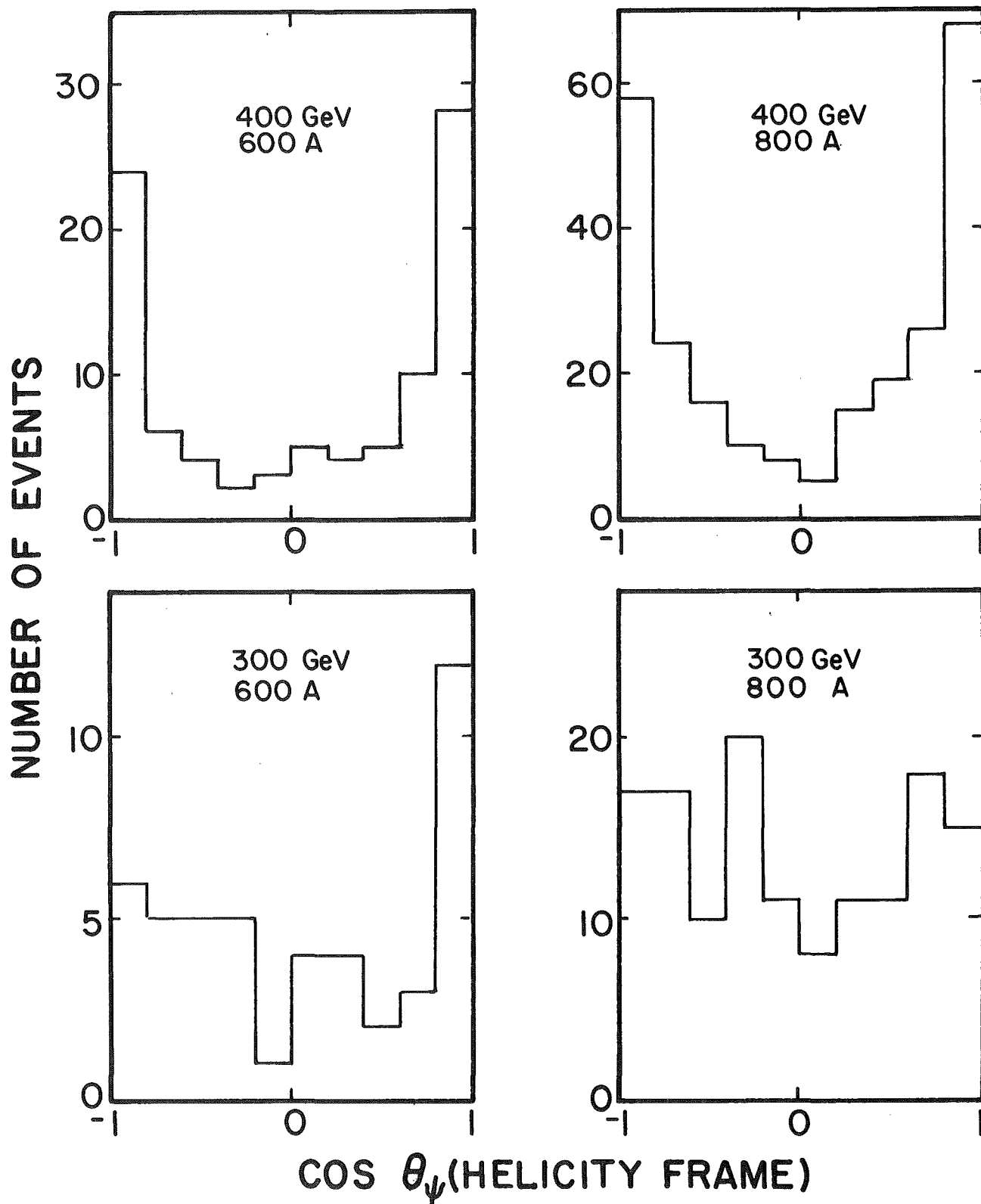


FIG. 15

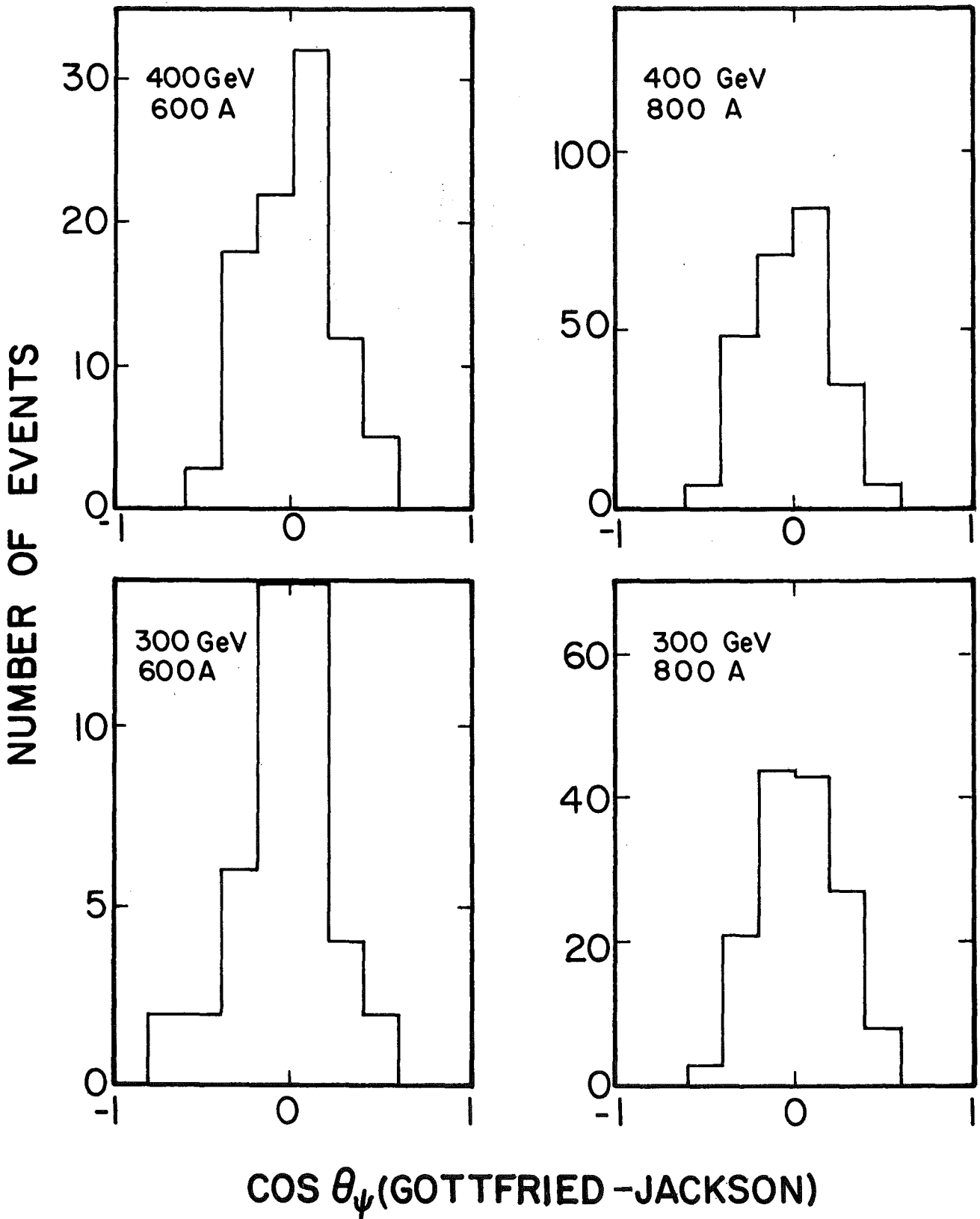


FIG. 16

ψ' 400 GeV 1100A DATA DISTRIBUTION

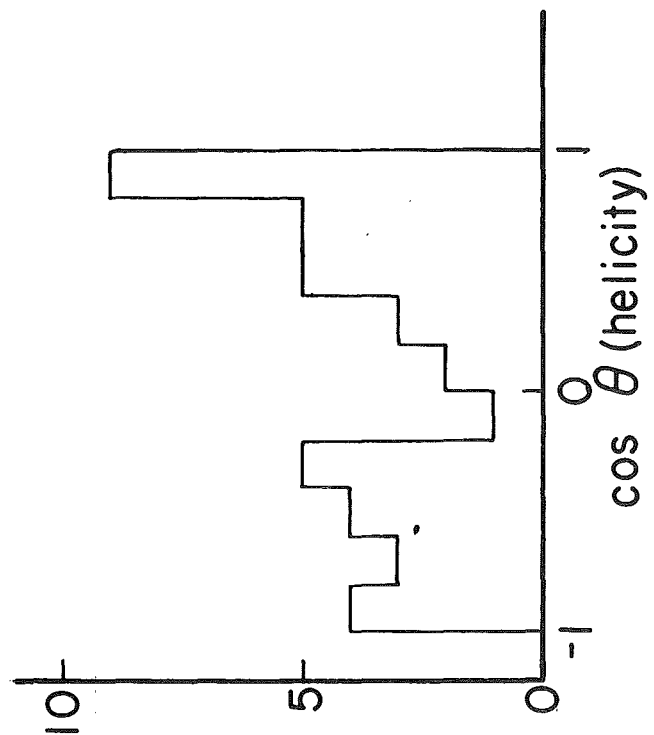
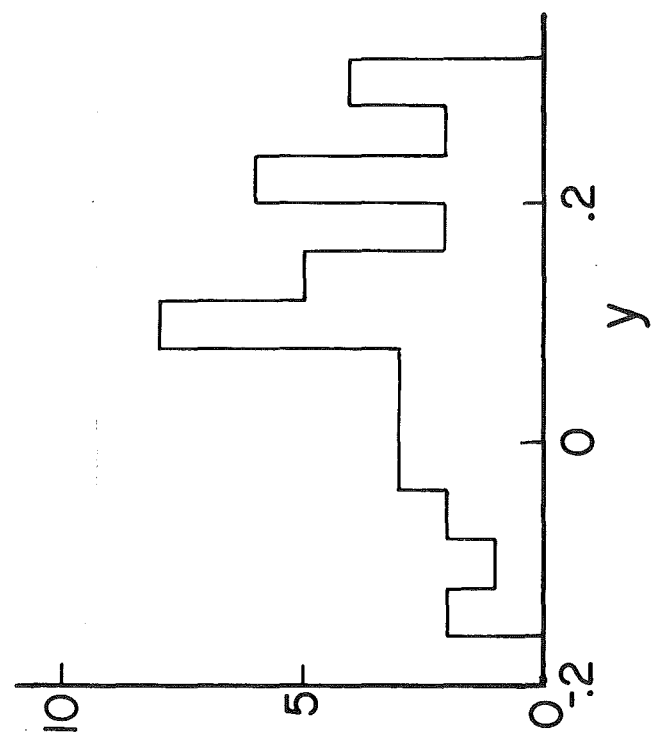
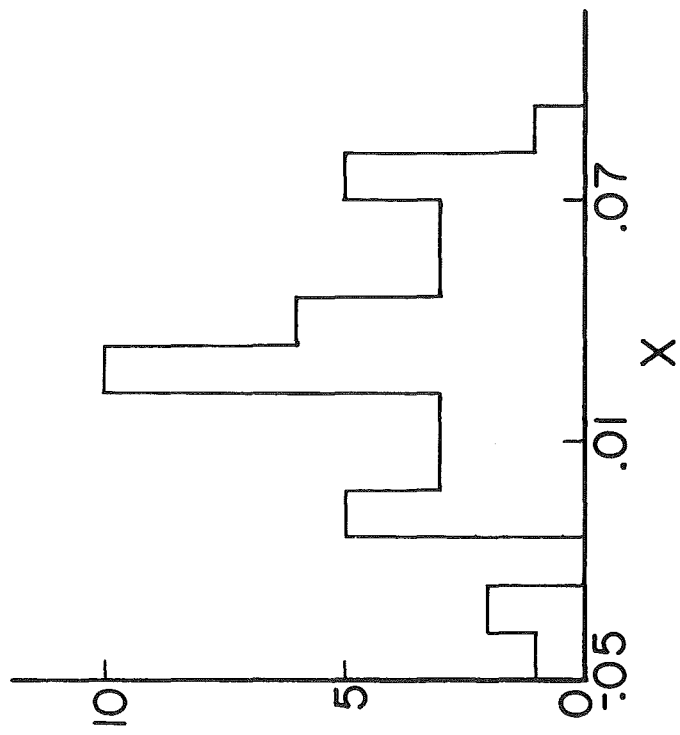
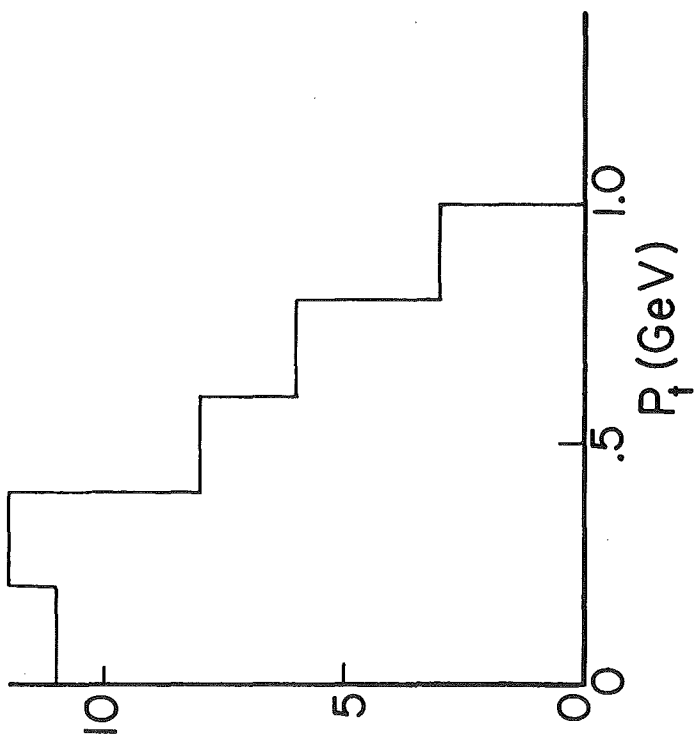
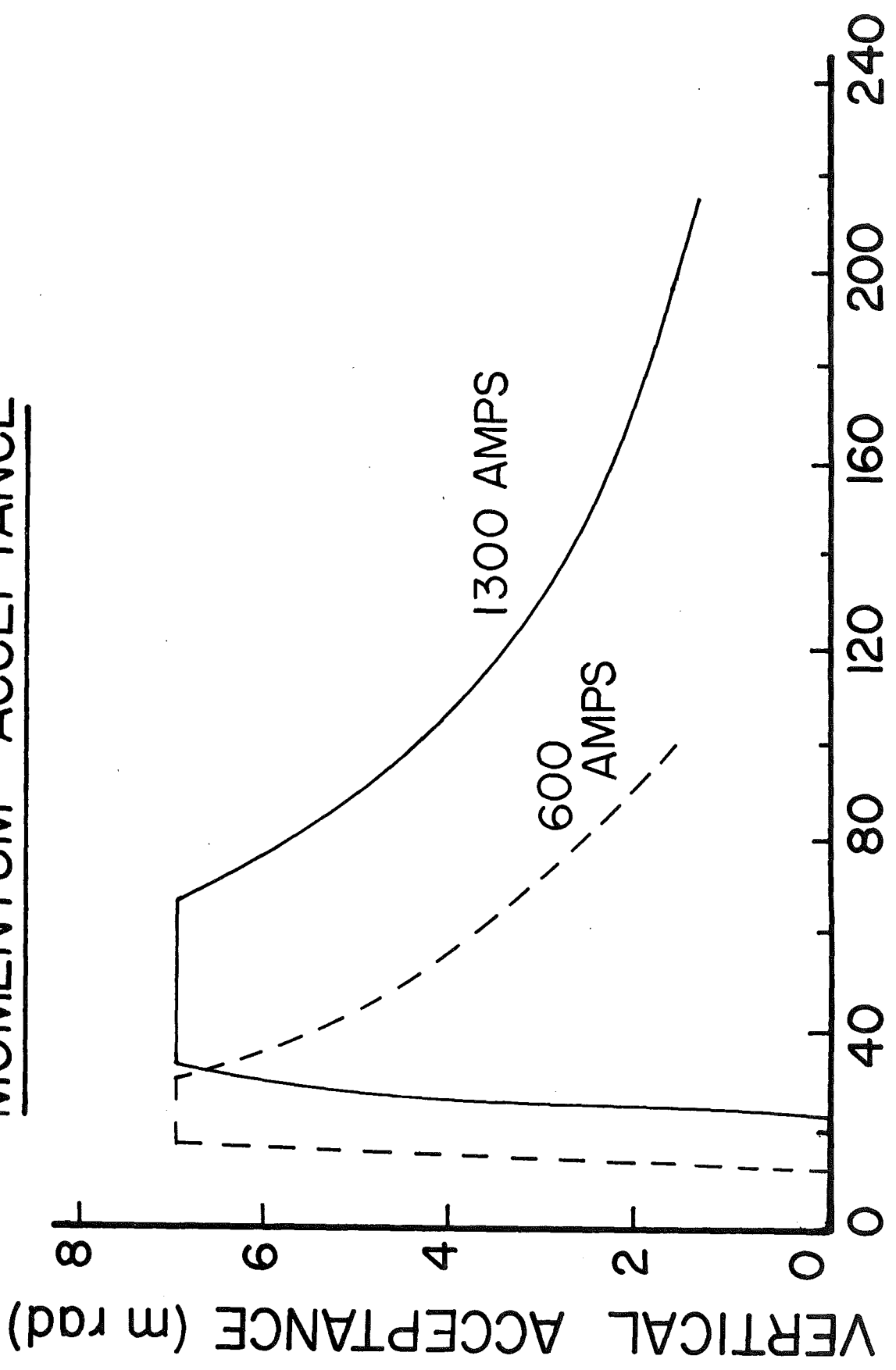


FIG. 17

MOMENTUM ACCEPTANCE



P (GeV/c)

FIG. 18

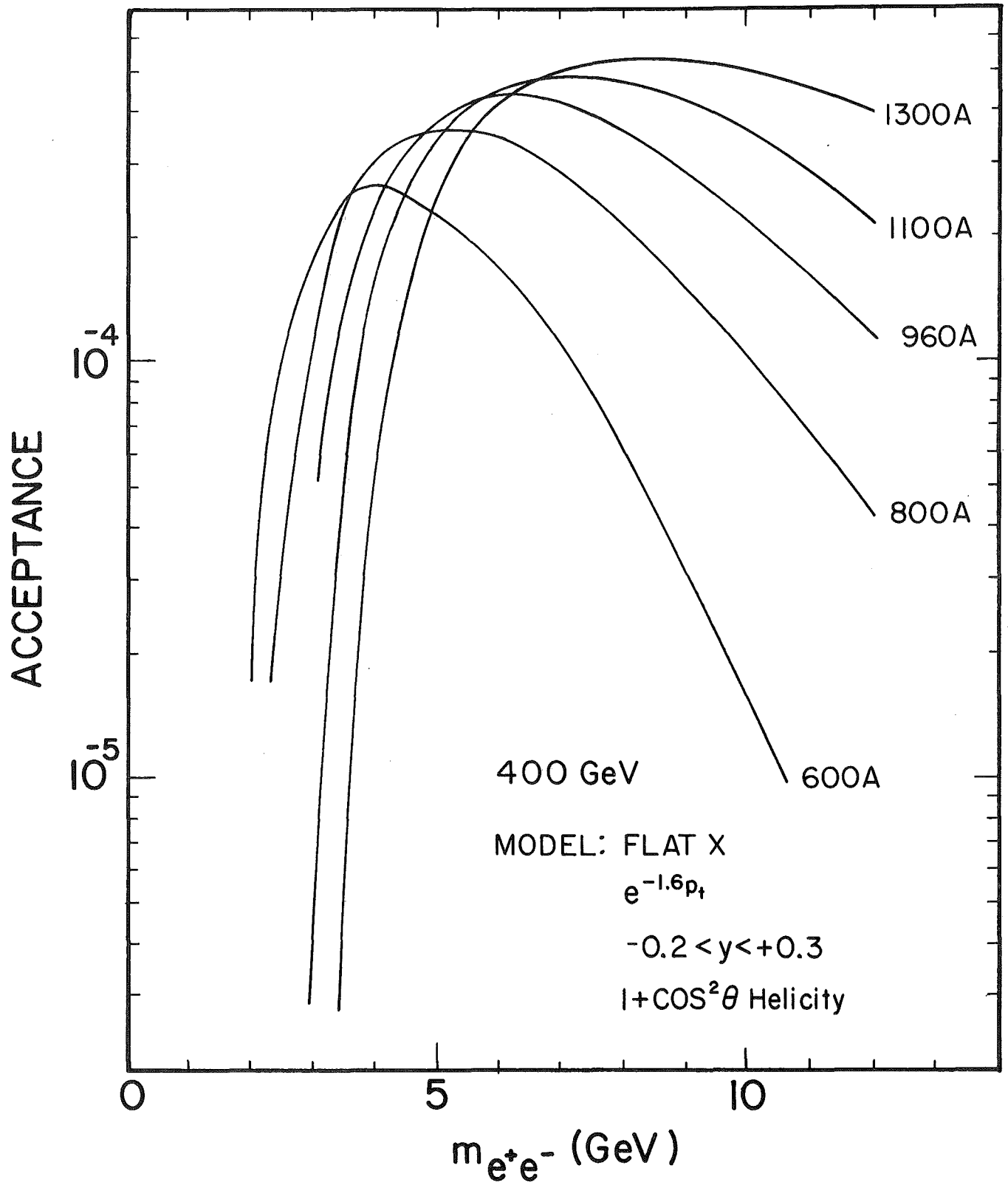


FIG. 19

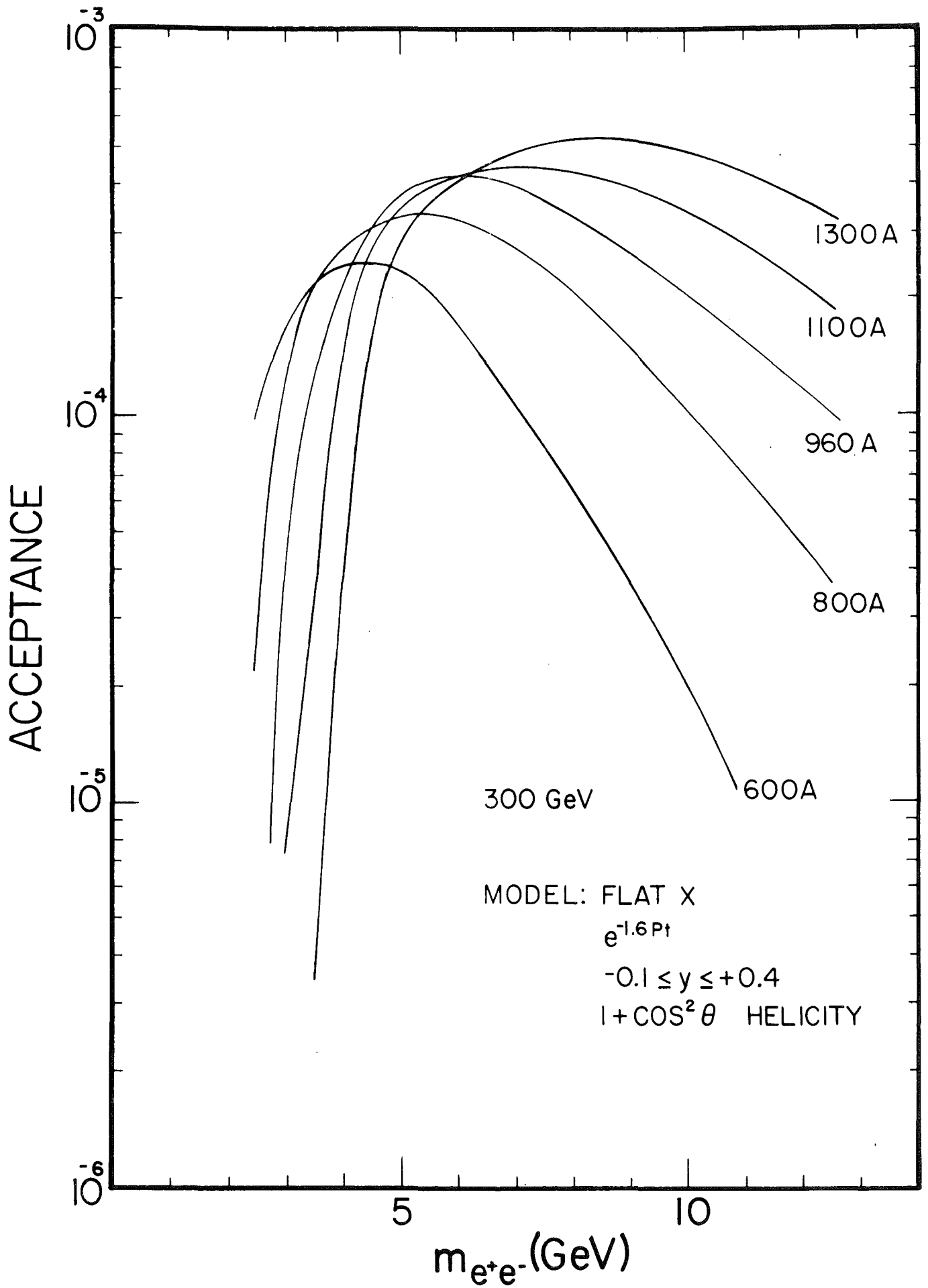


FIG. 20

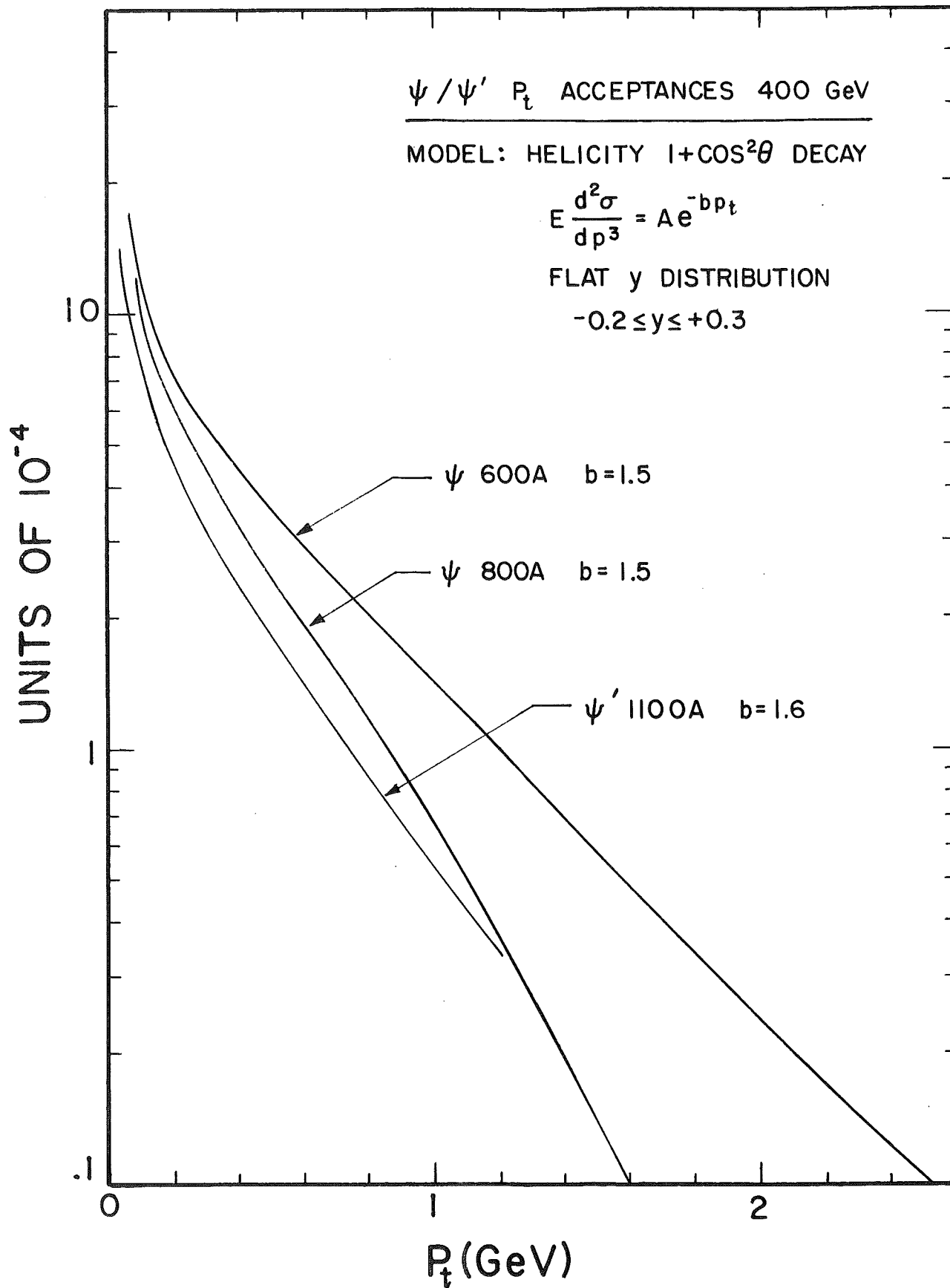


FIG. 21

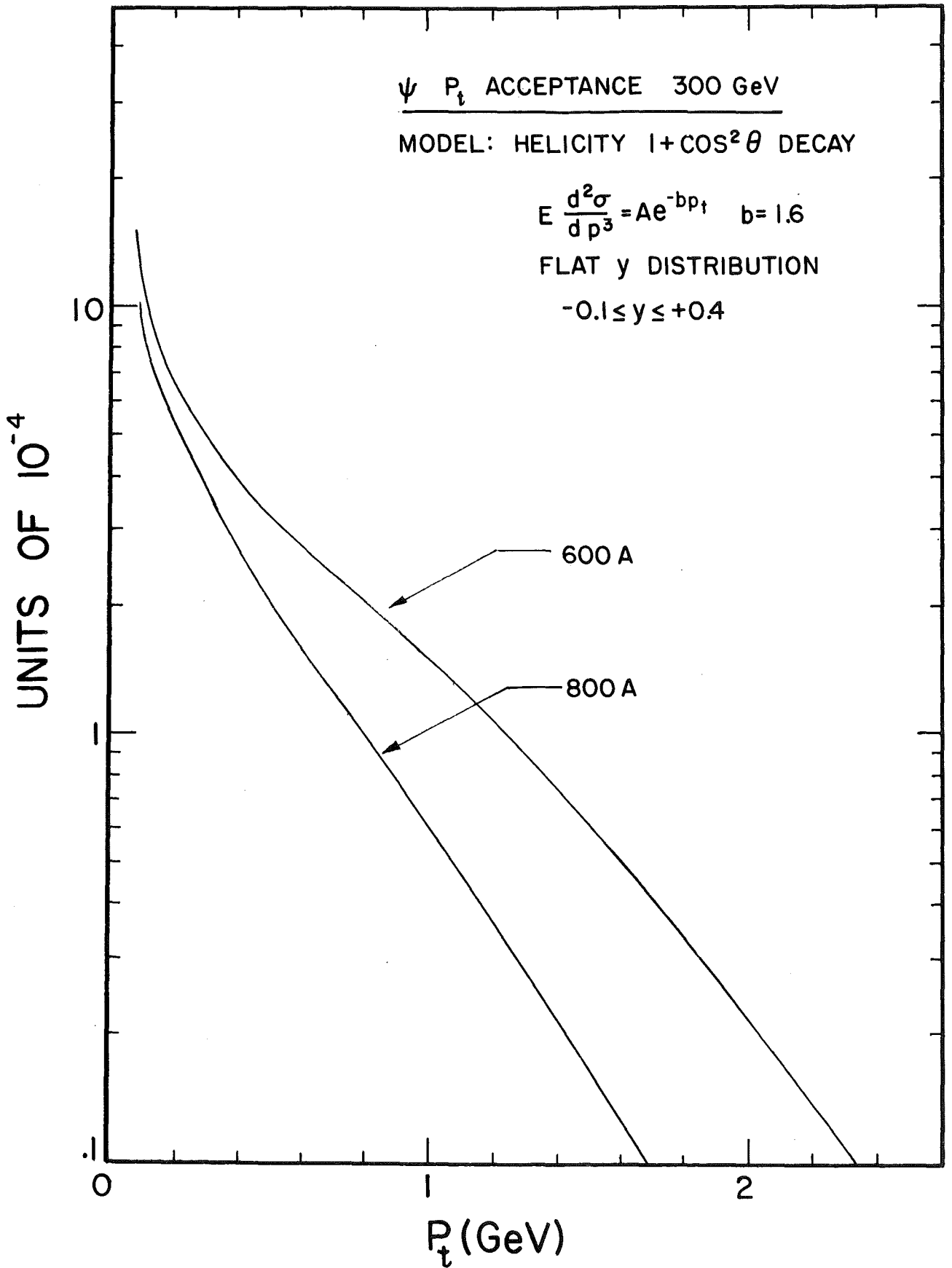
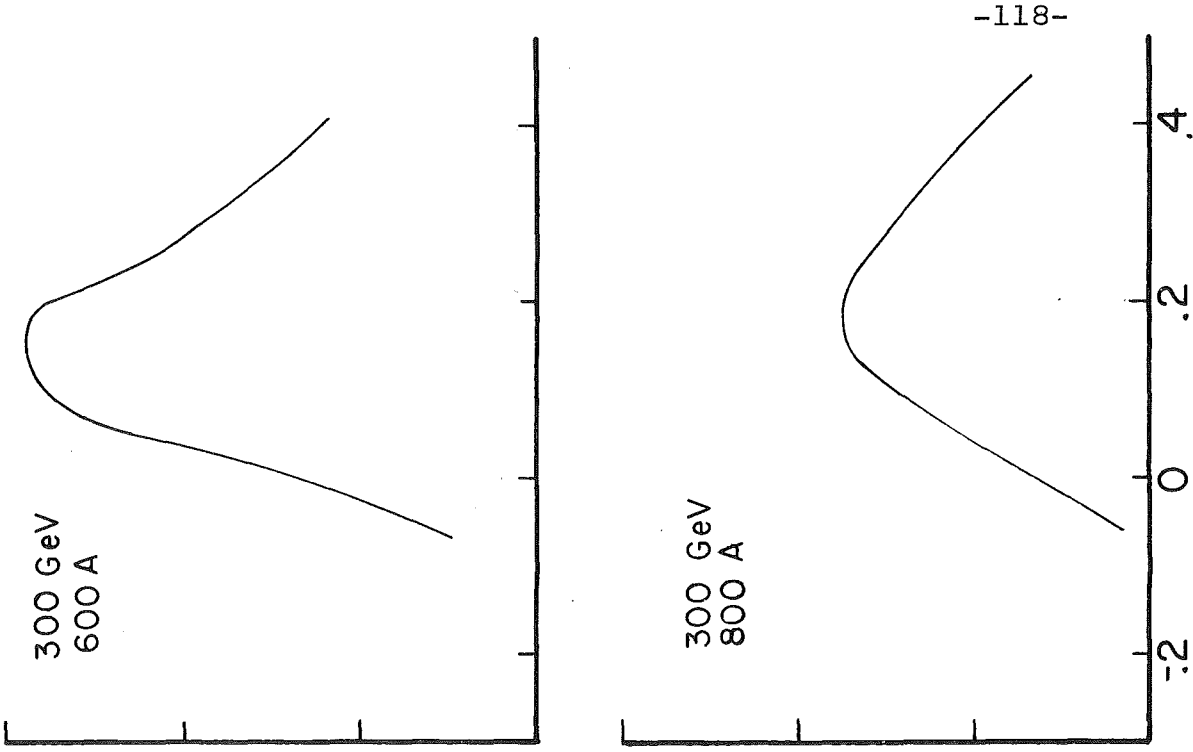
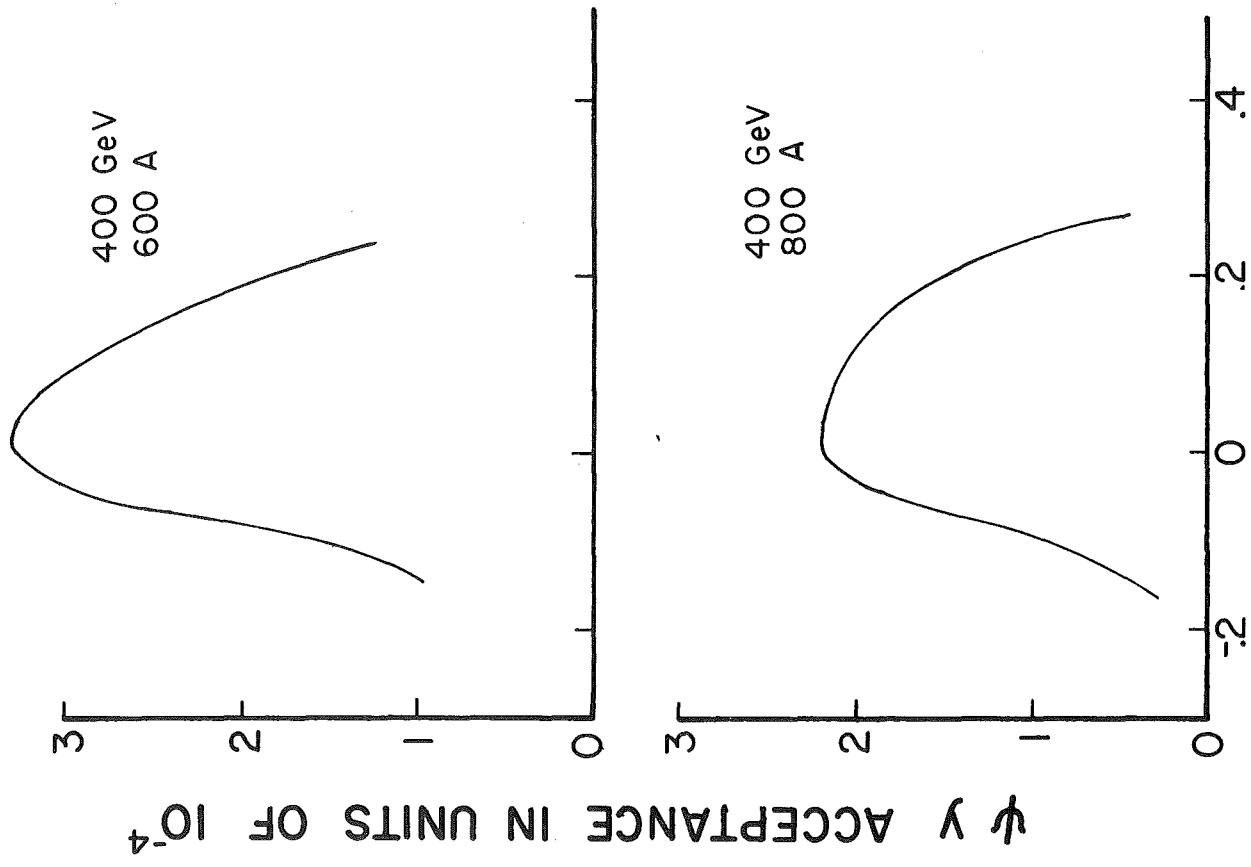


FIG. 22



-118-

y
FIG. 23

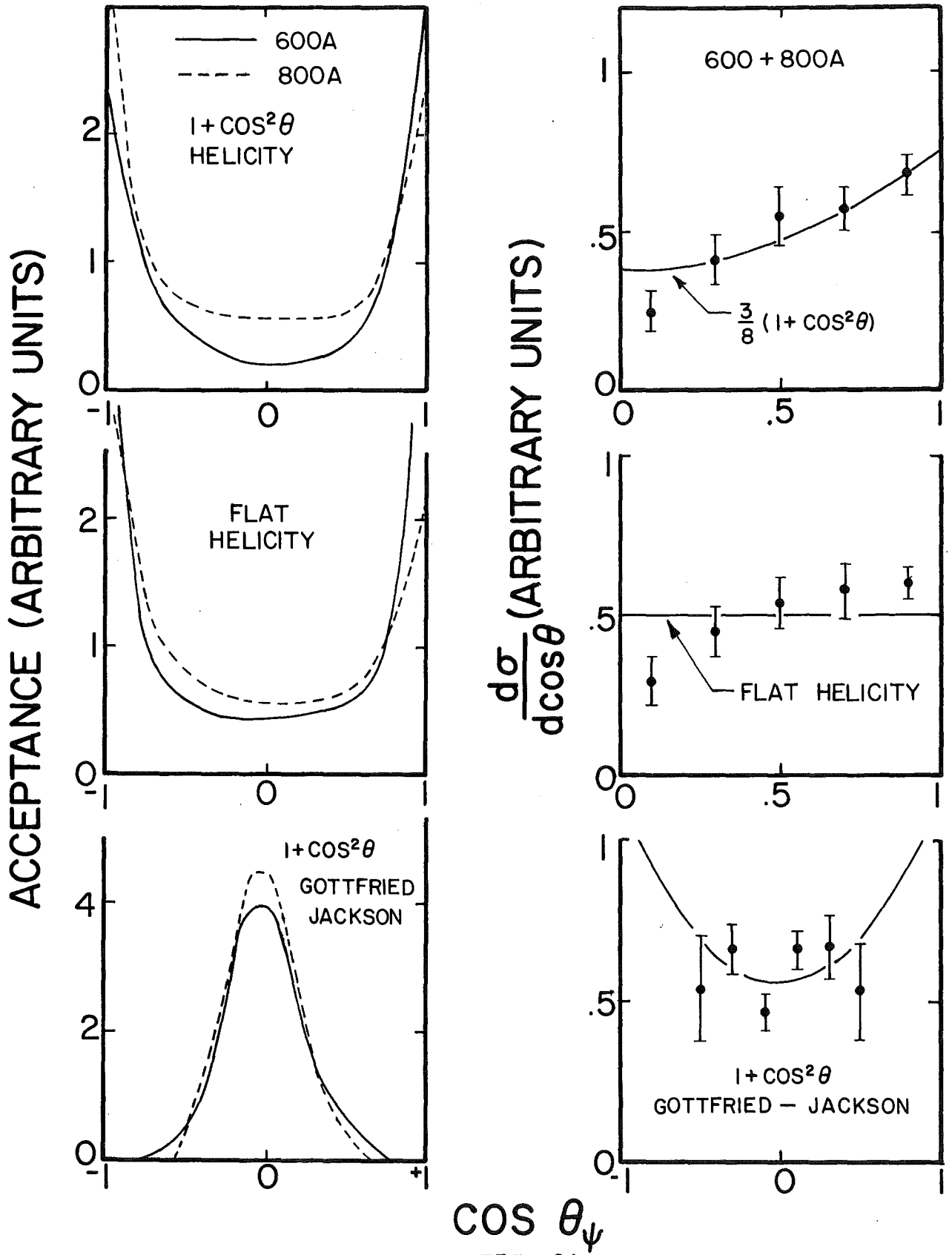


FIG. 24

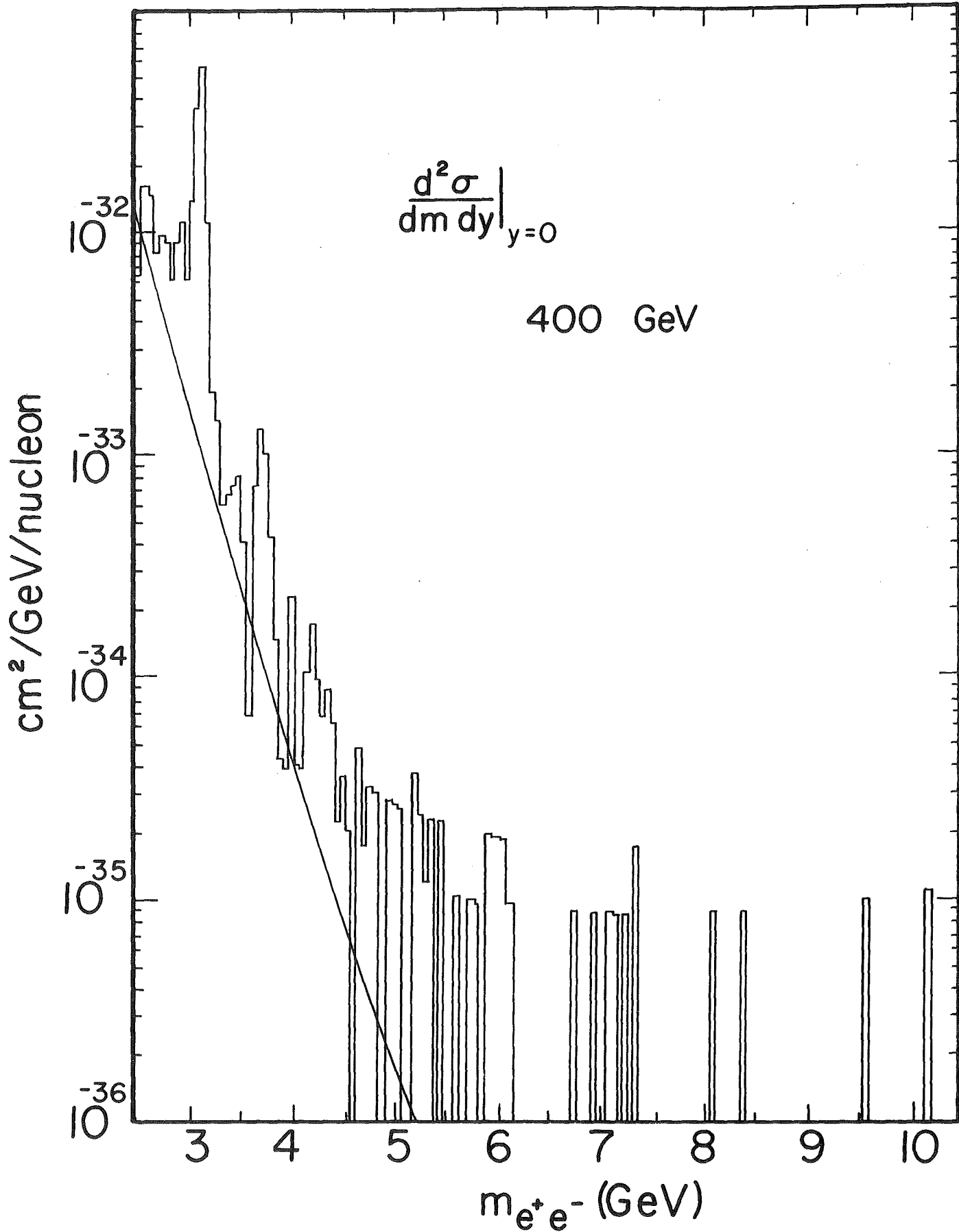


FIG. 25

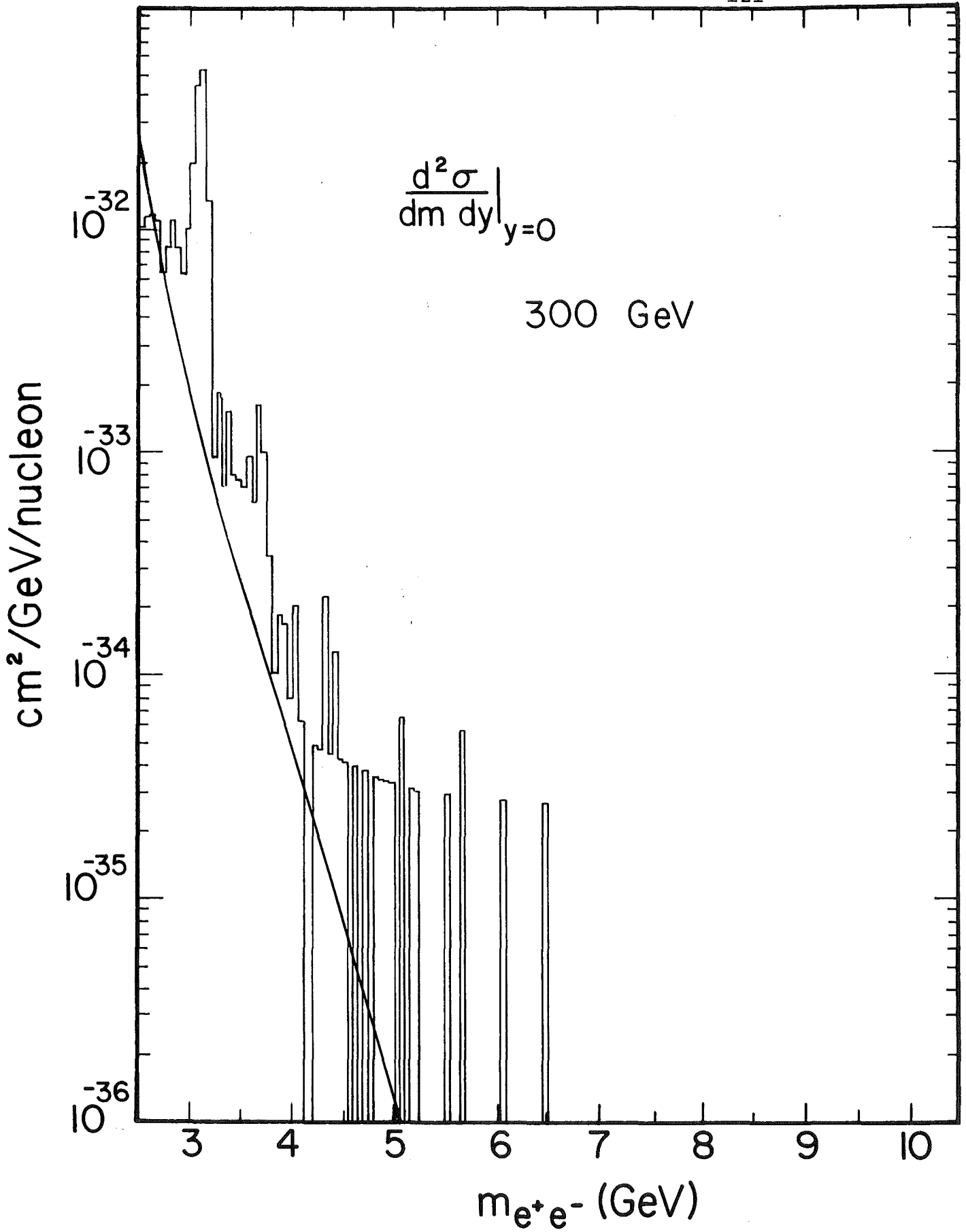


FIG. 26

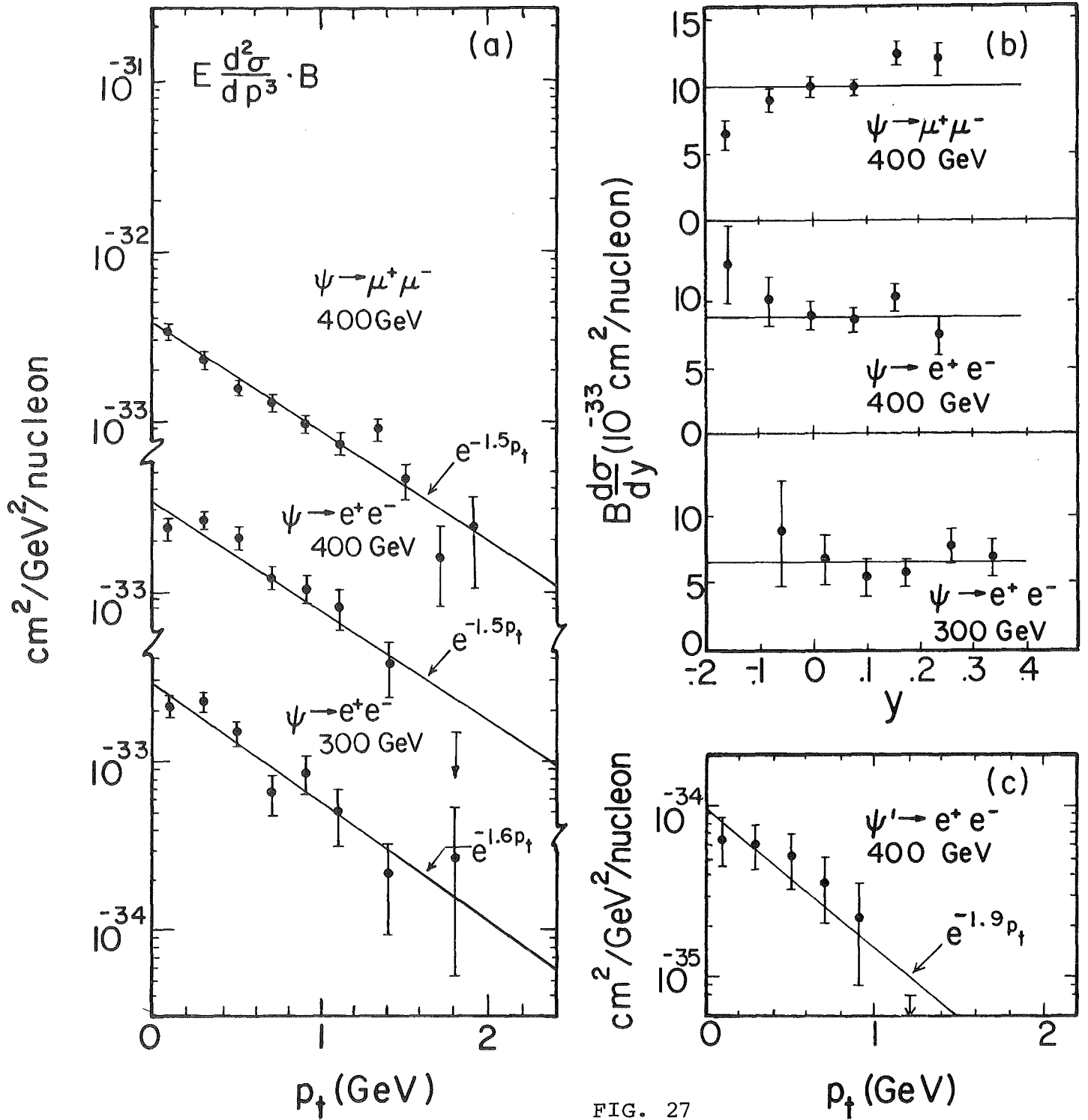


FIG. 27

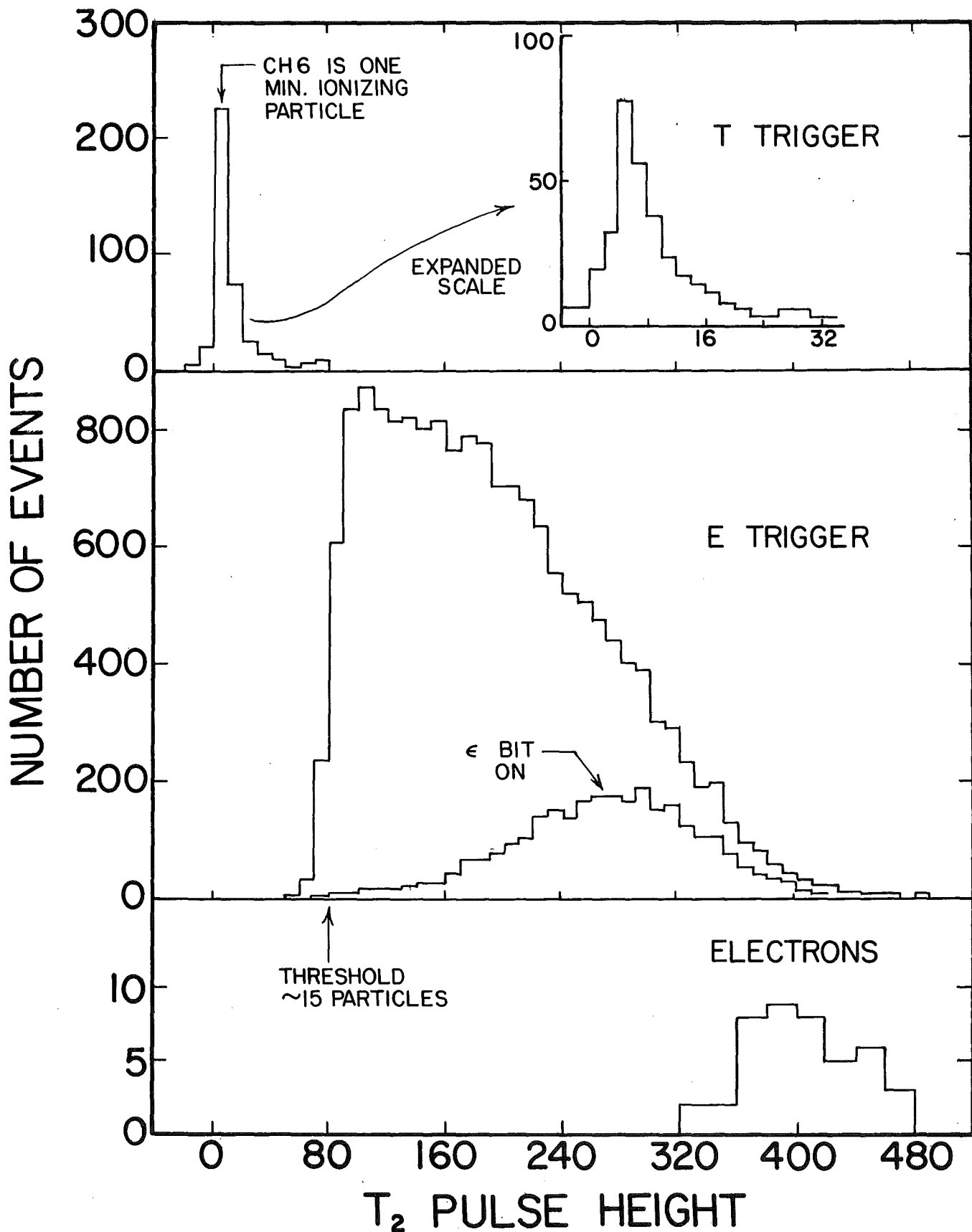


FIG. 28

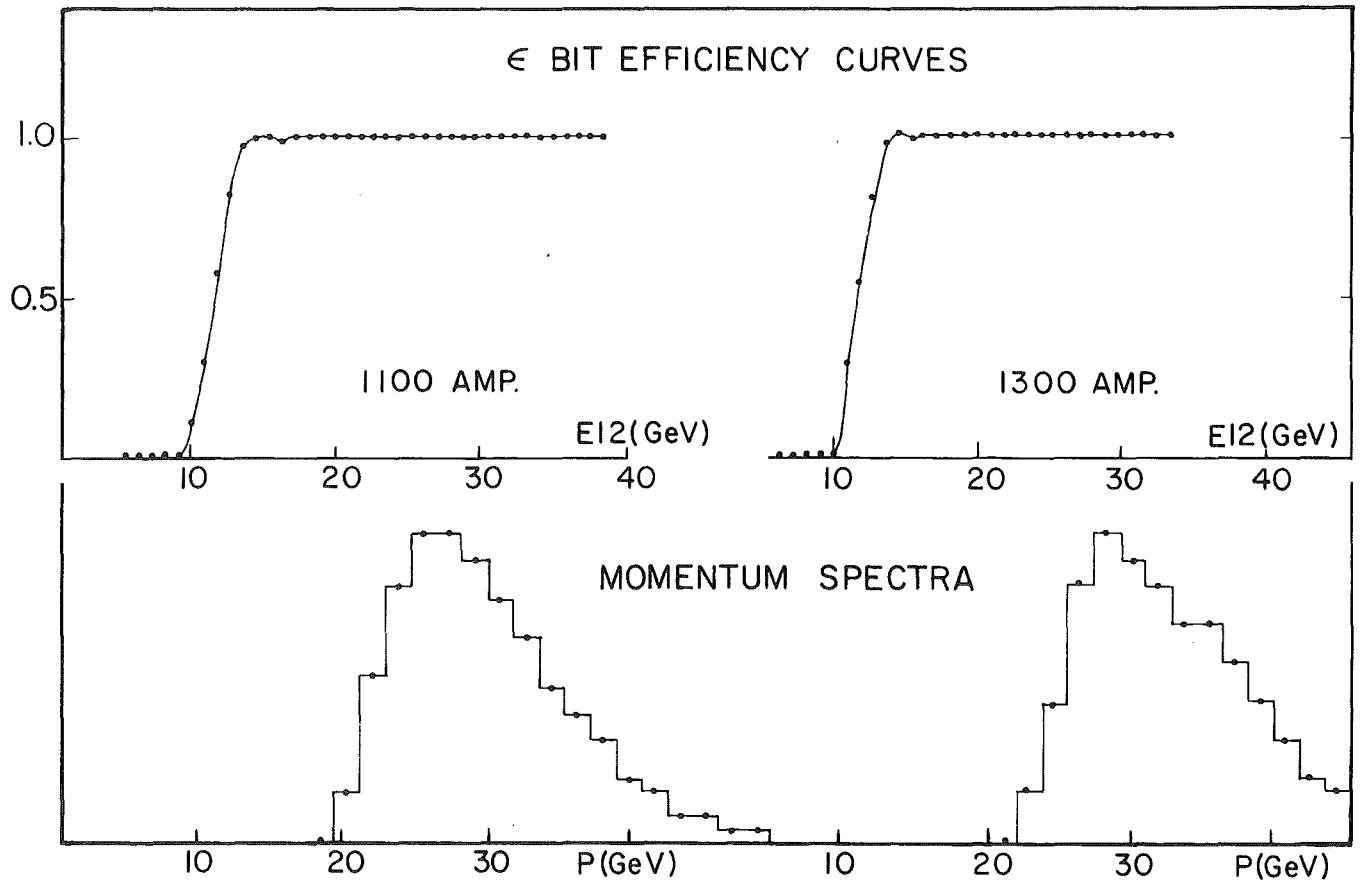
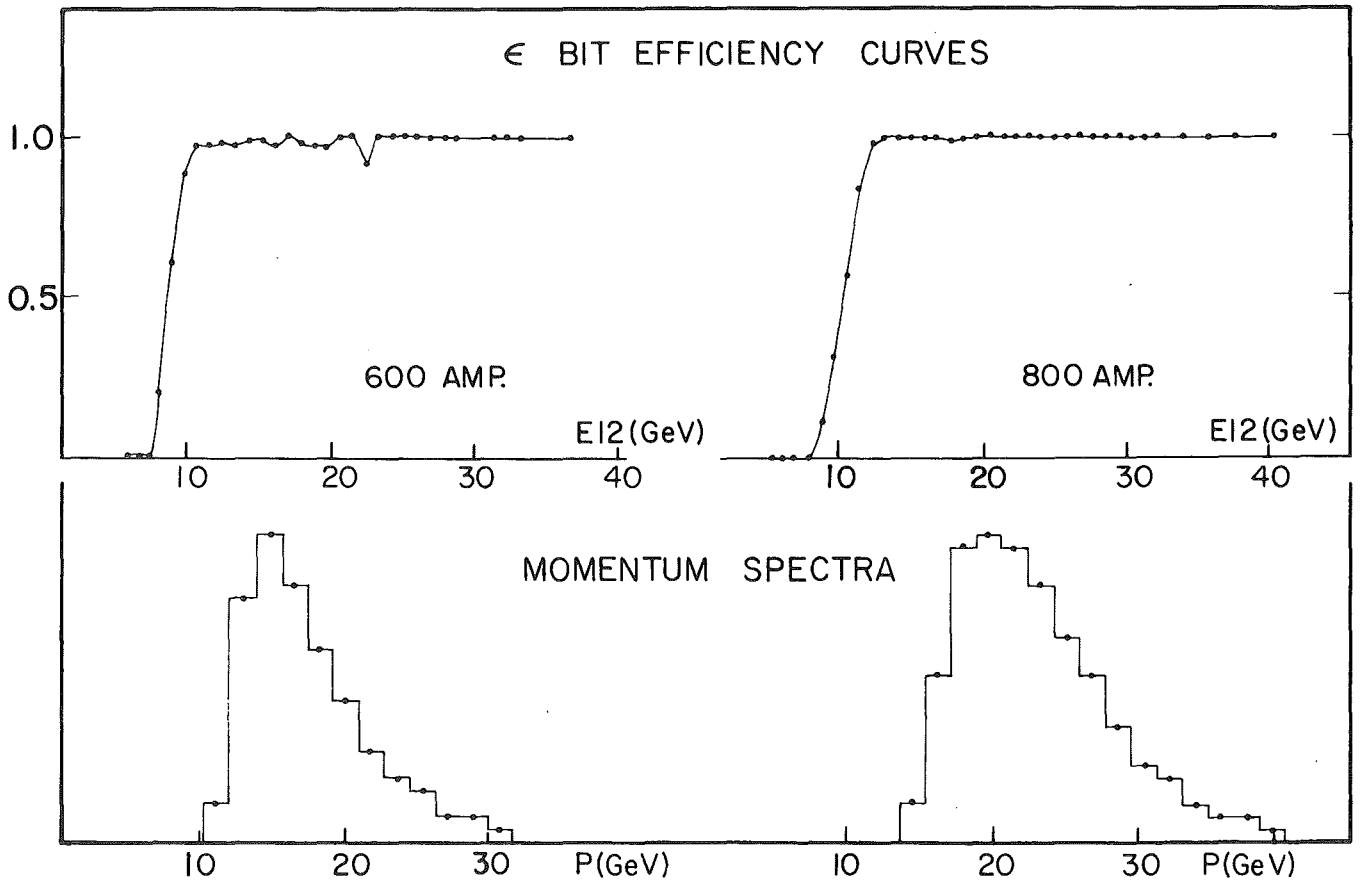


FIG. 29 , 30

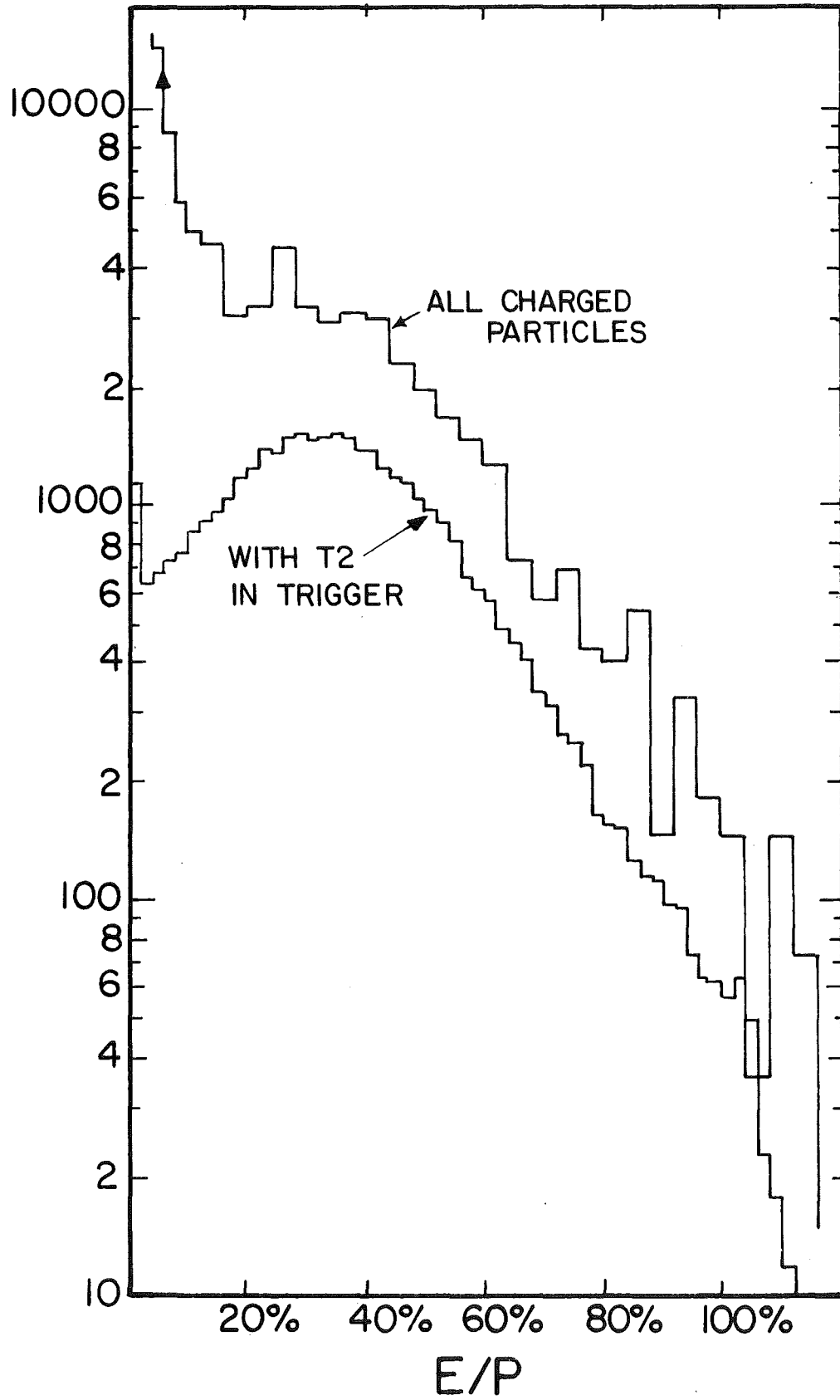


FIG. 31

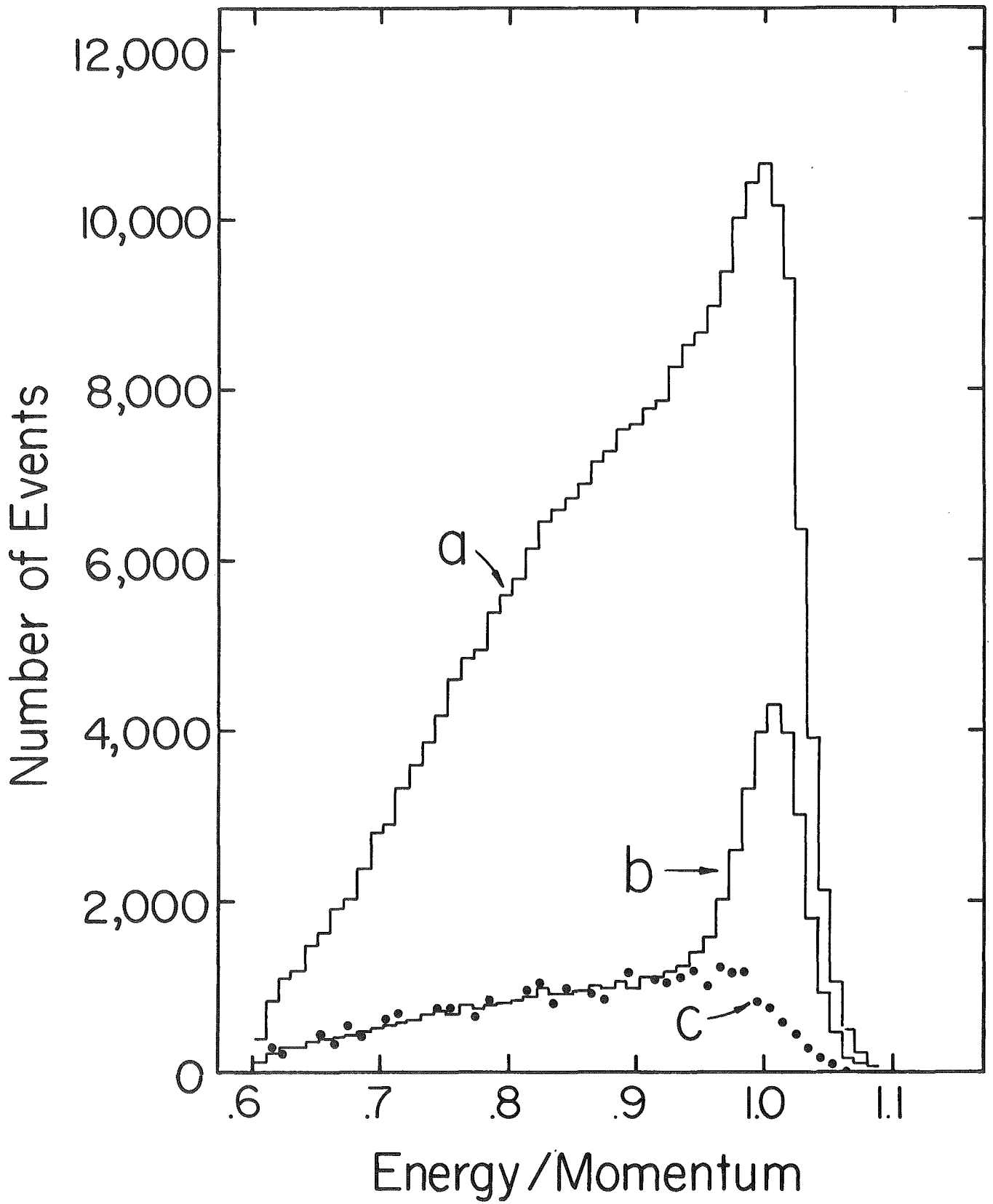
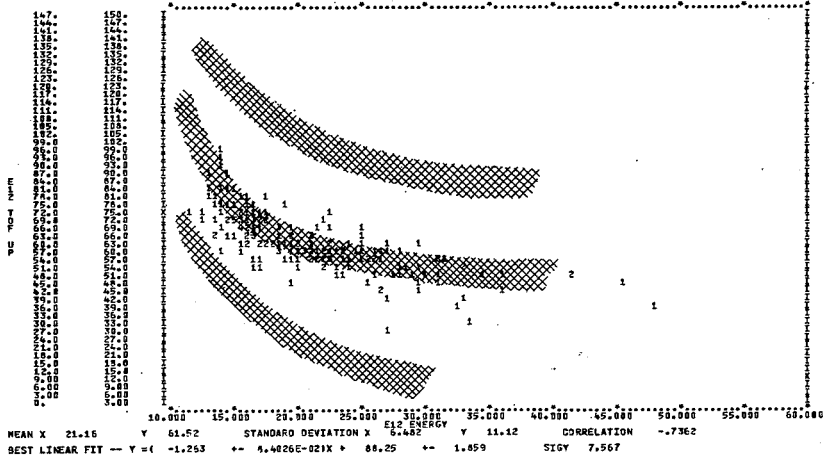
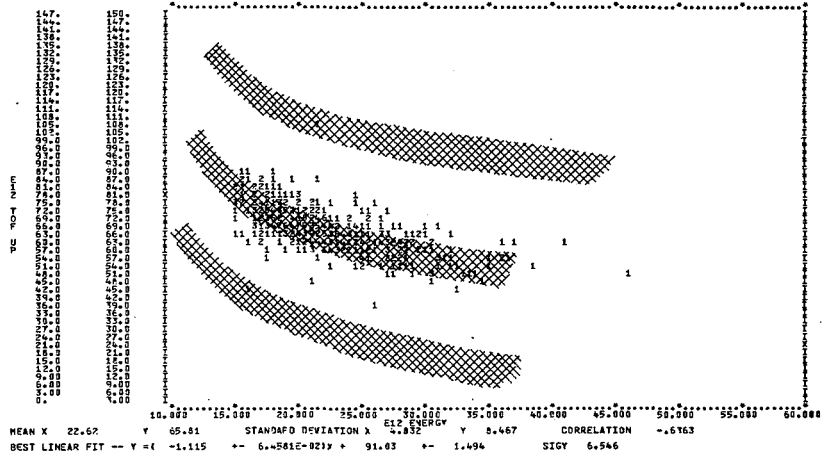


FIG. 32

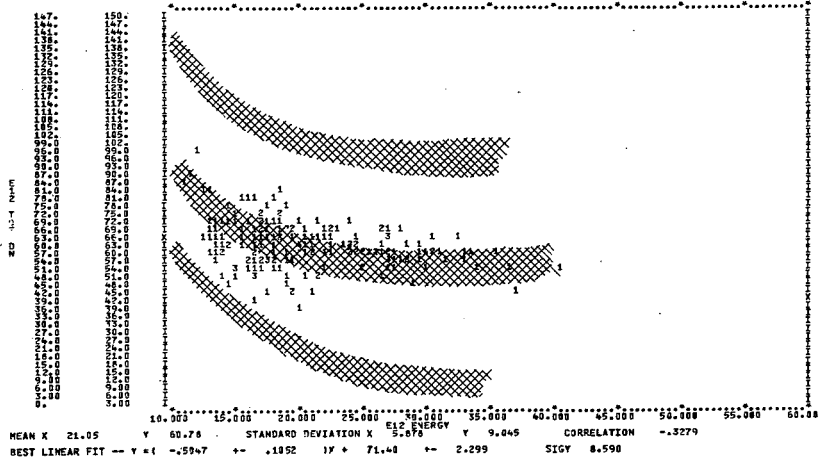
DATA FOR RUN BETWEEN 0 AND 1848 FOR CURRENTS 500
 SCATTER PLOT 13 OF E12 TOP UP VS E12 ENERGY, SE NO PILEUP UP 193. EVENTS (193. IN BOUNDS, UNWEIGHTED 18.28.53 02/27/77 PAGE 13



DATA FOR RUN BETWEEN 0 AND 1848 FOR CURRENTS 800
 SCATTER PLOT 13 OF E12 TOP UP VS E12 ENERGY, SE NO PILEUP UP 440. EVENTS (440. IN BOUNDS, UNWEIGHTED 18.29.53 02/27/77 PAGE 38



DATA FOR RUN BETWEEN 0 AND 1848 FOR CURRENTS 500
 SCATTER PLOT 14 OF E12 TOP DOWN VS E12 ENERGY, SE NO PILEUP DOWN 193. EVENTS (193. IN BOUNDS, UNWEIGHTED 18.29.53 02/27/77 PAGE 15



DATA FOR RUN BETWEEN 0 AND 1848 FOR CURRENTS 800
 SCATTER PLOT 14 OF E12 TOP DOWN VS E12 ENERGY, SE NO PILEUP DOWN 440. EVENTS (440. IN BOUNDS, UNWEIGHTED 18.29.53 02/27/77 PAGE 31

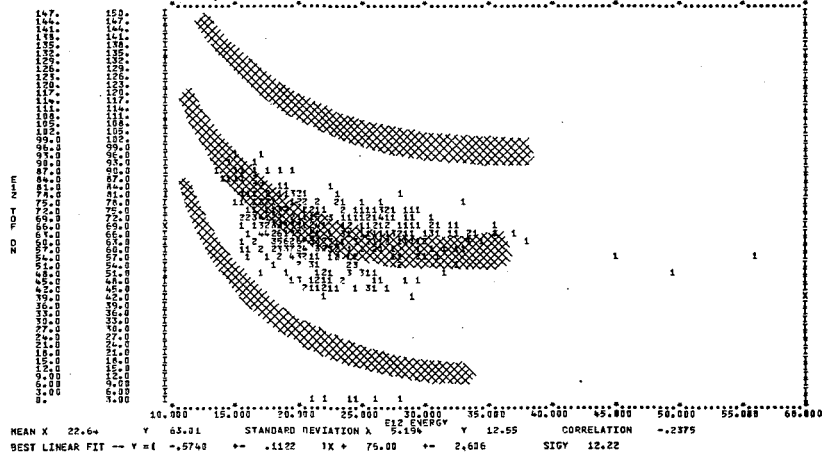
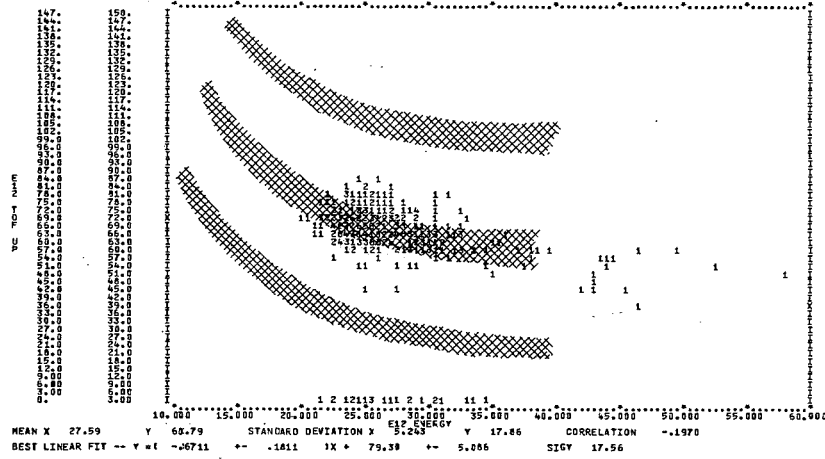
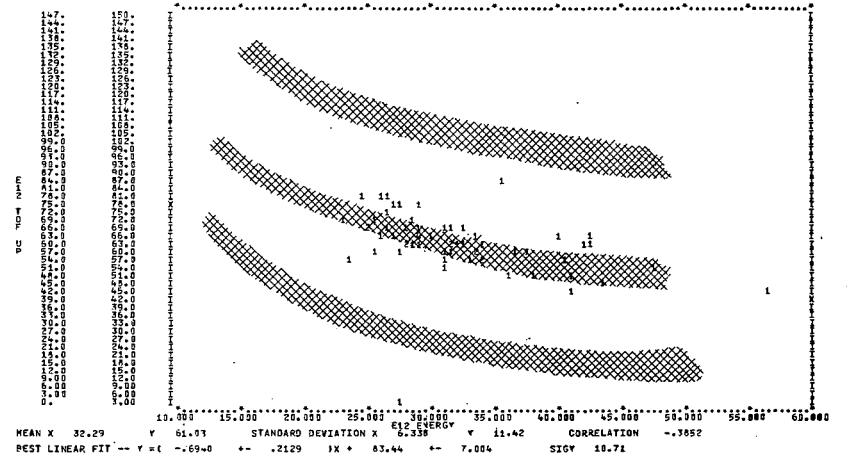


FIG. 33a

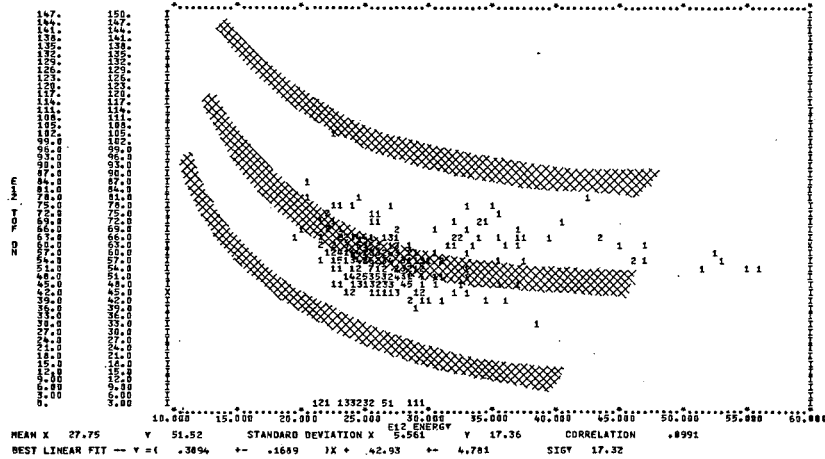
DATA FOR RUN BETWEEN 0 AND 1848 FOR CURRENTS 1200 UP VS E12 ENERGY, EE NO PILEUP UP 345. EVENTS (342. IN BOUNDS, UNWEIGHTED 18.28.53 82/27/77 PAGE 62



DATA FOR RUN BETWEEN 0 AND 1848 FOR CURRENTS 1200 UP VS E12 ENERGY, EE NO PILEUP UP 65. EVENTS (63. IN BOUNDS, UNWEIGHTED 18.28.53 82/27/77 PAGE 78



DATA FOR RUN BETWEEN 0 AND 1848 FOR CURRENTS 1200 DOWN VS E12 ENERGY, EE NO PILEUP DOWN 345. EVENTS (340. IN BOUNDS, UNWEIGHTED 18.28.53 82/27/77 PAGE 63



DATA FOR RUN BETWEEN 0 AND 1848 FOR CURRENTS 1200 DOWN VS E12 ENERGY, EE NO PILEUP DOWN 65. EVENTS (63. IN BOUNDS, UNWEIGHTED 18.28.53 82/27/77 PAGE 79

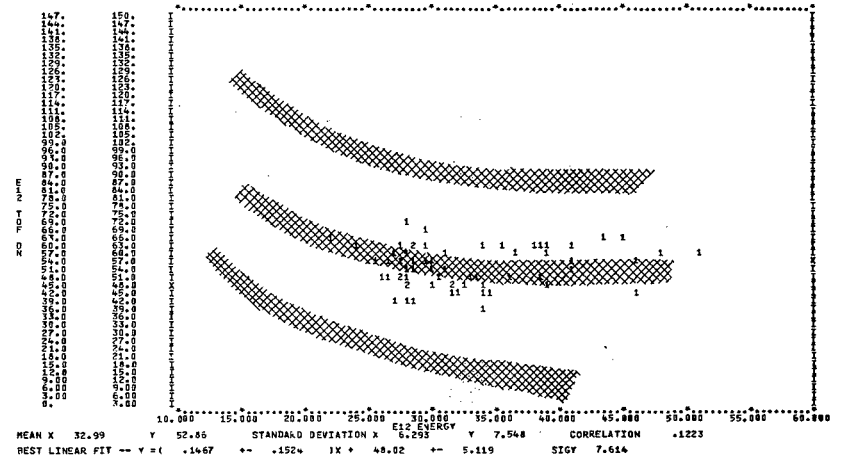


FIG. 33b.

2.8 < m < 3.2 600 AMPS

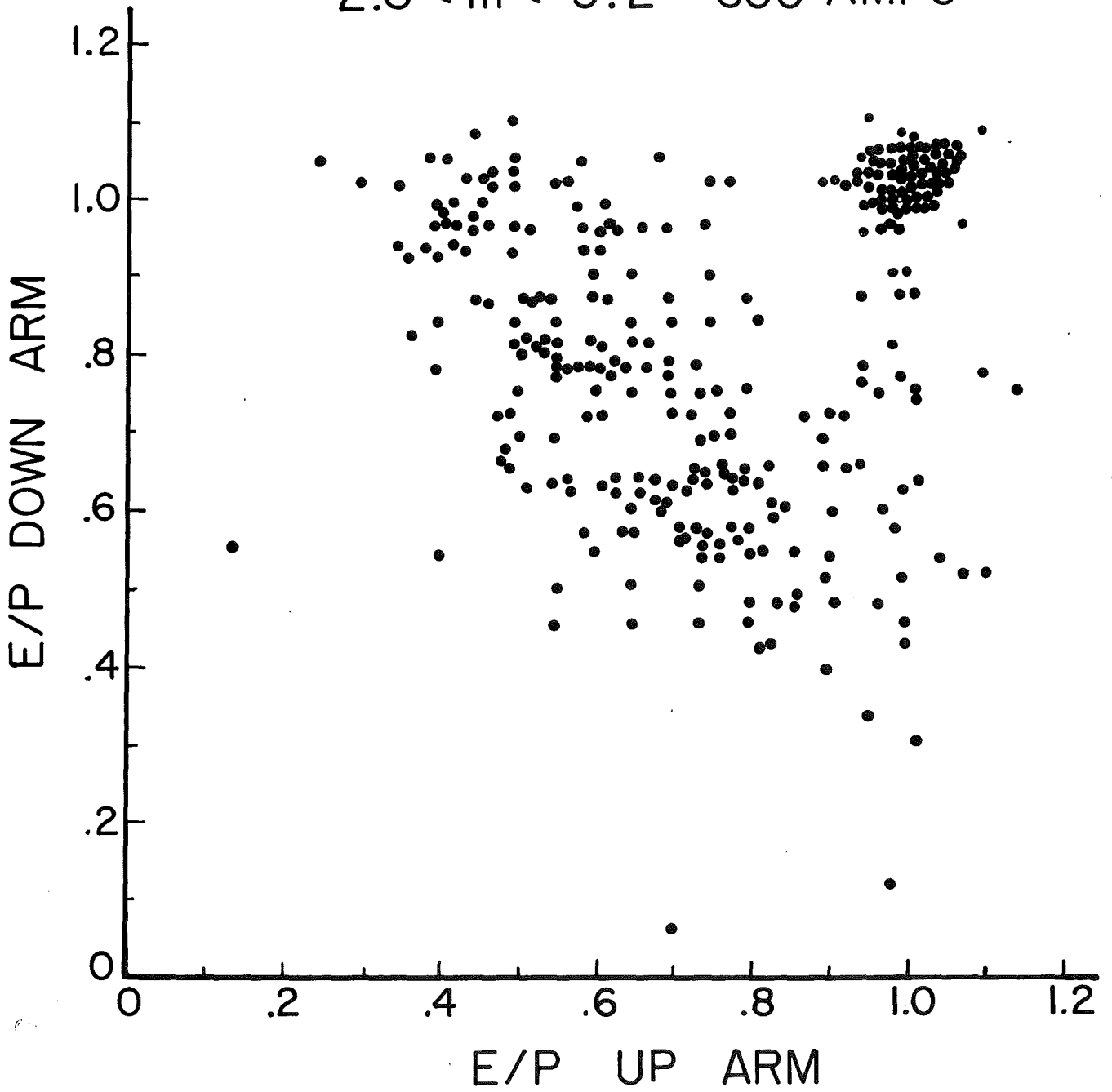


FIG. 34

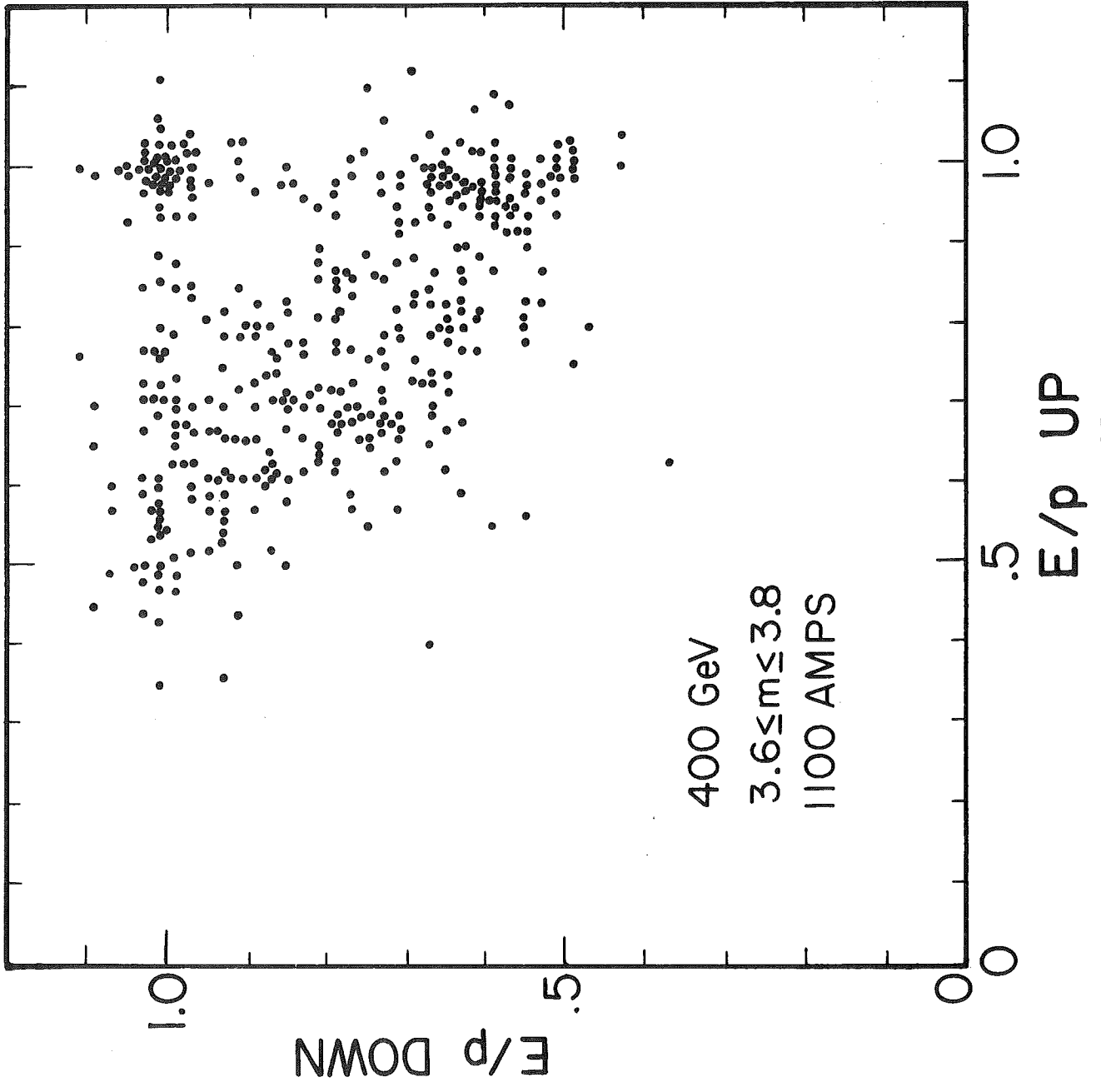


FIG. 35

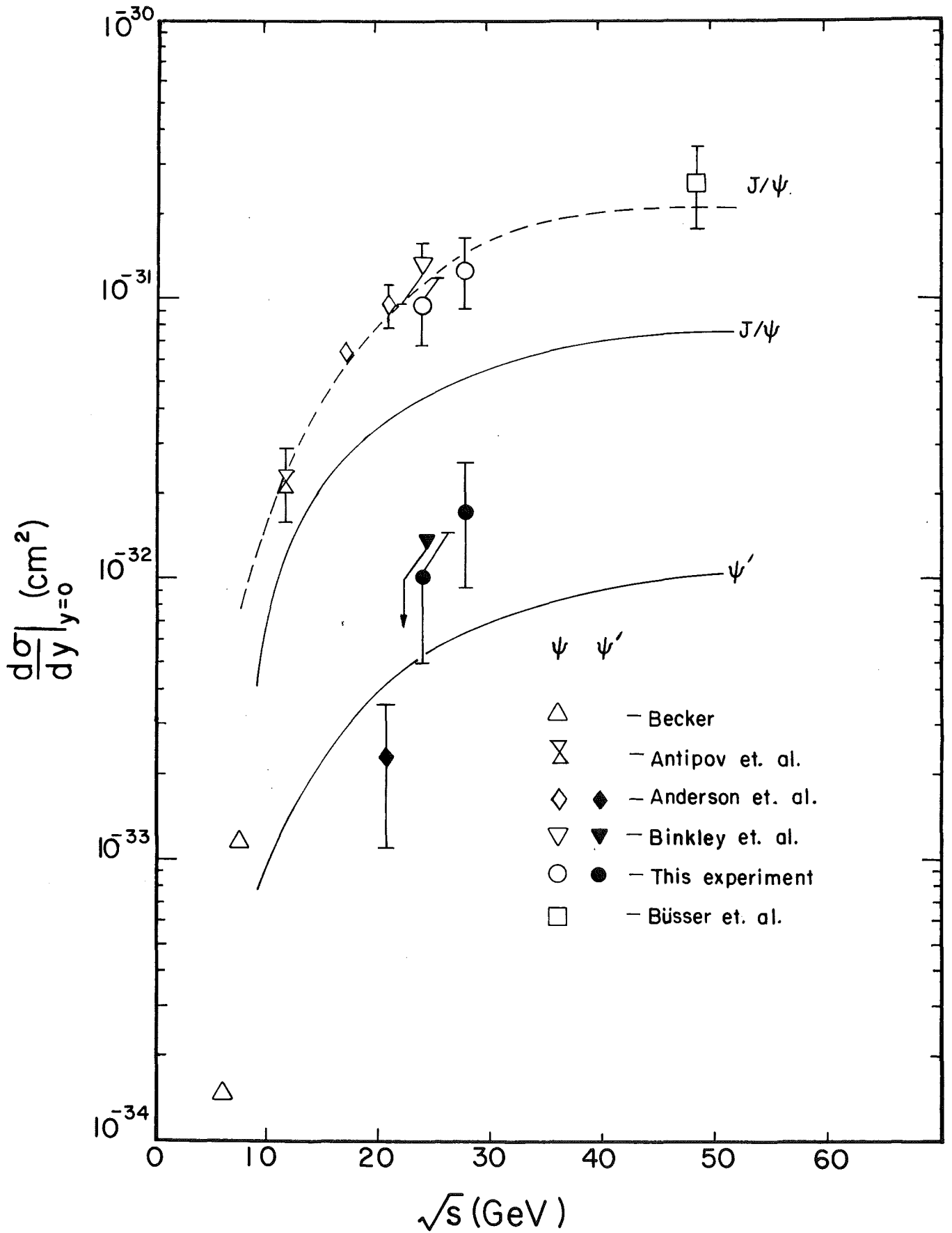


FIG. 36

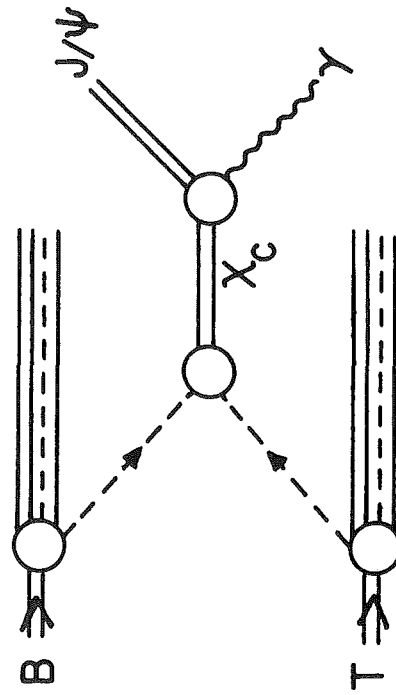


FIG. 37

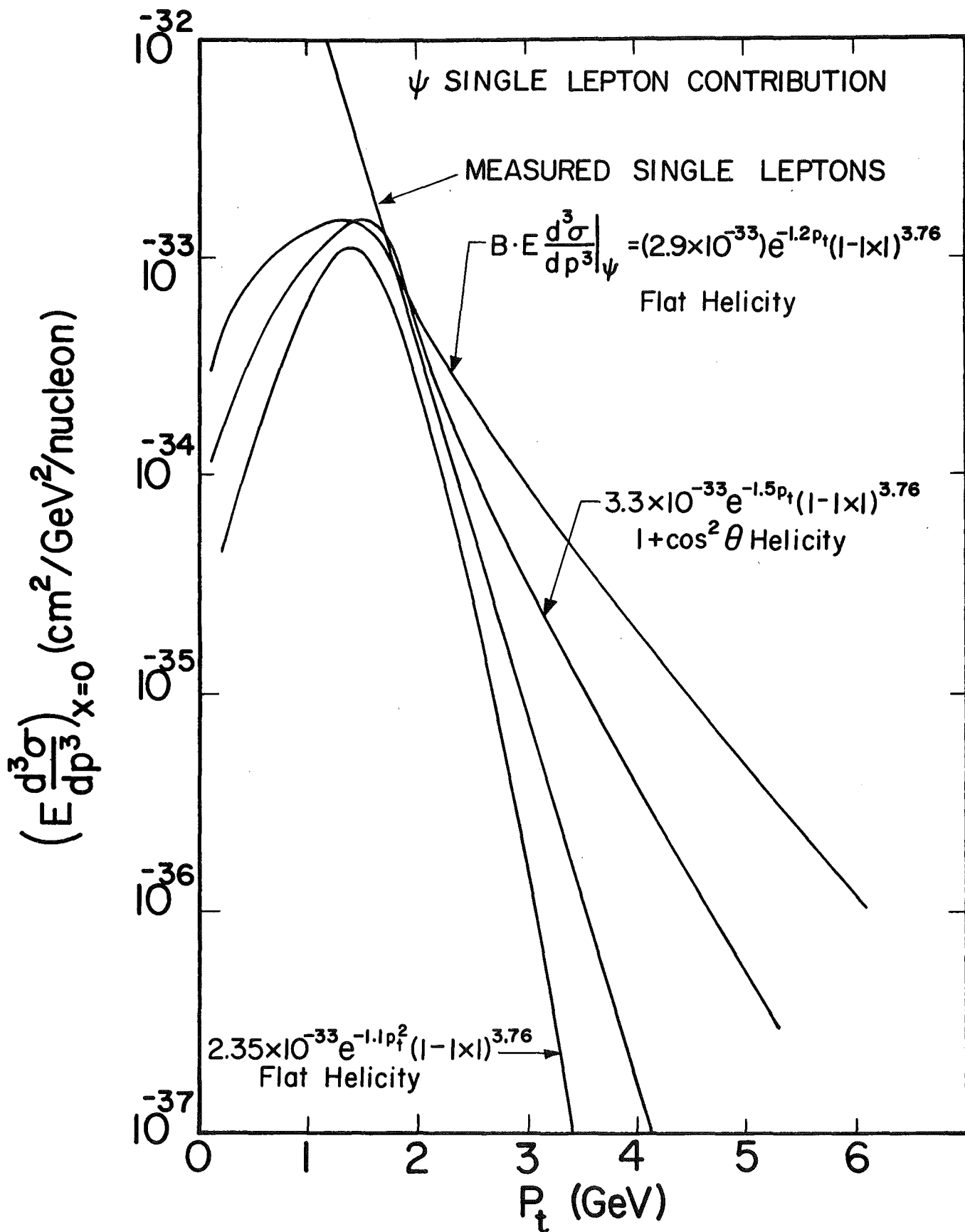
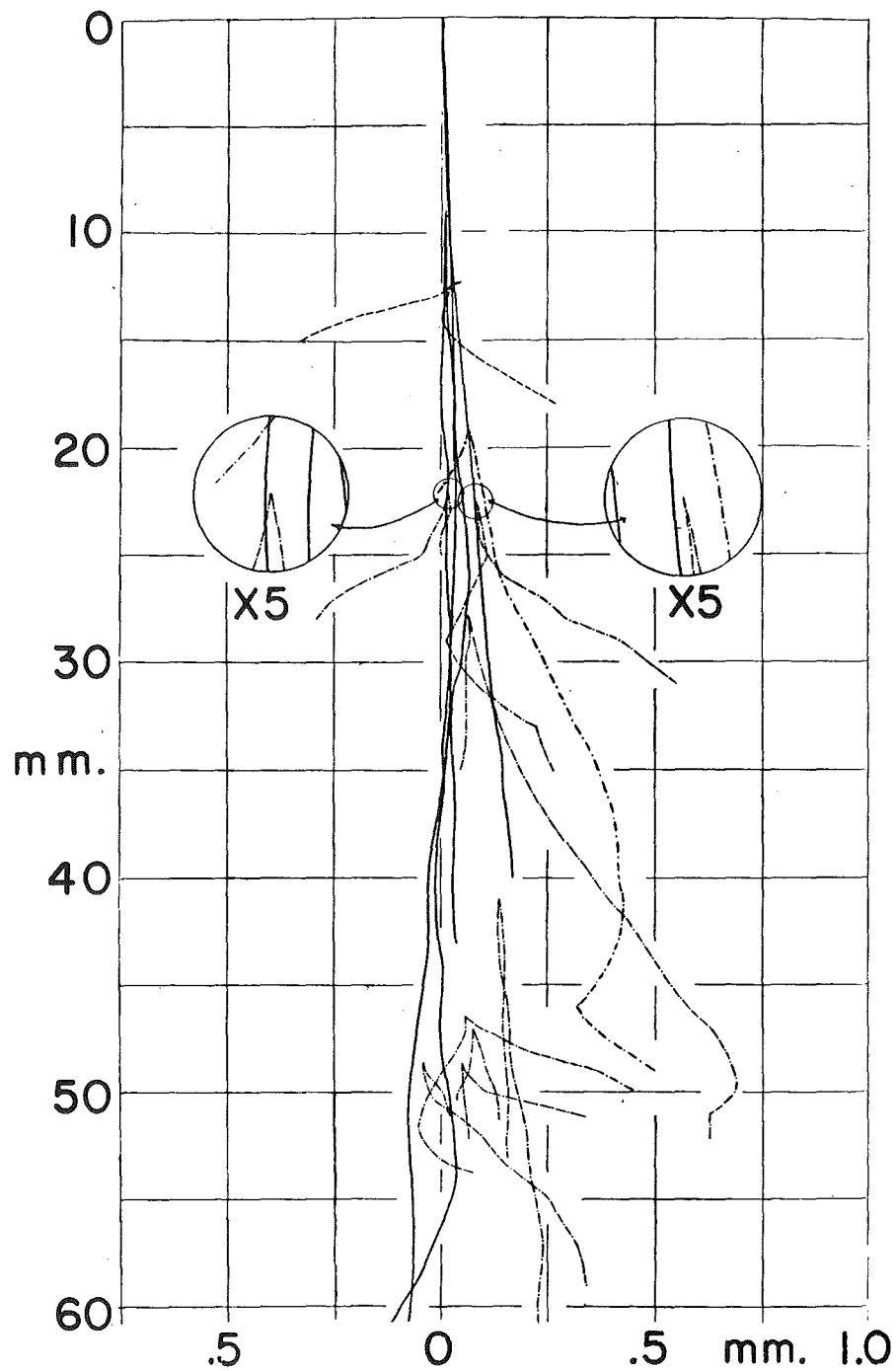


FIG. 38

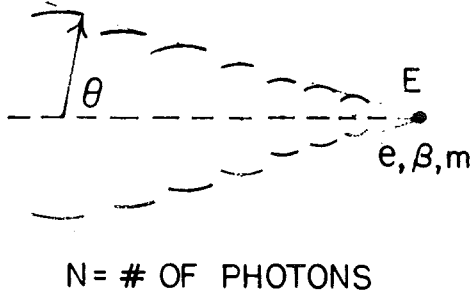


Traced drawing of the tracks in a cascade shower, initiated by an 18 GeV photon. Two radiation lengths of the shower development are shown. Note the factor of 20 difference in the horizontal and vertical scales. Particle tracks eventually disappear as they pass out of the plane of the photographic emulsion. (After J. E. Hooper, D. T. King, A. H. Morrish, Canadian Journal of Physics, 29, 550 (1951))

FIG. 39

CERENKOV RADIATION

(a)



$$\cos \theta = (\beta n)^{-1}$$

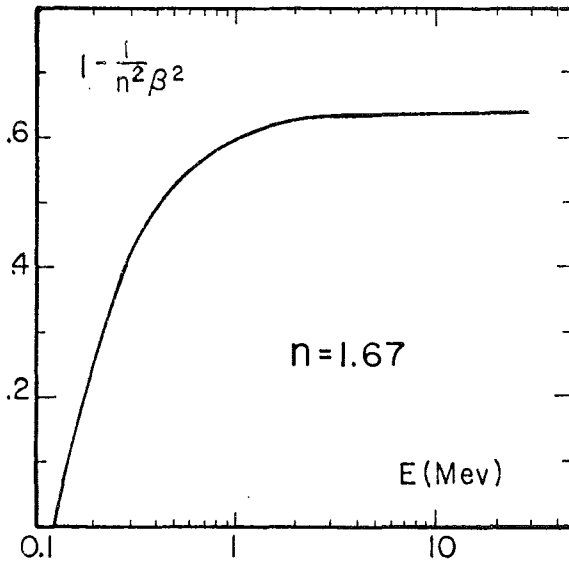
$$\frac{d^2 E}{dx d\omega} = \frac{e^2}{C^2} \left(1 - \frac{1}{n^2(\omega)\beta^2}\right) \omega \quad [\beta n(\omega) > 1]$$

$$\frac{d^2 N}{dx d\omega} = \frac{\alpha}{C} \left(1 - \frac{1}{n^2(\omega)\beta^2}\right)$$

$$\frac{dN}{dx} = 2\pi\alpha \left(\frac{1}{\lambda_1} - \frac{1}{\lambda_2}\right) \left(1 - \frac{1}{n^2\beta^2}\right)$$

CERENKOV FACTOR vs
ELECTRON ENERGY

(b)



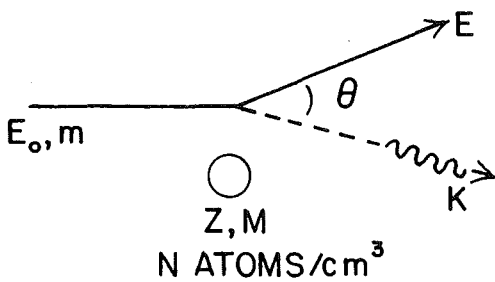
MINIMUM ELECTRON E for \hat{C}

$$\text{EMISSION} = m \left(\frac{1}{\sqrt{1-n^2}} - 1 \right) \approx .13 \text{ MeV}$$

REF. E. LONGO, I. SESTILI, NIM, 128, 283 (1975)

BREMSSTRAHLUNG

(c)



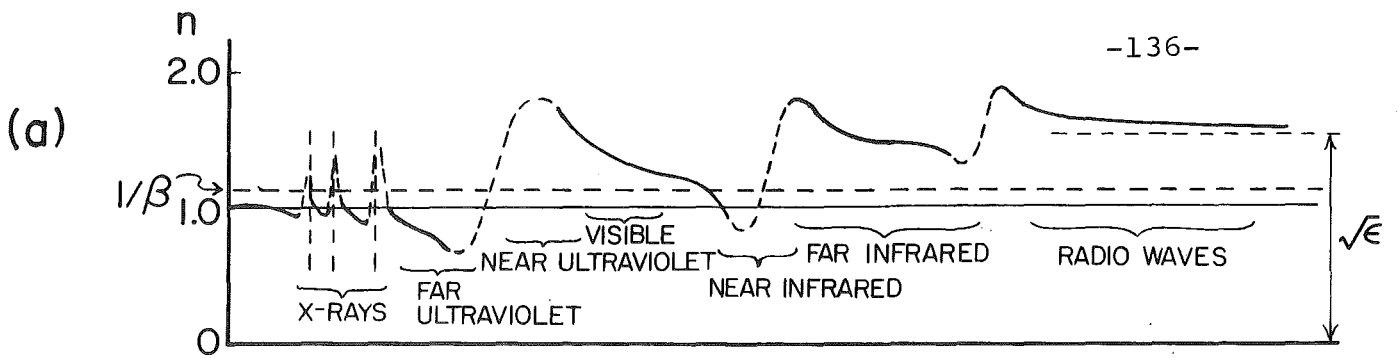
$$\theta(\text{RMS}) \approx 8.0 \ln(E_0/mc^2) / (E_0/mc^2) \text{ RADIANS}$$

ϕ_K = CROSS SECTION FOR PHOTON
EMISSION IN $dK / (E_0 - mc^2)$

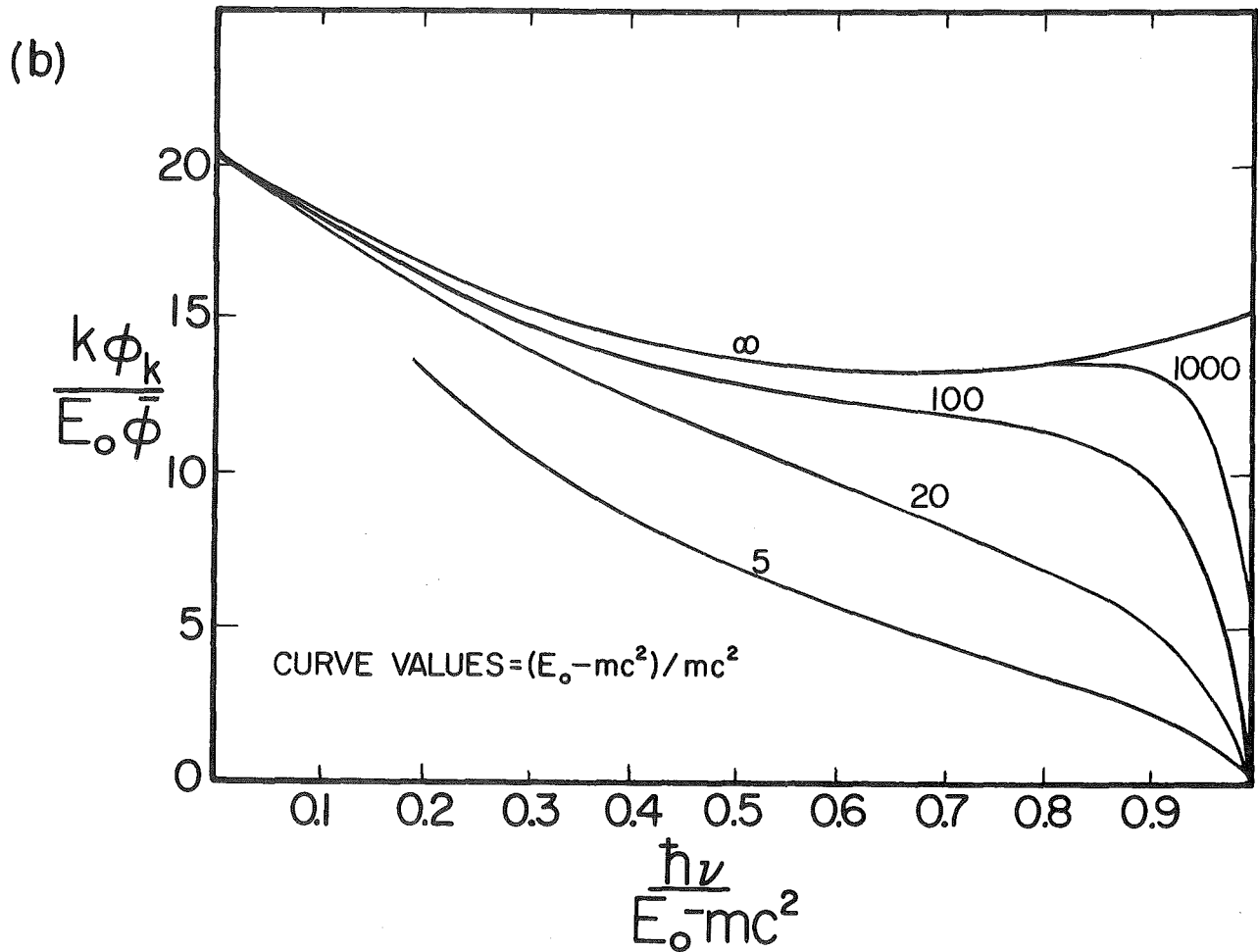
$$-\frac{dE}{dx} = N \int_0^1 K \phi_K d\left(\frac{K}{E - mc^2}\right)$$

$$-\frac{dE}{dx} = \frac{E}{\text{R.L.}} \left(\frac{E_0 E}{mc^2 K} \gg 137 Z^{-1/3} \right)$$

FIG. 40



SCHEMATIC DISPERSION CURVE FOR OPTICAL MEDIA
 (after Jenkins and White, Fundamentals of Optics, p487 (3rd. Ed)).



CALCULATED BREMSSTRAHLUNG INTENSITY AS A FUNCTION
OF $h\nu / (E_0 - mc^2)$ FOR LEAD

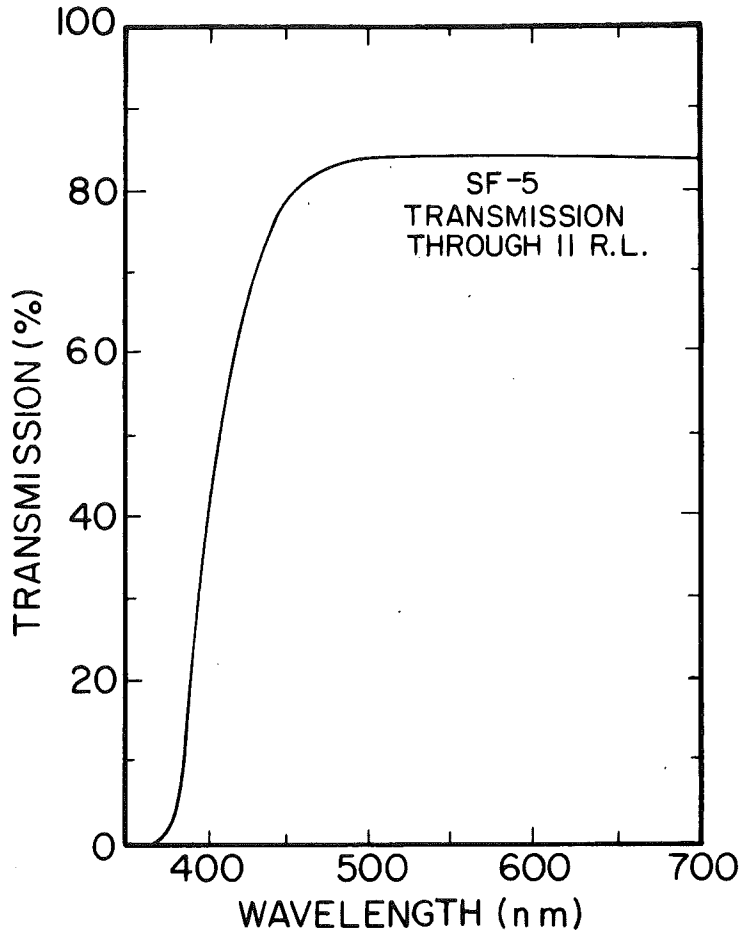
(after W. Heitler, Quantum Theory of Radiation, Oxford, (3rd Ed.), V,25)

$$\bar{\phi} = Z^2 e^4 / (137 m^2 c^4)$$

FIG. 41

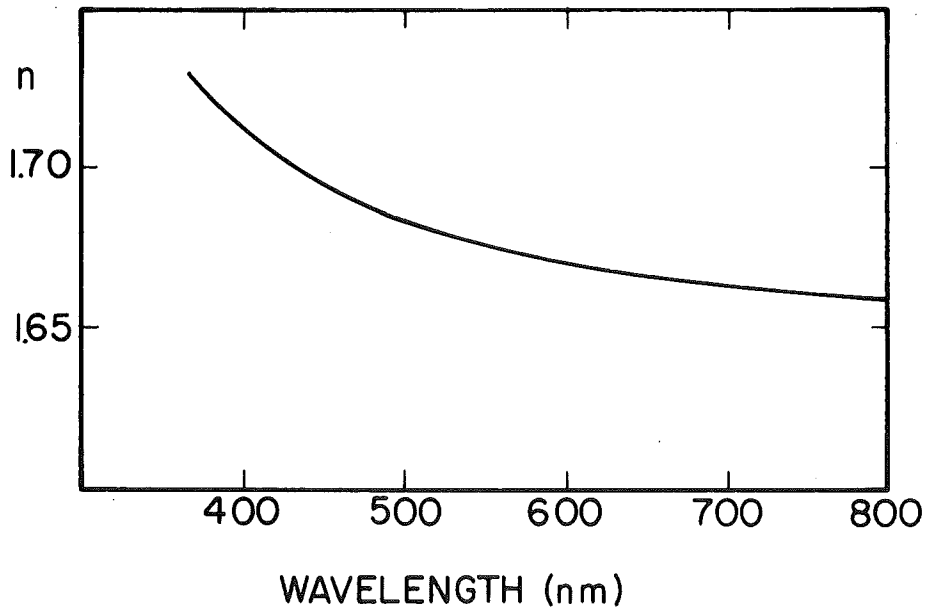
LEAD GLASS PROPERTIES

Manufacturer	Ohara, Inc. Tokyo
Type	SF 5
Radiation Length (R.L.)	2.36 cm.
Interaction Length	25.6 cm.
Specific Gravity	4.08 gm/cm. ³
Critical Energy	15.8 MeV
Composition	.55 PbO .38 SiO ₂ .05 K ₂ O .01 Na ₂ O



(REF. W.B. ATWOOD, SLAC REPORT
185 (JUNE 1975), APPENDIX B

SF-5 INDEX OF REFRACTION



(REF. 1971 OHARA OPTICAL GLASS CATALOG)

FIG. 42

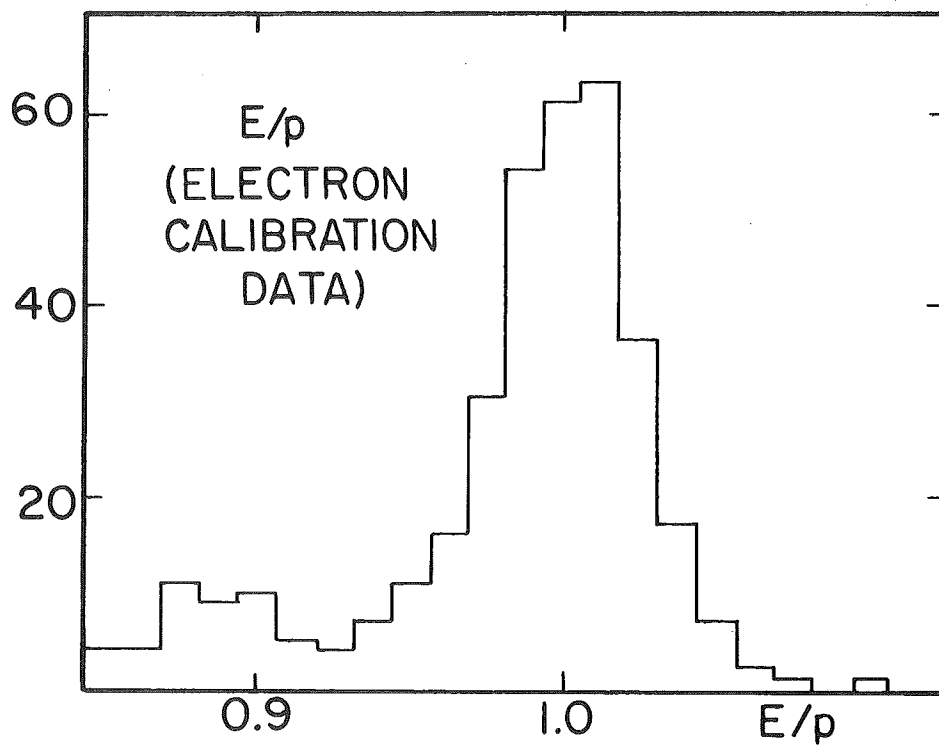


FIG. 43

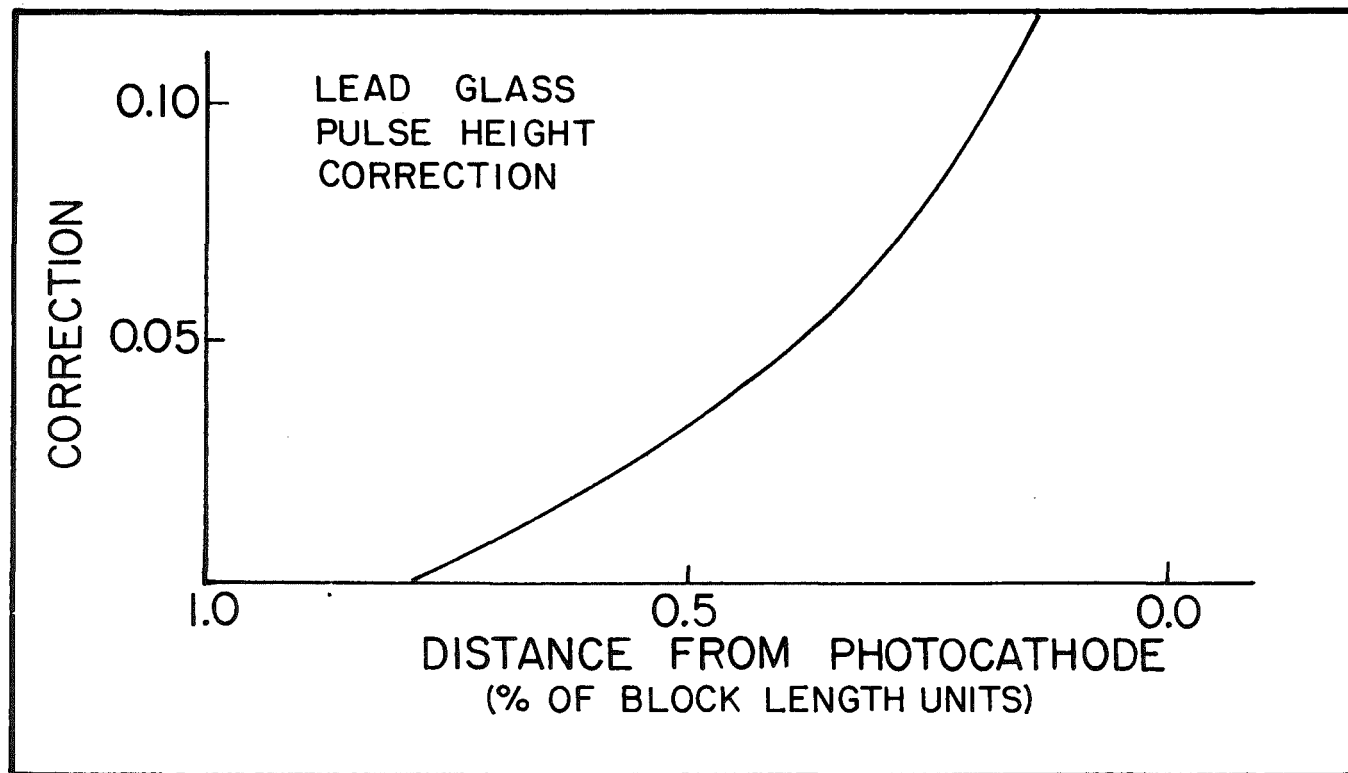


FIG. 44

% OF TOTAL LEAD GLASS LAYER ENERGY
IN SHOWER 'CONE' VS. 'CONE' RADII

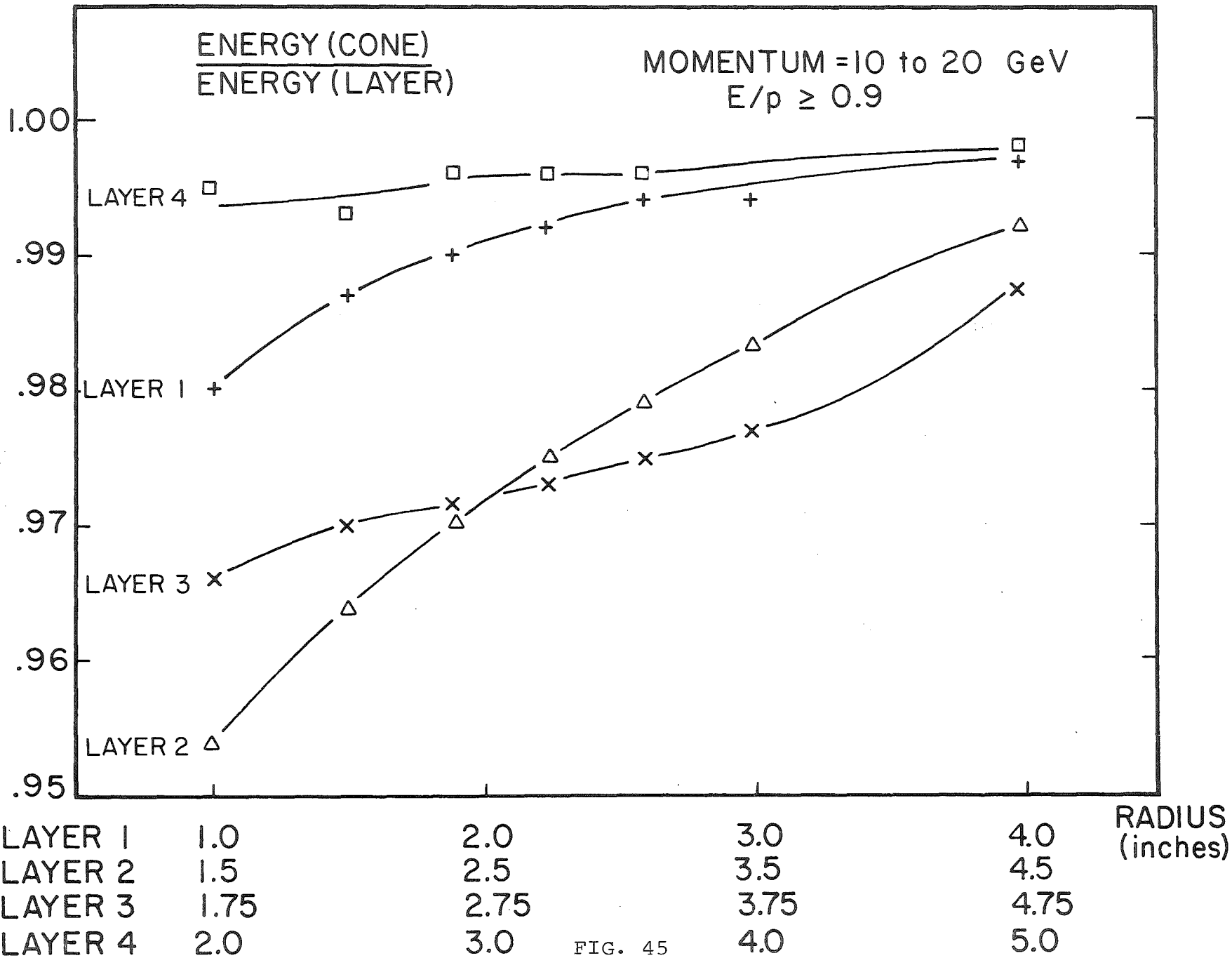
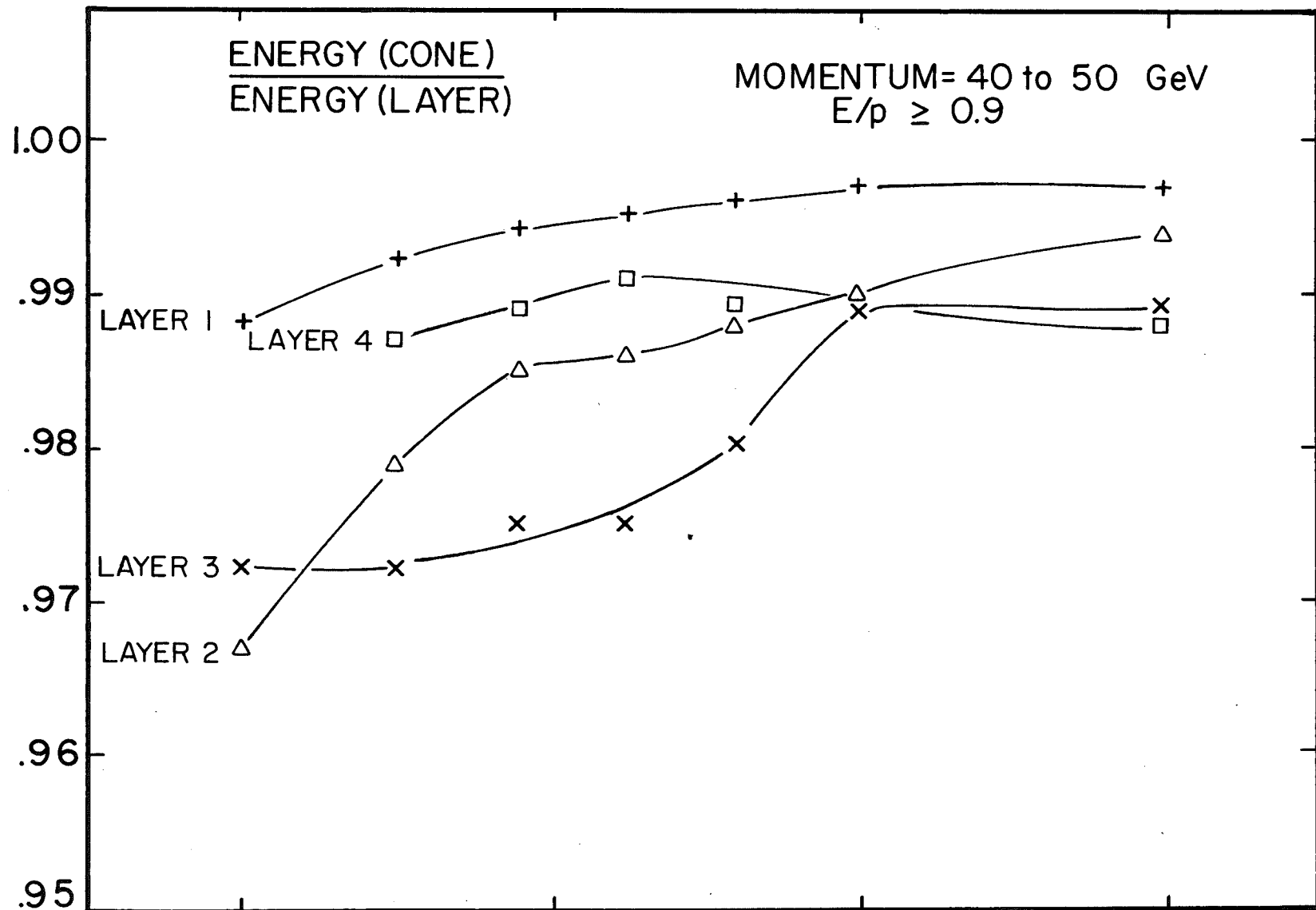


FIG. 45

% OF TOTAL LEAD GLASS LAYER ENERGY
IN SHOWER 'CONE' VS. 'CONE' RADII



Symbol	Layer	1.0	2.0	3.0	4.0	RADIUS (inches)
+	LAYER 1	0.988	0.994	0.996	0.997	1.0
Δ	LAYER 2	0.967	0.985	0.988	0.990	1.5
x	LAYER 3	0.972	0.975	0.980	0.989	1.75
□	LAYER 4	0.987	0.989	0.991	0.988	2.0

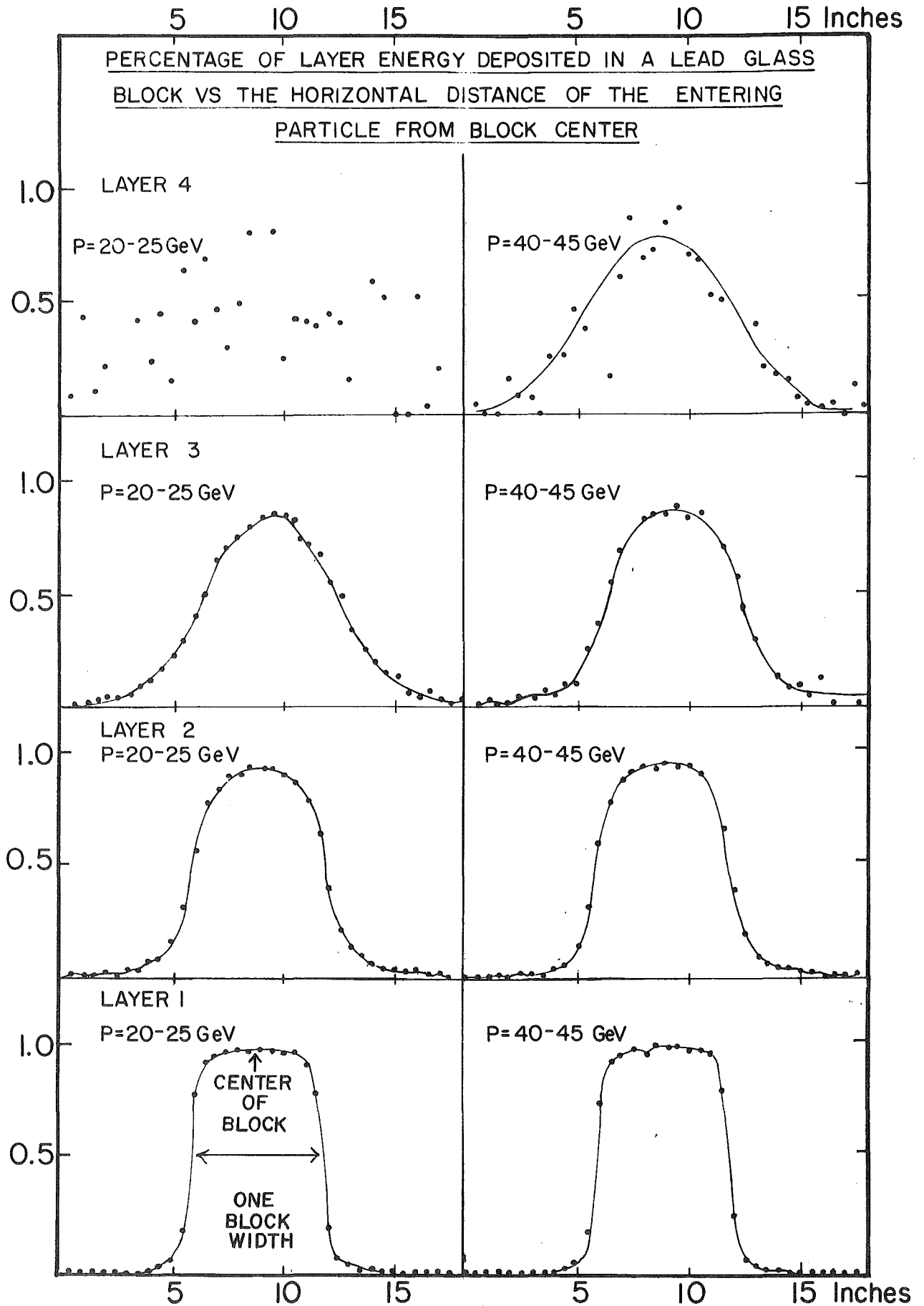


FIG. 47

% OF TOTAL LEAD GLASS ENERGY
IN SHOWER 'CONE' VS. E/p

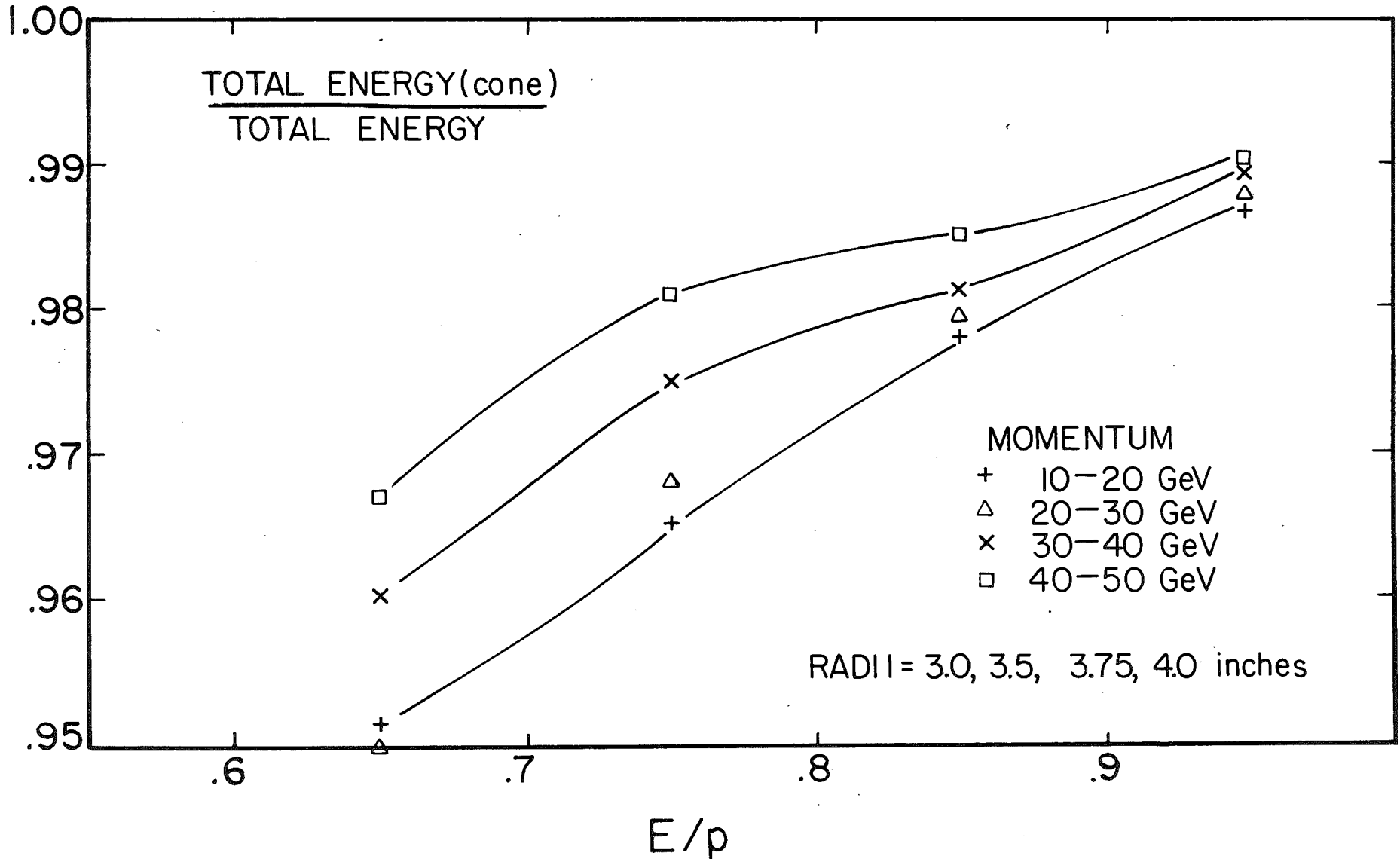
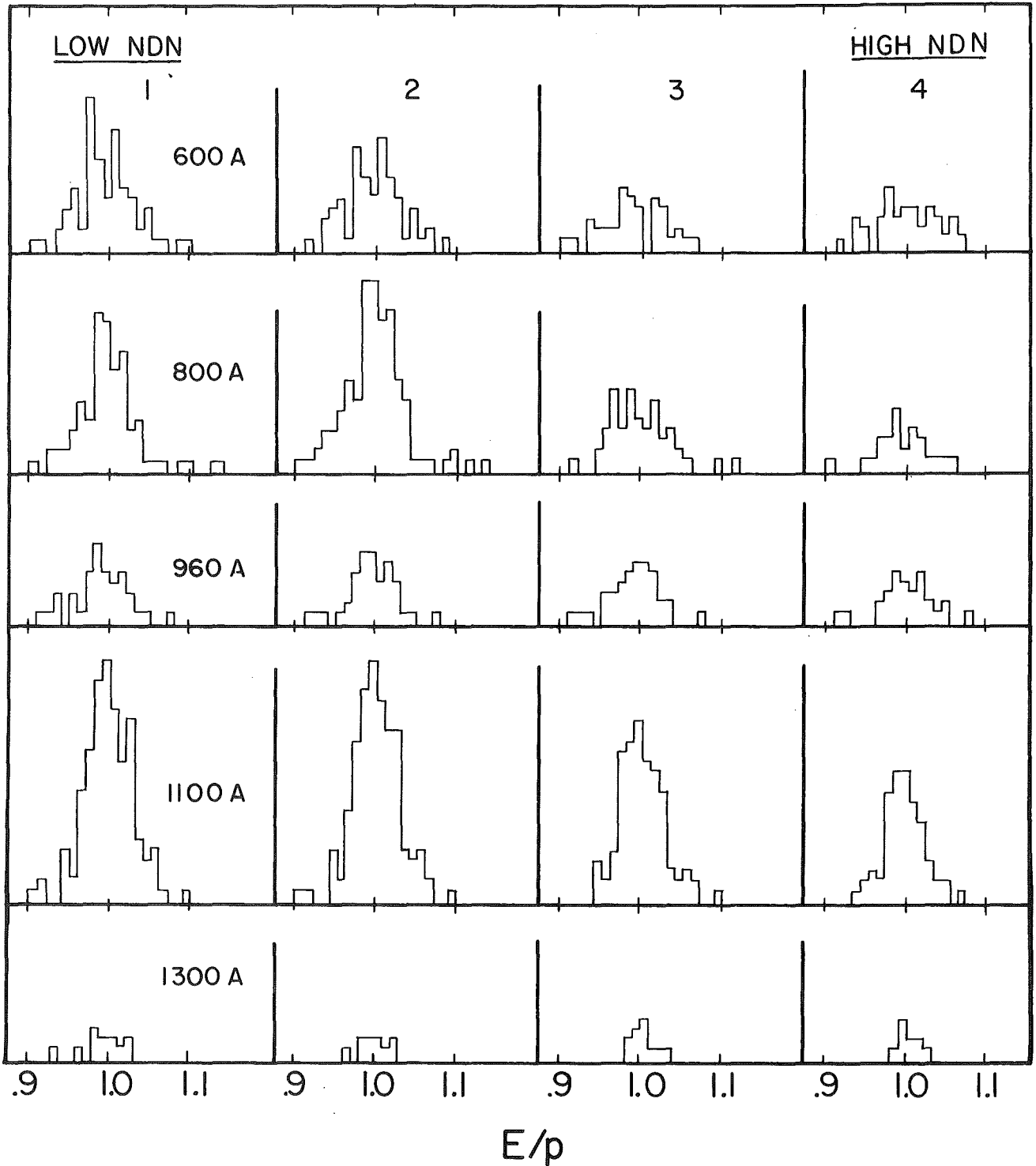


FIG. 48

DIELECTRON E/p PLOTS

- a.) EVENTS OF $E/p \geq 0.9$ (PAIRS ONLY)
- b.) PASSING MEDIUM LEAD GLASS LONGITUDINAL SHOWER CUTS
- c.) 400 GeV DATA
- d.) DIVIDED INTO 4 BINS OF NDN

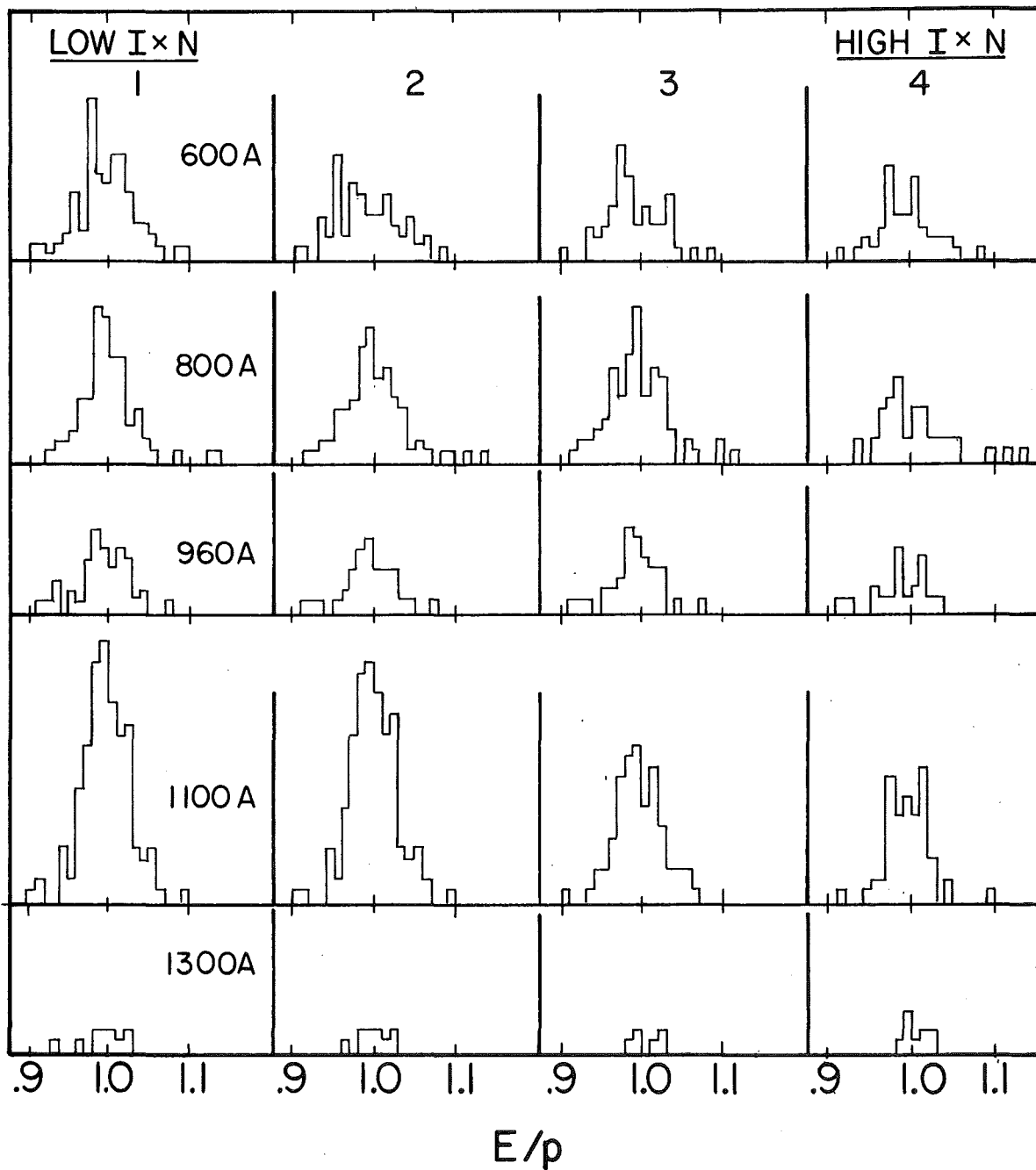


NOTE: EVENTS BELOW $E/p=0.9$ AND ABOVE $E/p=1.15$ ARE NOT SHOWN

FIG. 49

DIELECTRON E/p PLOTS

- a.) EVENTS OF $E/p \geq 0.9$ (PAIRS ONLY)
- b.) PASSING MEDIUM LEAD GLASS LONGITUDINAL SHOWER CUTS
- c.) 400 GeV DATA
- d.) DIVIDED INTO 4 BINS OF $INDUTY \times NDN (=I \times N)$



NOTE: EVENTS BELOW $E/p=0.9$ AND ABOVE $E/p=1.15$
ARE NOT SHOWN

FIG. 50

EXCESS LEAD GLASS ENERGY PLOTS

400 GeV DIELECTRONS

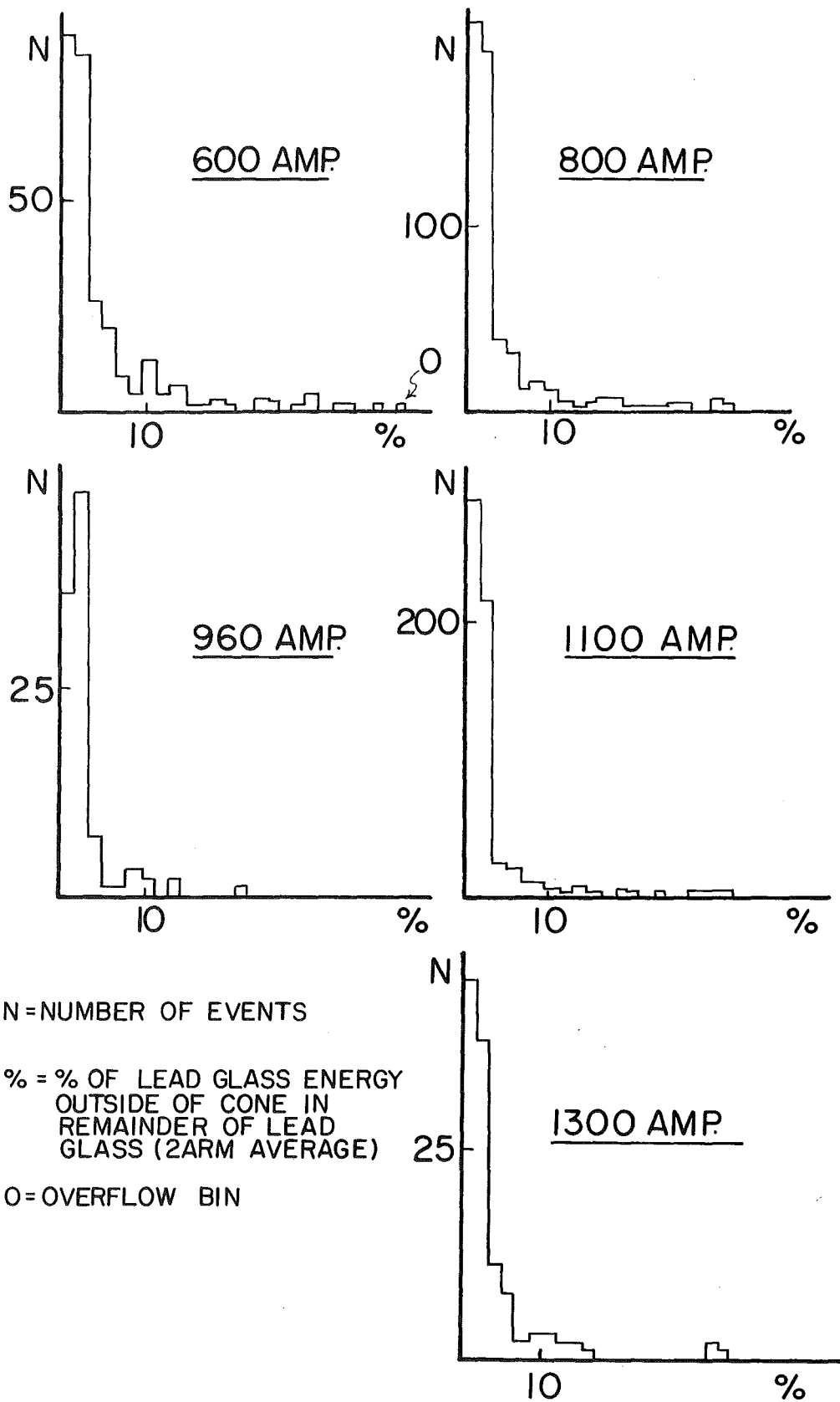


FIG. 51

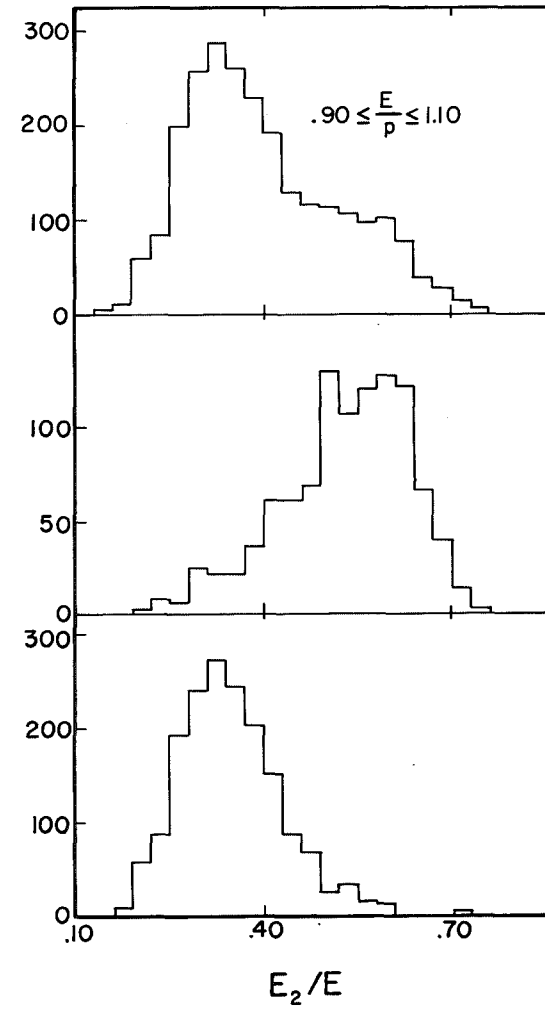
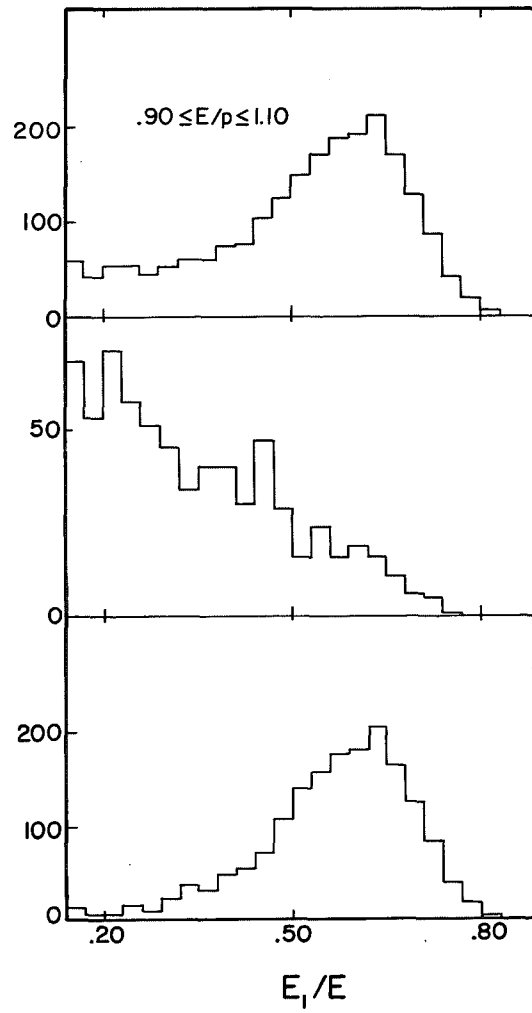
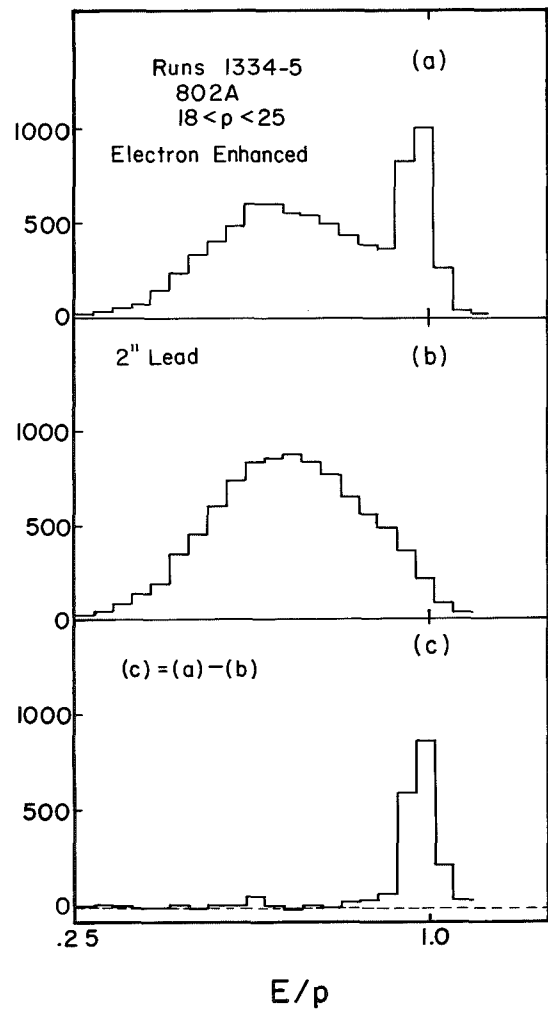


FIG. 52a

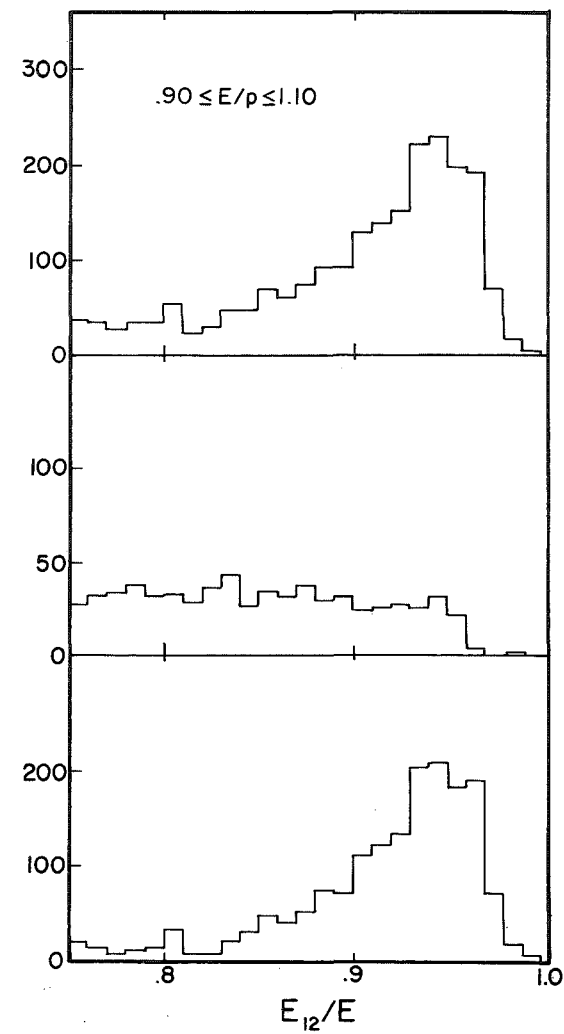
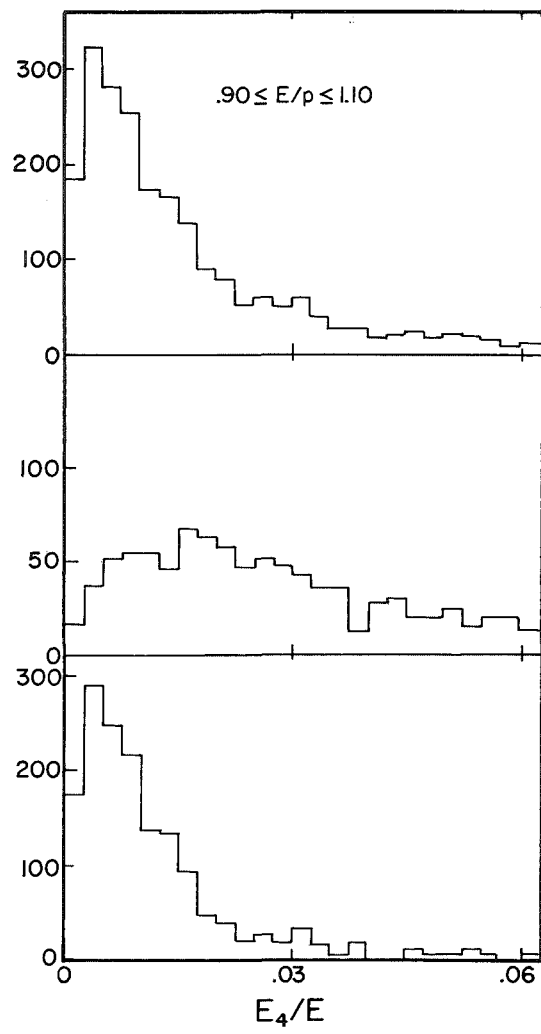
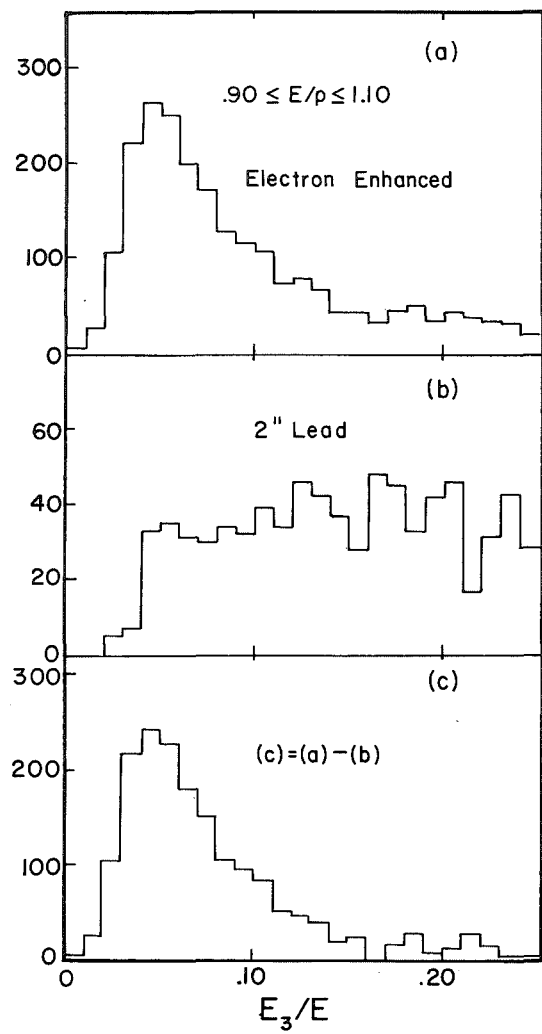


FIG. 52b